UNIVERSITY OF OKLAHOMA

GRADUATE COLLEGE

Variability, Multi-wavelength Properties, and Environments of Active Galactic Nuclei

A DISSERTATION

SUBMITTED TO THE GRADUATE FACULTY

in partial fulfillment of the requirements for the

Degree of

DOCTOR OF PHILOSOPHY

By

HEECHAN YUK
Norman, Oklahoma
2025

Variability, Multi-wavelength Properties, and Environments of Active Galactic Nuclei

A DISSERTATION APPROVED FOR THE
HOMER L. DODGE DEPARTMENT OF PHYSICS AND ASTRONOMY

BY THE COMMITTEE CONSISTING OF

Dr. Xinyu Dai, Chair

Dr. Edward Baron

Dr. Karen Leighly

Dr. Doerte Blume

Dr. Caleb Fulton

To my loving and supporting family

Acknowledgements

I would like to express my gratitude to my family. Without their continued love, support, and trust, I could not come anywhere close to where I am right now.

I would also like to thank my advisor Xinyu Dai. His guidance led me to become a competent and independent researcher and scientist.

I thank my committee members, Eddie Baron, Karen Leighly, Doerte Blume, and Caleb Fulton, as well as a former committee member, John Wisniewski, for their insightful and helpful advices over the years.

I am grateful for my colleagues at OU. Teamwork and friendship with them not only helped me academically, but also mentally, especially through the COVID era.

I would also like to thank many collaborators who worked on numerous projects with me, including Christopher Kochanek, Hai Fu, Ben Shappee, Tharindu Jayasinghe, Patrick Vallely, and many others. My research could never be complete without them.

Contents

Abstract

In the early twentieth century, Albert Einstein predicted the existence of black holes with his theory of general relativity. Over the past century, astronomers discovered many evidences that prove Einstein right. One of the most extreme cases of black holes is the supermassive black holes (SMBHs) found at the centers of most galaxies, with masses ranging from millions to billions of solar masses. Some of them are known to be actively consuming surrounding gas and dust, emitting a tremendous amount of energy during this process. These are called active galactic nuclei (AGNs), and these are some of the most energetic phenomena in the universe. AGNs are fascinating objects to study, as they are related to a number of areas in astronomy such as galaxy evolution and black hole physics.

One of prominent features of AGNs is variability; their brightness is always changing over time. Observations show that the AGN variability is stochastic, or a “red noise”, which means that the brightness difference increases as a function of time lag. This relation follows an approximate power law relation. However, past a certain time lag threshold, the power law index shifts to a smaller value. This point is called the break frequency, and this parameter is known to be correlated with the SMBH mass, suggesting that variability is closely related to the fundamental nature of AGNs.

To better understand the nature of AGNs, the AGN variability was analyzed in a few different ways in this dissertation. First, variability characteristics of a sample of galaxies, computed using the data from All-Sky Automated Survey for SuperNovae (ASAS-SN), were examined to distinguish AGNs from quiescent galaxies. By constraining the AGN fraction among galaxies, the timescale of AGN activities compared to galaxies’ age can be estimated. Then the multi-wavelength and environmental properties of the variability selected AGNs are analyzed. Second, the AGN break frequencies in optical power spectral densities (PSDs) are measured and compared to X-ray breaks. Current AGN models suggest that different regions around the AGN emit light at different wavelengths—shorter wavelength from near the central SMBH and longer wavelength from outer parts. If there is a correlation between optical and X-ray break frequencies, it can provide clues on the structure of AGNs and interactions between different regions. To achieve this goal, the optical break frequencies were measured using the data from ASAS-SN and Transiting Exoplanet Survey Satellite (TESS) on the sample of AGNs with X-ray break frequencies previously measured. With these methods, this study can contribute to the understanding of AGNs in both temporal and spatial terms.

The variability selection method showed that approximately 3% of galaxies are AGNs, and about 80% of them are classified as low-luminosity AGNs (LLAGNs). Because a portion of luminous AGNs are excluded from the parent galaxy sample, the true AGN fraction may be greater. LLAGNs are a subcategory of AGNs that display signs of activity, but not very energetic. This dissertation shows that LLAGNs most likely reside in denser environments compared to luminous AGNs, suggesting they may be triggered by different mechanisms compared to luminous AGNs. This result provides clues on timescales of different stages and evolution of AGN activities. Upon multi-wavelength analysis, the variability selected AGNs are often not classified as AGNs by traditional methods, meaning that this method provides a useful tool for discovering a larger population of AGNs, especially in the era of big data, as this procedure is automated and versatile so it can be used to any sets of data.

From the optical PSDs, a set of break frequencies is measured that is consistent with previous studies. In addition, a new set of break frequencies that is 1–2 orders of magnitude greater is also discovered. The high-frequency optical breaks displayed approximately 1-to-1 correlation with X-ray break frequencies, but with an offset in order of a few days. This can be interpreted as the X-ray variability driving the optical variability with a time delay, as it takes time for light to travel from one region to another. The size estimate from this time delay is consistent with measurements from previous studies, suggesting that this method introduces a new way to analyze the AGN structure.

Chapter 1

Introduction

1.1. Active Galactic Nucleus (AGN)

In 1915, Albert Einstein introduced the theory of general relativity. He proposed that massive objects warp the spacetime around them and other nearby objects move around the warped path (Einstein, 1915). In 1919, Arthur Eddington measured the starlight bending around the Sun during a solar eclipse, proving this theory (Dyson et al., 1920). General relativity also predicted the existence of black holes, the objects that warp spacetime to extremity. In 1964, an X-ray source, Cygnus X-1, was discovered. Detailed analyses uncovered that it is a binary star system where one star became a black hole and is in process of devouring its companion star (e.g., Rothschild et al., 1974). This is the first indirect detection of a black hole. Another evidence of a black hole was found in the center of our Milky Way Galaxy, where a number of stars were observed to orbit around a massive yet invisible object. By analyzing the orbits of these stars, the black hole in the galactic center was measured to be approximately 4 million solar masses (Eisenhauer et al., 2005). It is now widely believed that most galaxies host supermassive black holes (SMBHs), ranging from millions to billions of solar masses, at their centers. In 2019, the Event Horizon Telescope (EHT), a series of radio telescopes around the world, directly imaged a SMBH at the center of the galaxy M87, making it the first direct observation of a black hole (Event Horizon Telescope Collaboration et al., 2019). EHT also imaged the SMBH at the center of the Milky Way in 2022 (Event Horizon Telescope Collaboration et al., 2022).

In the mid-twentieth century, astronomers discovered unusual types of galaxies. In 1943, Carl Seyfert reported a class of galaxies with bright cores with strong broad emission lines in their spectra (Seyfert, 1943); they became to be known as Seyfert galaxies. In 1959, an all-sky catalog of radio sources, Third Cambridge Catalogue of Radio Sources (3C; Edge et al. 1959), was published. In the catalog, a few anomalous sources were found: 3C 48 and 3C 273. They appeared as point sources like stars, so they were called quasars (quasi-stellar radio sources). However, their optical spectra looked nothing like any known star. They had strong redshifted emission lines, suggesting they are not stars within our galaxy, but galaxies that are hundreds of megaparsecs away (Matthews & Sandage, 1963; Schmidt, 1963).

The common feature between Seyfert galaxies and quasars is that they have extremely bright cores. These cores cannot be powered by nuclear fusion, like stars, because it is physically impossible to generate so much energy within such small volume using fusion alone. Rather, theoretical models and observations support that they are powered by the central SMBHs actively accreting nearby matter. When matter falls into the SMBH, it does not directly fall in, but spirals inwards, creating an accretion disk, due to angular momentum. The magneto-rotational instability and outflows are the proposed mechanisms for the accretion material to lose angular momentum and move to inner orbits, and gravitational energy is converted to kinetic energy, heat, and radiation. The radiated energy is proportional to the accretion rate of the SMBH. Galactic cores with their SMBHs generating a significant amount of energy by accretion are called active galactic nuclei (AGNs).

There are many different types of AGNs, including Seyfert galaxies and quasars. Seyfert galaxies are characterized by strong emission lines, usually with resolved host galaxies. There are subcategories of Seyfert galaxies, type 1 and type 2. Type 1s display a broad Hα emission line, while type 2s display only narrow lines. Quasars are the most luminous type of AGNs. They appear very blue, or energetic in short wavelengths, display strong broad emission lines, and typically subtend small angular sizes. Quasi-stellar objects, or QSOs, refer to a class of AGNs that exhibit similar traits as quasars, but lack radio signals. Currently, quasars and QSOs are used interchangeably in literature disregarding their historical origins. Radio galaxies, as the name suggests, refer to galaxies with radio signals, but not as strong as quasars, and often with extended radio emissions. Blazars are the most variable sources with two main subcategories: flat spectrum radio quasars (FSRQs) and BL Lacs. While FSRQs have strong emission lines, BL Lacs have weak spectral lines or featureless continua. Low-ionization nuclear emission-line regions, or LINERs, are the least luminous type of AGNs, exhibiting very weak emission lines.

AGNs are fascinating objects to study for many reasons. They provide an opportunity to study black holes and accretion physics. Because AGNs are very bright, even distant AGNs from the early universe can be observed, which is important for studying the history of the universe and galaxy evolution.

1.2. AGN Structure

The AGN unification model is commonly used to describe the AGN structure (Antonucci, 1993; Urry & Padovani, 1995). At the center is the SMBH. Surrounding the SMBH is the accretion disk, which is the material that is falling into the SMBH and powering the AGN. Near the accretion disk is a broad line region, which is responsible for creating broad emission lines in the observed spectra. Outside the broad line region lies a dusty torus, which blocks the light coming out from the inside. In larger scales is the narrow line region. Relativistic jets come out from the SMBH from the polar direction relative to the accretion disk. The schematic of the unification model is shown on Figure 1.1.

According to this model, different classes of AGNs are due to different viewing angles of the

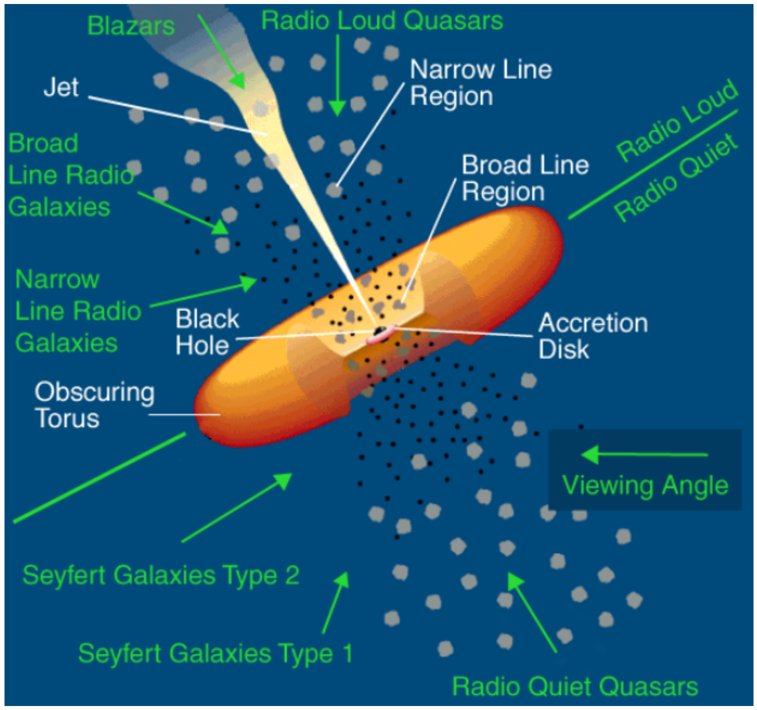

Figure 1.1: The schematic of the AGN unification model (Urry & Padovani, 1995; Reynolds et al., 2014).

same structure and the presence of a relativistic jet. If we look at the AGN at an angle such that the broad line region is not obscured by the dusty torus, we see type I AGN. If the dusty torus is in the line of sight, we cannot see the broad line region, so we see a type II AGN. If the AGN's jet is pointed towards us, we see a blazar.

1.3. AGN Detection and Classification

There are a number of different methods to identify AGNs among galaxies.

One method is examining the optical spectra. Type I AGNs are easily identified by the presence of broad Hα line. As described previously, not all AGNs have the broad Hα feature. For such objects, the strengths of narrow emission lines are examined. Baldwin et al. (1981) devised a method to use ratios of emission line strengths to identify AGNs. This diagnostic is called the BPT diagram.

Another method to identify AGNs is checking ultraviolet and optical colors (e.g., Schmidt & Green, 1983; Richards et al., 2002). While spectra of non-active galaxies are dominated by stars, AGN spectra are dominated by the emission of the accretion disk. They have very different comparative strengths at different wavelengths, making the colors very different. Specifically, AGNs are much brighter in bluer colors and dimmer in redder colors. In a similar manner, infrared colors can be used to identify AGNs as well (e.g., Assef et al., 2010; Stern et al., 2012).

AGNs are also known to be powerful sources of X-ray. The X-ray emission from AGNs come from the energetic corona above the accretion disk. A typical standard for AGN X-ray luminosity is 10^{42} erg s^{-1} or above (e.g., Mushotzky, 2004).

Radio emission is another way to identify AGNs, as the relativistic jets coming out from the AGNs' central engines emit strong radio waves. The mechanism responsible for the AGNs' radio emission is synchrotron radiation.

These methods probe different aspects of AGNs, giving different insights about AGNs. Not all AGNs will satisfy all of these criteria, depending on different AGN classes. For example, not all Seyfert galaxies are bright in radio, while some blazars lack emission lines for the BPT diagnostic.

1.4. AGN Variability

With the advent of long-time observations, astronomers discovered that variability is a ubiquitous feature of AGNs. AGN variability is observed in all wavelengths–X-ray (e.g., Uttley et al., 2002; Vaughan et al., 2003; González-Martín & Vaughan, 2012), ultraviolet (e.g., Wasleske et al., 2022), optical (e.g., Vanden Berk et al., 2004; Burke et al., 2020), infrared (e.g., Elmer et al., 2020), and radio (e.g., Mundell et al., 2009; Järvelä et al., 2024)–and all timescales–hours (e.g., Nandra et al., 1997; González-Martín, 2018), days (e.g., Aranzana et al., 2018; Burke et al., 2020), and years (e.g., di Clemente et al., 1996; Baldassare et al., 2020; Jha et al., 2022). Though variability is a prominent feature of AGNs, the mechanism behind it is still being debated. Numerous theories were proposed over the past few decades, including thermal processes (e.g., Lightman & Eardley, 1974; Shakura & Sunyaev, 1976; Kelly et al., 2009), accretion disk instabilities (e.g., Rees, 1984; Kawaguchi et al., 1998; Trèvese & Vagnetti, 2002), photon reprocessing (e.g., Haardt & Maraschi, 1991; McHardy et al., 2018), local disk communication processes on sound crossing or Alfvén timescales (Dexter & Agol, 2011), magnetorotational instabilities (e.g., Balbus & Hawley, 1991; Reynolds & Miller, 2009), and supernovae (e.g., Terlevich et al., 1992; Aretxaga et al., 1997).

Despite its uncertain origin, AGN variability is known to be correlated with physical properties. AGN variability is observed to be a red noise, which means that the variability amplitude is greater at lower frequency, or longer timescale (e.g., Uttley et al., 2002; Kelly et al., 2009). However, the variability amplitude does not increase indefinitely with lower frequency; it eventually flattens below a certain frequency. This is called the break frequency, or damping timescale. This quantity is correlated with the mass of the SMBH at the center of the AGN (e.g., Kelly et al., 2009; MacLeod et al., 2010; Burke et al., 2021). It is crucial to study AGN variability, as it can provide an important insight into the inner structure of AGNs and is a promising method to select a more complete sample of AGNs.

1.5. Wide Sky-Area Timing Surveys

Observing a large portion of the sky many times over an extended period of time enables different types of astronomical research. Rotation periods of stars can be measured by observing the regular pattern in the light curves. A sudden rise in brightness in a galaxy can indicate a supernova. The most common method of searching for exoplanets is the transit method, where drops in brightness are detected as a planet passes between the host star and the observer. Over the past decades, many surveys gathered long-time photometry data of the sky, such as the MACHO Project (Alcock et al., 1997), Lick Observatory Supernova Search (LOSS; Li et al. 2000), Sloan Digital Sky Survey (SDSS) Stripe 82 (York et al., 2000), All-Sky Automated Survey for SuperNovae (ASAS-SN; Shappee et al. 2014a; Kochanek et al. 2017), and Zwicky Transient Facility (ZTF; Bellm et al. 2019; Masci et al. 2019).

The quality of the time-series surveys has improved over the years, as more data accumulated in addition of technological advances. Surveys like ASAS-SN and ZTF archive high-quality all-sky photometry data over a decade. Space-based observatories such as *Kepler* (Borucki et al., 2010) and Transiting Exoplanet Survey Satellite (TESS; Ricker et al. 2015) provide relatively short-term, but high-cadence data. With such unprecedented data sets, it has become possible to study the variability of AGNs in much more detail.

1.6. Outline

This dissertation delves deeper into AGN variability in efforts to understand them better in a series of studies. I first defined the research topics and samples of the study with my advisor. I worked with collaborators for the data reduction. Then I analyzed the data, and discussed with the collaborators to interpret the results. Afterwards, I led the writing of the manuscripts. I was the corresponding author of three papers and it was my responsibility to submit the papers, respond to the referee reports, and correspond with the journal editors and coauthors during the submission process. The chapters in this dissertation are the reproductions of these papers.

For the first study, variability of galaxies was examined to distinguish AGNs from quiescent galaxies. Excess variance and structure function were computed to determine whether a galaxy's light curve displays an AGN-like variability. Then the spectra of the variability selected AGNs were examined to study their detailed characteristics, such as BPT classifications. For this study, the collaborators extracted ASAS-SN light curves and performed spectral fitting on SDSS spectra, and I wrote programs to automatically identify AGN-like variability and analyze spectral properties.

The first study was followed up by the multi-wavelength and environmental analysis of the variability selected AGN sample. The infrared and X-ray data was examined to check how many of the variability selected AGNs satisfy traditional AGN classification methods. In addition, catalogs of galaxies and galaxy clusters were used to determine whether the variability selected AGNs are more commonly found in denser environments. I gathered the multi-wavelength data and catalogs, and the collaborators contributed in extracting additional X-ray data. I processed and analyzed the data, then discussed with the collaborators for interpretations.

Another way the AGN variability was studied was examining the AGNs' power spectral densities (PSDs). Specifically, the break frequencies in optical PSDs were measured. ASAS-SN and TESS light curves were used to construct PSDs. The broken power law model was used to fit the joint PSDs to measure the break frequencies, and the break frequencies were examined for correlations with SMBH mass and X-ray break frequencies reported in literature. I obtained a list of targets for this project, for which collaborators extracted ASAS-SN light curves. Collaborators also provided the program to extract TESS light curves, which I executed. Then I calibrated the ASAS-SN and TESS light curves, computed the PSDs, performed the PSD fitting for analysis. In addition, I simulated light curves to examine the robustness of this method and explored multi-variable correlations.

CHAPTER 2

Variability Selected Active Galactic Nuclei from ASAS-SN Survey: Constraining the Low Luminosity AGN Population

This chapter is the reproduction of Yuk et al. (2022), ApJ, 930, 110.

2.1. Abstract

Low luminosity active galactic nuclei (LLAGN) probe accretion physics in the low Eddington regime and can provide additional clues about galaxy evolution. AGN variability is ubiquitous and thus provides a reliable tool for finding AGN. We analyze the All-Sky Automated Survey for SuperNovae light curves of 1218 galaxies with $g < 14$ mag and Sloan Digital Sky Survey spectra in search of AGN. We find 37 objects that are both variable and have AGN-like structure functions, which is about 3% of the sample. The majority of the variability selected AGN are LLAGN with Eddington ratios ranging from 10^{-4} to 10^{-2}. We thus estimate the fraction of LLAGN in the population of galaxies as 2% down to a median Eddington ratio of 2×10^{-3}. Combining the BPT line ratio diagnostics and the broad-line AGN, up to ∼60% of the AGN candidates are confirmed spectroscopically. The BPT diagnostics also classified 10–30% of the candidates as star forming galaxies rather than AGN.

2.2. Introduction

Active galactic nuclei (AGNs) are some of the most luminous objects found in the universe, driven by accretion onto a supermassive black hole. Studies show that AGN and their host galaxy properties are strongly correlated. For example, the AGN class is closely related to galaxy morphology (e.g., Slavcheva-Mihova & Mihov 2011; Chen & Hwang 2017; Bornancini & García Lambas 2018; Gkini et al. 2021), AGN feedback can suppress star formation (e.g., Hopkins & Elvis 2010; Zubovas & King 2012; Alberts et al. 2016; Yuan et al. 2018), and merger events can ignite AGN activities (e.g., Keel et al. 1985; Ellison et al. 2011, 2019; Koss et al. 2012). The strongest evidence of coevolution between AGN and host galaxies is the $M - \sigma$ correlation between black hole masses and the stellar velocity dispersion (Ferrarese & Merritt 2000; Gebhardt et al. 2000; Graham et al. 2011; McConnell et al. 2011; Morabito & Dai 2012). The central black hole is active only some of the time, so the fraction of active galaxies constrains the AGN duty cycle, which in turn can be used to match the black hole with accretion rate history (e.g., Yu & Tremaine 2002; Marconi et al. 2004; Tamura et al. 2006; Shankar et al. 2009). AGN activities also have an environmental dependence: rich clusters show lower AGN activity due to inefficient mergers (e.g., Kauffmann et al. 2004; Lopes et al. 2017; Mishra & Dai 2020) at low redshifts below the peak of AGN activities. At high redshifts, observational evidence points to higher AGN fractions in clusters (Eastman et al. 2007; Haggard et al. 2010; Martini et al. 2013). For the low-density environments in cosmic voids, the existing few studies suggest potential higher AGN fractions (Constantin et al. 2008; Mishra et al. 2021).

An interesting subset of AGN is the low luminosity AGN (LLAGN). There exist many, some fundamental, differences between LLAGN and luminous AGN. LLAGN are thought to be less triggered by major mergers and more by effects such as tidal disruptions and disk instabilities (e.g., Hopkins & Hernquist 2009; Hopkins et al. 2014). Observations and models suggest that the broad-line region and the obscuring "torus" disappear for the AGN with the lowest luminosities (e.g., Ho et al. 1997c; Nicastro 2000; Laor 2003; Elitzur & Shlosman 2006), so LLAGN do not follow the standard AGN unification model. Instead, the black hole may have a radiatively inefficient accretion flow at small radii and a truncated thin disk farther out combined with a jet or outflow (e.g., Chen & Halpern 1989; Ho 2008). AGN with lower luminosities tend to have a greater fraction of their accretion power converted into a relativistic jet which can have a significant impact on galaxy formation (Ho, 2008). Active galaxies are known to spend significantly more time as LLAGN than as luminous AGN, but LLAGN evolution is not well understood. One observation that can provide clues about the evolution of AGN is the LLAGN fraction as a constraint on the duty cycle of this form of accretion.

One of defining features of AGN is their variability across the entire electromagnetic spectrum on all timescales. The mechanism responsible for the variability is still unknown. Proposed mechanisms include thermal fluctuations (e.g., Lightman & Eardley 1974; Shakura & Sunyaev 1976; Kelly et al. 2009), accretion disk instabilities (e.g., Kawaguchi et al. 1998; Trèvese & Vagnetti 2002), supernova explosions (e.g., Aretxaga et al. 1997), and reprocessing photons between the accretion disk and the corona (e.g., Haardt & Maraschi 1991; McHardy et al. 2018). It is known that the variability is stochastic in nature (e.g., Kelly et al. 2009; MacLeod et al. 2010) and it can be modeled by simple stochastic process models.

As a ubiquitous feature of AGN, variability can be used to find AGN. One way of characterizing the AGN variability is the structure function (e.g., Vanden Berk et al. 2004; Kozłowski 2017; Middei et al. 2017), defined by the mean square flux change as a function of the time separating the measurements. The advantage of the structure function is that it can be measured accurately even with unevenly sampled light curves with seasonal gaps. The structure functions of AGN are roughly a broken power law, initially rising in amplitude as the time lag increases and flattening into a plateau (e.g., Trevese et al. 1994; MacLeod et al. 2010; Kozłowski 2017). The light curve of any galaxy can be examined to see if it has an AGN-like structure function to identify AGN that other methods, such as broad emission lines, optical color space, X-ray, mid-IR, and radio emissions, may miss.

There have been previous studies of variability selected AGN samples. MacLeod et al. (2011) analyzed ~10,000 variable sources from Sloan Digital Sky Survey (SDSS) data. They compared the structure function of the variable objects with the damped random walk (DRW) model to select quasars, and their fraction of variability selected quasars that were previously confirmed quasars was >90%. Butler & Bloom (2011) parameterized the structure function of quasars as a function of brightness and used this model to find AGN. Their algorithm identified 99% of the known quasars correctly while finding thousands of new quasars, increasing the quasar sample size by 29%. Ruan et al. (2012) investigated the optical variability of ~190,000 variable objects from the MIT Lincoln Laboratory (MITLL) Lincoln Near-Earth Asteroid Research (LINEAR) survey. They characterized the blazar variability by the DRW model and compared it to the LINEAR variables. Compared to the Fermi catalog, their selection method identified blazars with an efficiency of $E \geq 88\%$ and a completeness of $C = 88\%$. Sánchez-Sáez et al. (2019) analyzed the variability features of over 200,000 light curves from QUEST-La Silla AGN Survey, finding ~ 5000 AGN. Their spectroscopic follow-up found that >80% of their variability selected AGN display AGN-like spectral features.

Most of the variability selected AGN samples are quasars at the high luminosity end of the AGN population. In this study, we seek to find AGN with a wider range of luminosity, including LLAGN, so we can place tighter constraints on the AGN fraction among galaxies in the low Eddington regime. We use the data from the All-Sky Automated Survey for SuperNovae (ASAS-SN; Shappee et al. 2014a; Kochanek et al. 2017) to do a variability analysis of 1218 nearby SDSS galaxies using structure functions to identify AGN candidates. The SDSS spectra (Ahumada et al., 2020) can then be used to further characterize the candidates.

In Section 2.3, we describe the ASAS-SN data used for this study. In Section 2.4, we discuss the systematic procedures for analyzing the light curves to find AGN candidates. In Section 2.5, we present our results. In Section 2.6, we further analyze the properties of the candidates. The paper is summarized in Section 2.7. Throughout this paper, we assume a ΛCDM cosmological model, with $H_0 = 70$ km s^{-1} Mpc^{-1}, $\Omega_\Lambda = 0.7$, and $\Omega_M = 0.3$.

2.3. Data

ASAS-SN (Shappee et al. 2014a; Kochanek et al. 2017) is a network of telescopes that has been observing the extragalactic sky since 2012. ASAS-SN has expanded a number of times and now consists of 20 14 cm telescopes in five mounts that have been surveying the entire visible sky every night since late 2017. The original two mounts used the V-band filter until 2018 and then switched to the g-band, while the three new mounts commissioned in late 2017 used the g-band from the start. ASAS-SN's limiting magnitude is $V \sim 16.5 - 17.5$ and $g \sim 17.5 - 18.5$ depending on lunation.

The field of view of an ASAS-SN camera is 4.5 deg^2, the pixel scale is 8.″0 and the FWHM is typically ∼2 pixels. The ASAS-SN light curves were extracted as described in Jayasinghe et al. (2018) using image subtraction (Alard & Lupton, 1998; Alard, 2000) and aperture photometry on the subtracted images with a 2 pixel radius aperture. The APASS catalog (Henden et al., 2015) was used for calibration. We corrected the zero-point offsets between the different cameras as described in Jayasinghe et al. (2018). The photometric errors were recalculated as described in Jayasinghe et al. (2019).

For this study, we extracted nuclear light curves for the 1218 $g < 14$ mag SDSS galaxies with SDSS spectra (Ahumada et al., 2020). The spectrum allows us to spectroscopically classify the variability identified candidates. A typical object has 280 V-band data points spanning over 2000 days, and 180 g-band data points spanning over 600 days. The typical uncertainties are 0.02 mag for the V-band and 0.03 mag for the g-band. Before starting the analysis of the light curves, significant outliers are removed, as they can affect the variability measurements. We discarded data points more than 5σ from the median, where σ is the standard deviation of the measurements. We also rejected objects with mean ASAS-SN magnitudes that differ from the SDSS magnitudes by >2 mag; most of these objects have nearby bright sources that can contaminate the photometry.

2.4. Method

We searched for AGN in two steps. First, we calculate the excess variance of each light curve to see if the source has significant variability. If a source appears to be variable, we calculate the structure function of the light curve, and model it to see if the variability is AGN-like. We analyzed the V- and g-band light curves separately for each target.

2.4.1. Excess Variance

The excess variance measures the intrinsic variability of the object beyond measurement uncertainties (e.g., Nandra et al., 1997; Edelson et al., 2002; Vaughan et al., 2003). For this study, we calculate the excess variance using magnitudes, so we use unnormalized excess variance, which is calculated by correcting the variance for the photometric noise,

$$\sigma^2_{\rm XS} = S^2 - \overline{\sigma^2_{\rm err}}, \tag{2.1}$$

where S^2 is the variance of the light curve and $\overline{\sigma^2_{\rm err}}$ is the mean square measurement error. If this value is negative, then the variance of the data is within the range of measurement error. Assuming the uncertainty of $\overline{\sigma^2_{\rm err}}$ is negligible, the error in the excess variance is

$$\Delta(\sigma^2_{\rm XS}) = \sqrt{\frac{2}{N-1}} S^2, \tag{2.2}$$

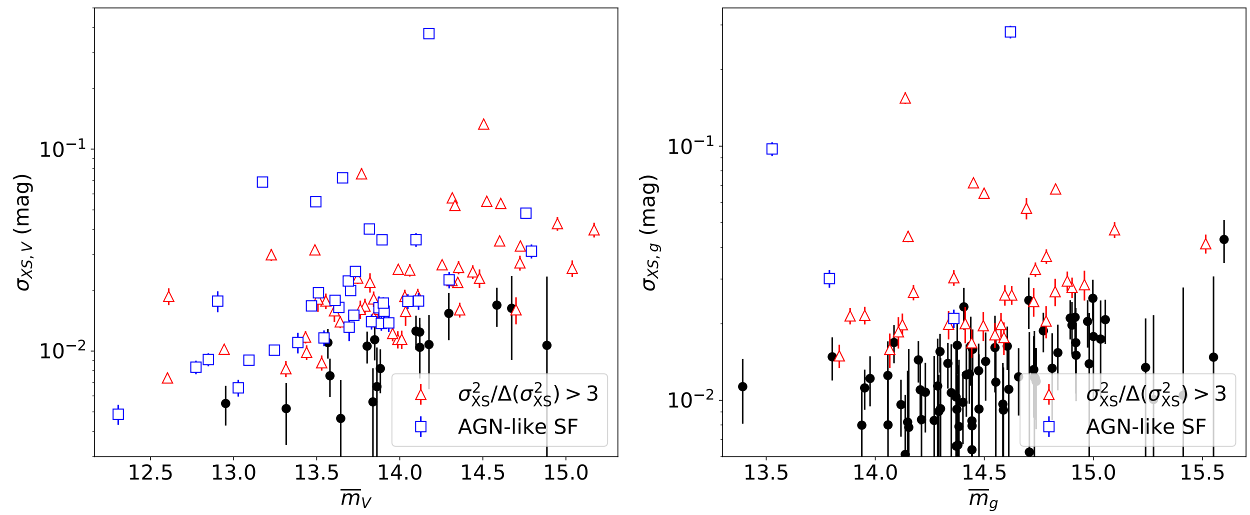

Figure 2.1: Excess variance versus mean magnitude of all ASAS-SN objects with $\sigma^2_{\rm XS} > 0$. The black circles are galaxies with $\sigma^2_{\rm XS}/\Delta(\sigma^2_{\rm XS}) < 3$, red triangles are galaxies with $\sigma^2_{\rm XS}/\Delta(\sigma^2_{\rm XS}) > 3$, and the blue squares also have AGN-like structure functions.

where N is the number of data points (Trumpler & Weaver 1953; Edelson et al. 2002).

The distribution of the galaxies in $\sigma_{\rm XS}$ is shown in Figure 2.1, and a galaxy is considered to have significant variability if $\sigma^2_{\rm XS}/\Delta(\sigma^2_{\rm XS}) > 3$. Using the variability in magnitudes, the fractional flux variability is

$$\frac{\Delta F}{F} = |1 - 10^{-0.4\sigma_{\rm XS}}|, \tag{2.3}$$

and as seen in Figure 2.2, most objects with $\sigma^2_{\rm XS}/\Delta\sigma^2_{\rm XS} > 3$ have $\Delta F/F \gtrsim 10^{-2}$. Excluding highly variable outliers, there is a weak trend for fainter objects to require higher variability amplitudes for detection, which is to be expected given the increase in photometric uncertainties with magnitude.

2.4.2. Structure Function

Several different definitions of the structure function are in use, where the two most common forms are

$$\mathrm{SF}(\tau) = \sqrt{\langle [m(t+\tau) - m(t)]^2\rangle - \sigma^2_{noise}}, \tag{2.4}$$

(e.g., Bauer et al. 2009; Middei et al. 2017) and

$$\mathrm{SF}(\tau) = \sqrt{\frac{\pi}{2}\langle |m(t+\tau) - m(t)|\rangle^2 - \sigma^2_{noise}}, \tag{2.5}$$

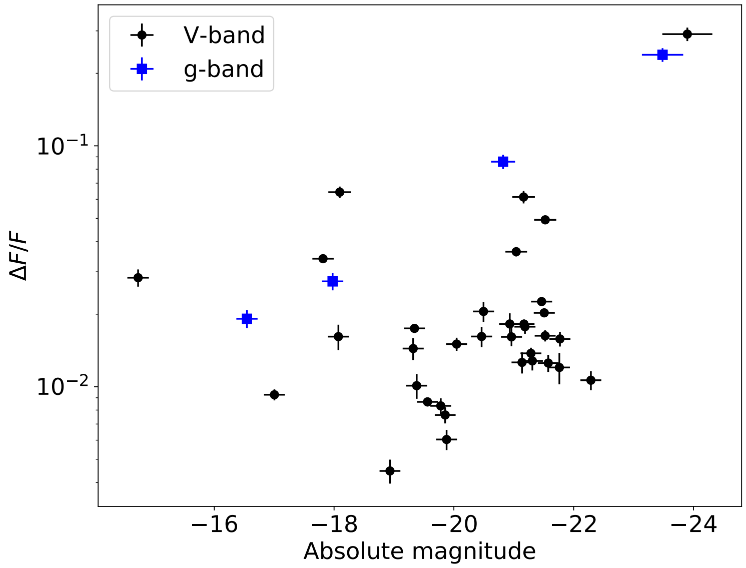

Figure 2.2: Fractional flux variability versus absolute magnitude of AGN candidates. Three objects are classified as AGN candidates in both V- and g-band, and for these objects, both V- and g-band variabilities are plotted. The variability amplitude of these objects agrees to within a factor of 3.

(e.g., di Clemente et al. 1996; Vanden Berk et al. 2004), where $m(t)$ is the magnitude at time t, τ is the time difference between the data pair, and

$$\sigma^2_{noise} = \langle \sigma^2_{\text{err}}(t) + \sigma^2_{\text{err}}(t+\tau) \rangle \tag{2.6}$$

is the noise contribution where $\sigma_{\text{err}}(t)$ is the uncertainty in the measured magnitude. For this study, we use Equation 2.4. The structure function is calculated in bins of width $\Delta \log(\tau/\text{day}) = 0.1$. The uncertainty of the structure function is

$$\Delta \text{SF} = \frac{1}{N_{\text{bin}} \cdot \text{SF}} \sqrt{\sum_{t,\tau} \left\{ [m(t+\tau) - m(t)]^2 \cdot [\sigma^2_{\text{err}}(t+\tau) + \sigma^2_{\text{err}}(t)] \right\}}, \tag{2.7}$$

where N_{bin} is the number of data point pairs in the bin and we are assuming that the uncertainty in σ_{err} is negligible. For small τ, the errors are large, so we discard time scales $\tau < 3$ days.

We next model the structure function as a power law plus a constant, $\text{SF}(\tau) = A\tau^B + C$, representing the contributions from the AGN plus a white noise contribution from the measurement error. We fit the structure function both with an AGN ($A \neq 0$) and just as white noise ($A = 0$), and then use an F-test to determine if the fit with the power-law component is significantly better than the constant fit. The distribution of F-test results is bimodal, with peaks at around 0.02 and 0.40. To filter out the clearly bad candidates while still keeping some borderline candidates, we keep candidates with F-test values < 0.1.

In addition to F-test, we examined the power-law index, B, to determine if the structure function is AGN-like. Quasar variability is a form of red noise, in the sense that the amplitude of the variability initially increases with time scale, but then seems to saturate on longer time scales (years to decades, e.g., MacLeod et al. 2012; Kozłowski 2017). If the DRW was truly the correct model, $B = 0.5$ on short time scales and then a power-law fit will become shallower ($B < 0.5$) on time scales similar to the damping time scale or longer. Schmidt et al. (2010) fit power-law structure functions to the SDSS Stripe 82 quasars and used this to set a selection limit of $B > 0.055$. The Stripe 82 light curves are moderately longer (8 yr) than either the ASAS-SN V- or g-band light curves and poorly sampled on shorter time scales, so we would expect the typical B found here to be larger. We find values that are relatively steep (median $B = 1.5$), but we suspect the exact values are both noisy and affected by systematic errors. We found that an empirical selection cut of $B > 0.3$ appears to work well. Then we examined higher slopes in detail to determine the upper limit. Structure functions with $2 < B < 3$ tend to display an upward trend starting at $\log(\tau/\text{day}) > 2.5$, while the structure functions with smaller slopes start showing such trend earlier. Structure functions with $3 < B < 4$ display the general upward trend, however, the shape is more complicated where the simple power law plus a constant model does not fit well. For $B > 4$, the structure function is mostly flat, with only the last few data points slightly larger than the others, so we set the upper limit of B for the AGN candidate at 4 and a reliable slope measure at 3. Before the final confirmation of a candidate, the light curves and SF are visually inspected.

In addition, high variability objects ($\sigma_{\text{XS}} > 0.03$) that fail the SF criteria are also manually examined. Some candidates are lost because they have more complex structure functions, such as the broken power law. Once an object passes all of these criteria in either V- or g-band, it is considered an AGN candidate. Figure 2.3 shows the light curve and structure function of the three candidates. One of the structure functions has a small peak at $\log(\tau/\text{day}) \sim 2.2$, which corresponds to a time lag of ~ 150 days. This is a common feature observed in many of the structure functions and it is probably an artifact of the seasonal gaps.

2.5. Results

Of the 1218 galaxies, 88 objects in the V-band and 38 objects in the g-band (10 objects in both) display significant variability ($\sigma^2_{\text{XS}}/\Delta(\sigma^2_{\text{XS}}) > 3$). Of these, 36 objects in the V-band and 4 objects in the g-band pass the structure function test. With three of them overlapping in both bands, we find a total of 37 AGN candidates, eight of which were previously classified as AGN by SDSS (Ahumada et al., 2020). Table 2.1 summarizes the candidates, and Figure 2.4 shows the images of six.

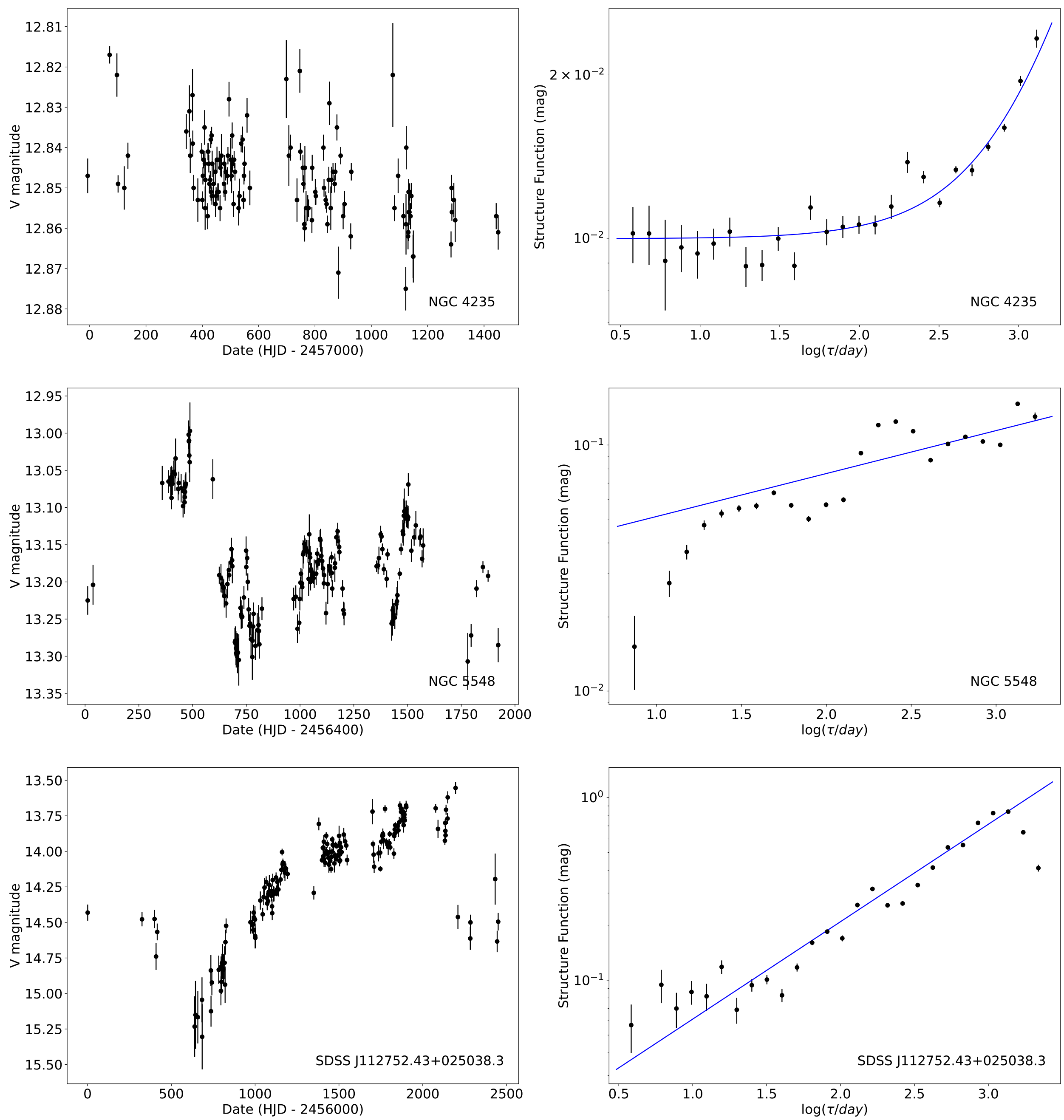

Figure 2.3: The ASAS-SN V-band light curves and the structure functions of NGC 4235 and NGC 5548, two known AGN, and a new variability selected AGN candidate, SDSS J112752.43+025038.3. The blue lines are the best fit structure function models.

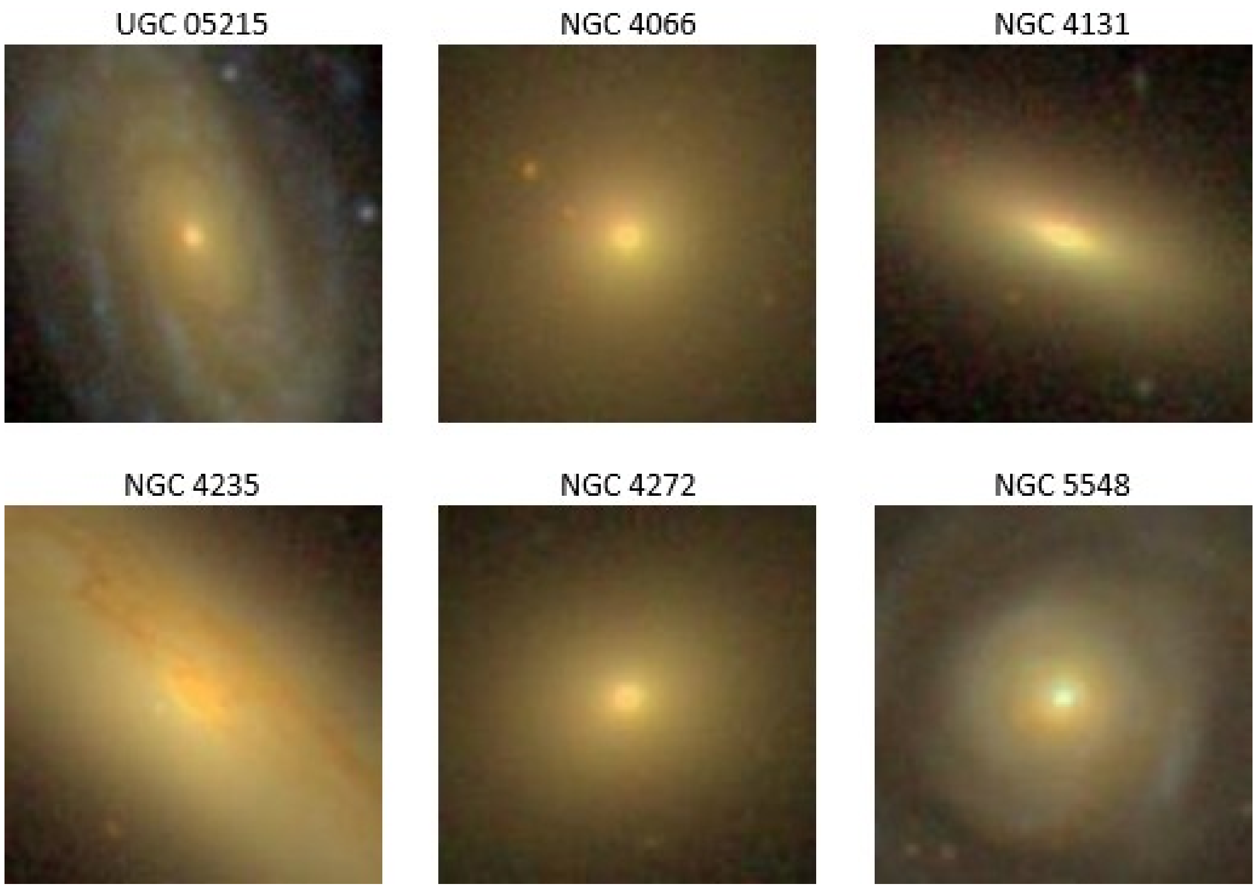

Figure 2.4: The SDSS images (Ahumada et al., 2020) of the 6 of the 37 AGN candidates. Each image is $50'' \times 50''$ with North up and East left.

Table 2.1. Data of AGN candidates from ASAS-SN light curves

Object name	Known AGN	Redshift	Morphology	$\log L/L_\odot$	$\log M_{\rm BH}/M_\odot$	Eddington Ratio
NGC 0863	Yes	0.0261	SA(s)a:	10.63	8.0	1.0×10^{-3}
UGC 02018		0.0206	$SB0^{+}$(rs):	10.30	8.3	7.4×10^{-4}
NGC 0988		0.0050	SB(s)cd:	9.16	7.1	3.4×10^{-3}
NGC 2552		0.0018	SA(s)m?	7.82	5.7	1.6×10^{-3}
UGC 05215		0.0183	Sbc	10.11	8.1	8.1×10^{-4}
NGC 3102		0.0101	$S0^{-}$:	9.65	7.6	7.3×10^{-4}
NGC 3499		0.0051	I0?	9.05	7.0	1.7×10^{-3}
NGC 3594		0.0209	SB0:	10.12	8.1	1.0×10^{-3}
SDSS J112752.43+025038.3		0.0897	Unknown	11.48	9.5	1.4×10^{-2}
NGC 3835		0.0081	Sab: edge-on	9.68	7.6	5.1×10^{-4}
NGC 3886		0.0194	$S0^{-}$:	10.40	8.4	8.7×10^{-4}
NGC 3978	Yes	0.0332	SABbc:	10.84	8.8	5.1×10^{-4}
NGC 4041		0.0040	SA(rs)bc:	9.50	7.5	2.3×10^{-4}
NGC 4043		0.0214	(R)SB(r)0^{0}:	10.39	8.4	9.0×10^{-4}
NGC 4061		0.0245	E:	10.53	8.9	4.7×10^{-4}
NGC 4062		0.0025	SA(s)c	8.73	6.7	4.9×10^{-4}
NGC 4066		0.0245	E	10.51	8.8	5.2×10^{-4}
NGC 4070	Yes	0.0239	E	10.53	8.9	3.8×10^{-4}
NGC 4080		0.0018	Im?	8.10	6.0	1.8×10^{-3}
NGC 4092		0.0225	S?	10.31	8.3	8.0×10^{-4}

Table 2.1 (cont'd)

Object name	Known AGN	Redshift	Morphology	$\log L/L_\odot$	$\log M_{\rm BH}/M_\odot$	Eddington Ratio
NGC 4095		0.0238	E?	10.45	8.8	3.0×10^{-4}
NGC 4131		0.0124	S	9.94	7.9	7.6×10^{-4}
NGC 4158	Yes	0.0082	SA(r)b:	9.66	7.6	7.8×10^{-4}
NGC 4213		0.0224	E	10.44	8.8	3.2×10^{-4}
NGC 4224		0.0086	SA(s)a: edge-on	9.88	7.8	3.0×10^{-4}
NGC 4233	Yes	0.0076	$S0^0$	9.87	7.8	3.9×10^{-4}
NGC 4235	Yes	0.0075	SA(s)a edge-on	9.84	7.2	7.3×10^{-4}
NGC 4241		0.0025	SB(s)cd	8.09	6.0	2.4×10^{-3}
NGC 4272		0.0282	E	10.55	8.9	2.9×10^{-4}
NGC 4944		0.0232	S0/a? edge-on	10.53	8.5	2.4×10^{-3}
NGC 5032		0.0213	SB(r)b	10.34	8.3	1.8×10^{-3}
NGC 5162		0.0227	Scd:	10.38	8.4	6.2×10^{-4}
UGC 08516		0.0034	Scd:	8.66^a	6.5	1.0×10^{-3}
NGC 5273	Yes	0.0036	$SA0^0$(s)	9.16	6.5	1.5×10^{-3}
IC 4345		0.0311	E?	10.63	9.0	3.6×10^{-4}
NGC 5548	Yes	0.0163	(R')SA(s)0/a	10.39	7.8	5.2×10^{-3}
NGC 5633		0.0077	(R)SA(rs)b	9.75	7.7	4.2×10^{-4}

Note. — The objects are listed in ascending order of R.A. The redshift and morphology are from SDSS (Ahumada et al., 2020) and the NASA/IPAC Extragalactic Database (NED) (NASA/IPAC Extragalactic Database (NED), 2019), respectively. The luminosity refers to the object's V-band (or g-band, if noted) luminosity. The central supermassive black hole mass and the Eddington ratio are estimates, as described in section 2.6.3.

[a] g-band luminosity.

2.6. Analysis

2.6.1. Comparison with spectral classification

Since all the targets have SDSS spectra, we can examine and measure several spectral features to further understand the properties of our variability selected AGN sample. Examples of the spectra are shown in Figure 2.5. Only four of the spectra (NGC 0863, NGC 4235, NGC 5273, and NGC 5548) display clear broad Hα emission lines, and all four are previously known AGN. We used the IDL package `SPFIT` (Fu et al., 2018) to fit the spectra. `SPFIT` simultaneously fits the stellar continuum and emission lines, using the Penalized Pixel-Fitting method (pPXF; Cappellari & Emsellem 2004) in three steps. First, the spectral regions with possible emission lines are masked to fit the stellar continuum. Next, the best-fit continuum is subtracted and the remaining emission-line-only spectrum is fit. Finally, the nonlinear optimizer package `MPFIT` (Markwardt, 2009) uses these two models as the initial values for a fit to the full spectrum.

We then use Baldwin–Phillips–Terlevich (BPT) diagrams (Baldwin et al., 1981) to classify and confirm the AGN candidates with emission-line flux measurements with signal-to-ratios > 3 (Figure 2.6). Because `SPFIT` is not designed to fit spectra with broad emission lines, three of four spectra with broad Hα emission are not well fit and are excluded from the BPT analysis. Figure 2.6 shows the BPT diagrams of the AGN candidates with the star forming/AGN dividing line from Kewley et al. (2006). In all three panels, a large fraction of the AGN candidates are confirmed based on the BPT diagnostics: 19 out of 26 for $\log($[O III]/H$\beta)$ vs. $\log($[N II]/H$\alpha)$, 14 out of 26 for $\log($[O III]/H$\beta)$ vs. $\log($[S II]/H$\alpha)$, and 6 out of 10 for $\log($[O III]/H$\beta)$ vs. $\log($[O I]/H$\alpha)$. For the most commonly used $\log($[O III]/H$\beta)$ vs. $\log($[N II]/H$\alpha)$ diagnostic, the AGN confirmation rate is 73%. When including the three other broad line AGN, the AGN confirmation rate is 85%. Out of the total sample of 37 candidates, the confirmation rate is 60%. There exist prior emission line measurements and BPT classifications from SDSS spectra by MPA-JHU (Brinchmann et al., 2004), which give classifications largely consistent with our results.

However, a significant fraction of AGN candidates are classified as star-forming galaxies and it is possible that some of the galaxies in the AGN region of the BPT diagrams are AGN imposters that are actually retired galaxies (Cid Fernandes et al., 2011). Such galaxies can be identified by the equivalent width of their Hα emission line; galaxies with $\mathrm{EW_{H\alpha}} < 3$ Å are considered retired galaxies. If we also require $\mathrm{EW_{H\alpha}} > 3$ Å, the AGN fraction based on the BPT diagrams drops down to 20–40%, suggesting that the emission line diagnostic has its own limitations.

2.6.2. Low-Luminosity AGN

Objects with $L_{\mathrm{H\alpha}} < 10^{40}$ erg s^{-1} are considered LLAGN (Ho et al., 1997a). After manually estimating the Hα luminosity of the broad-line AGN, 30 of 37 candidates–including NGC 5273, a galaxy with broad Hα emission–are classified as LLAGN. Next, we took a closer look at the flux

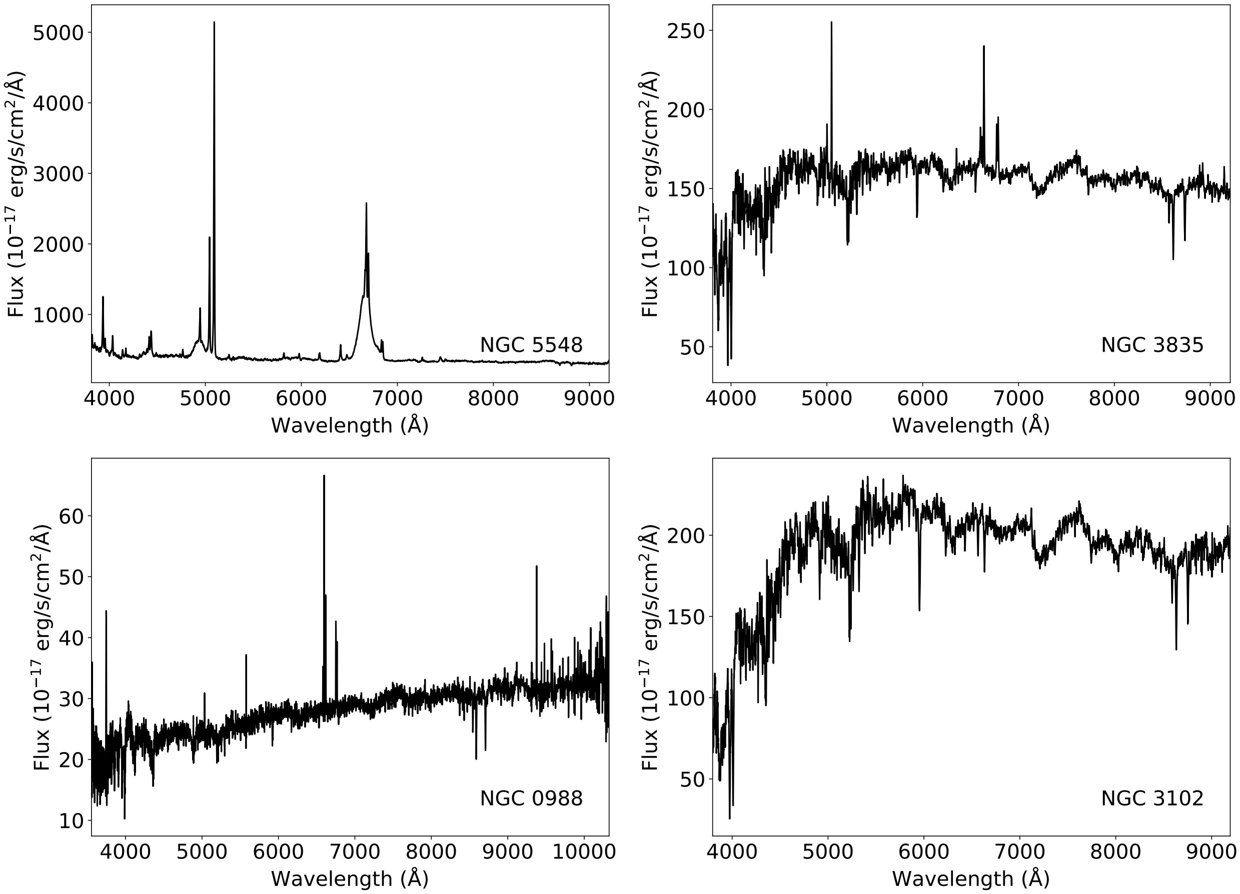

Figure 2.5: SDSS Spectra of several AGN candidates. Top left: a spectrum of the known AGN NGC 5548 showing a clear broad Hα emission line. Top right: a spectrum with a narrow Hα emission line that is classified as an AGN based on its BPT line ratios. Bottom left: a spectrum with a narrow Hα emission line that is not classified as an AGN given its line ratios. Bottom right: a spectrum with weak or absent Hα emission. There are 4, 18, 7, and 8 candidates in each of these categories.

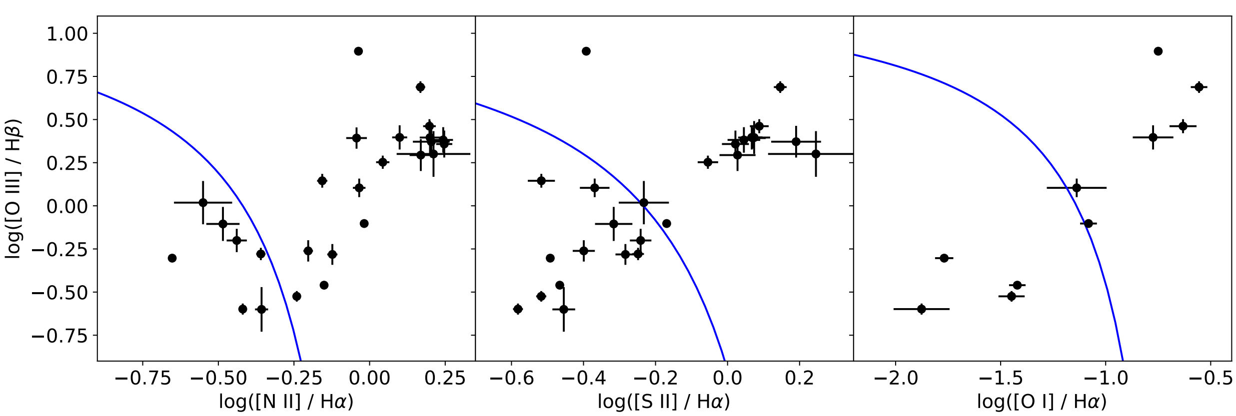

Figure 2.6: BPT diagrams of the AGN candidates. The blue curve is the Kewley et al. (2006) classification line dividing star forming sources (lower right) from AGN (upper right).

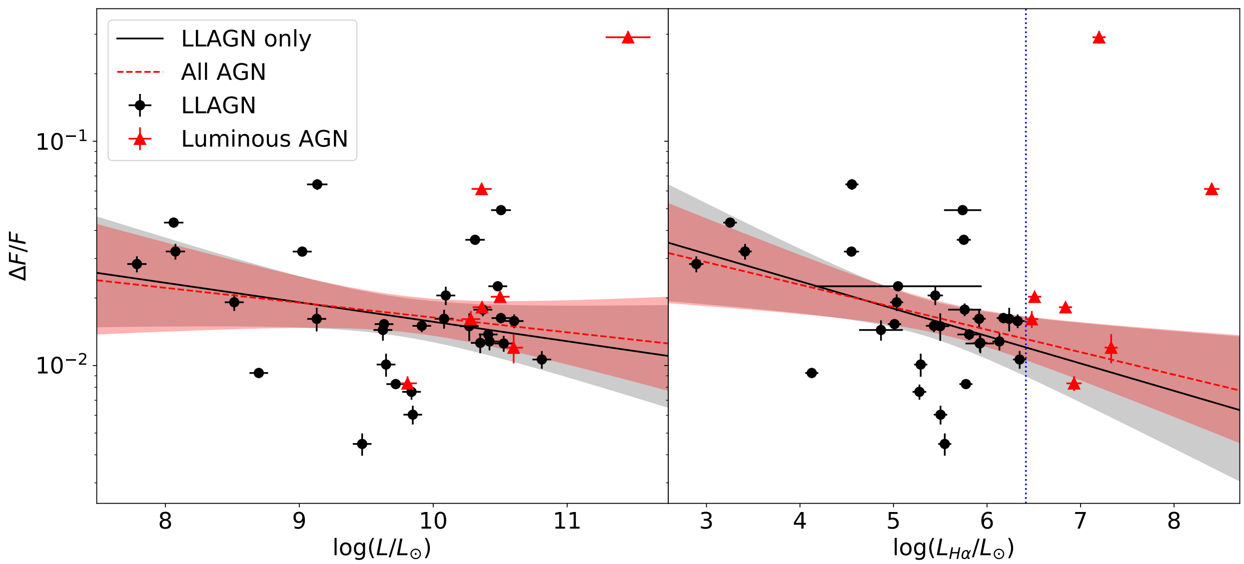

Figure 2.7: Fractional flux variability of the candidates versus host V/g-band (left) and Hα (right) luminosities with the best linear fits (shaded areas represent the 90% confidence regions). The dotted blue vertical line on the right graph is the dividing line for LLAGN ($L_{\mathrm{H}\alpha} = 10^{40}$ erg s^{-1}). The outlier at $\Delta F/F \sim 0.3$ is excluded for both fits, and an additional outlier at $\log(L_{\mathrm{H}\alpha}/L_\odot) \sim 8.5$ is excluded for the $\Delta F/F$ versus $\log(L_{\mathrm{H}\alpha}/L_\odot)$ fit.

variability of the LLAGN compared to the host and the Hα luminosities, as shown in Figure 2.7. Galactic luminosities refer to the V- or g-band luminosities derived from the ASAS-SN photometry and are not bolometric. AGN variability is generally larger for less luminous AGN (e.g., Vanden Berk et al., 2004; MacLeod et al., 2010; Kozłowski et al., 2016). Broadly speaking, our candidates show the expected trends. We also observe that the slope is slightly steeper for the LLAGN, but the difference is not significant given the scatter. There is also a bias against detecting objects with smaller fractional variability.

2.6.3. Black hole mass and Eddington Luminosity

We estimate the mass of the central supermassive black hole using the spheroid luminosity,

$$\log\left(\frac{M_{\mathrm{BH}}}{M_\odot}\right) = \alpha + \beta \log\left(\frac{L_{\mathrm{sph},I}}{10^{11} L_{\odot,I}}\right), \tag{2.8}$$

where $L_{\mathrm{sph,I}}$ is the I-band spheroid luminosity, and $\alpha = 9.11 \pm 1.15$ and $\beta = 1.02 \pm 0.11$ for quiescent galaxies and $\alpha = 8.88 \pm 0.05$ and $\beta = 1.02$ (fixed) for type 1 AGN (Bennert et al., 2021). We estimate $L_{\mathrm{sph,I}}$ by the following procedure. We calculate the absolute magnitude using the mean magnitude in the V- or g-band measured by ASAS-SN, corrected for Galactic extinction (Schlafly & Finkbeiner, 2011) and using Assef et al. (2010) for the K-correction. We also use the SED from Assef et al. (2010) to calculate the $V - I$ color and convert the V-band magnitudes into I-band magnitudes; g-band magnitudes are approximated as V-band magnitudes. Given the low resolution of ASAS-SN data, the flux is assumed to be the flux of the entire galaxy. For spiral galaxies, the flux is dominated by the disk. Bennert et al. (2021) show that the average difference between the spheroid and the disk magnitudes is $\langle m_{\text{sph}} - m_{\text{disk}} \rangle = 0.795$ (Table 4 in Bennert et al. 2021). We use this correction for spiral galaxies and galaxies with unknown morphology. For elliptical galaxies, the entire galaxy is considered to be a spheroid. Then, using the Sun's absolute magnitude in the I-band (Willmer, 2018), each galaxy's I-band spheroid luminosity in terms of solar luminosity is obtained, which is then used to calculate the black hole mass.

The sources of uncertainties in M_{BH} calculation come from both ASAS-SN measurement uncertainties and systematic uncertainties. The average value of black hole mass uncertainties due to measurement uncertainties is 0.07 dex, while the average contribution from systematic uncertainties is 0.5 dex for broad Hα AGN and 1.2 dex for the others. Such discrepancy comes majorly from the spread in α.

Of the six objects previously classified as AGN, M_{BH} has been measured for NGC 0863 and NGC 5548 using reverberation mapping. The measured values of $\log(M_{\text{BH}}/M_{\odot})$ are $7.57^{+0.06}_{-0.07}$ for NGC 0863 (Bentz & Manne-Nicholas, 2018) and $7.51^{+0.23}_{-0.14}$ for NGC 5548 (Pancoast et al., 2014), which are in agreement with our estimates of 8.0 ± 0.5 and 7.8 ± 0.5.

Given the estimated black hole mass, we can calculate the expected Eddington Luminosity, L_{Edd}. We also estimate the Eddington ratio, $\lambda_{\text{Edd}} = L/L_{\text{Edd}}$, from variability. Because of its low resolution, we can only measure the variability of the AGN with ASAS-SN and not its mean flux. MacLeod et al. (2010) find that the variability and Eddington ratio have power-law relation, $\sigma_{\text{XS}} \propto (L/L_{\text{Edd}})^{-0.23}$. This can be scaled to $L/L_{\text{Edd}} \sim 38.0(\Delta F/F_{\text{Edd}})^{1.3}$, assuming the fractional variability is small. Most of our AGN candidates have $\Delta F/F_{\text{Edd}}$ in order of $10^{-4} \sim 10^{-3}$. In this regime, this power-law relation can be approximated as $L/L_{\text{Edd}} \sim 3.0 \times \Delta F/F_{\text{Edd}}$. From the measured luminosity and M_{BH} calculated from reverberation mapping, Pancoast et al. (2014) report that the Eddington ratio of NGC 5548 is 0.017, while for the ASAS-SN light curve, the ratio of the flux variability to Eddington is $\Delta F/F_{\text{Edd}} = 5.2 \times 10^{-4}$. The ratio between these two values is in order of 10^1, so instead of scaling by ~3.0, we estimate the Eddington ratio by

$$\lambda_{\text{Edd}} = 10 \times \frac{\Delta F}{F_{\text{Edd}}}. \tag{2.9}$$

The dependence of this Eddington ratio estimate on the black hole mass is shown in Figure 2.8. The Eddington ratios of the AGN candidates are of order 10^{-4}–10^{-2}, and all the LLAGN identified based on the Hα luminosity have Eddington ratios in order of 10^{-3} or lower.

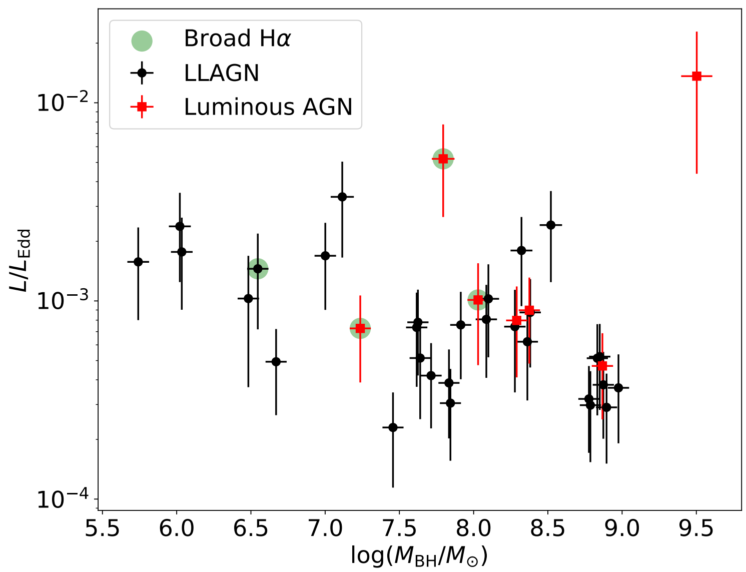

Figure 2.8: Eddington ratio versus black hole mass for the AGN candidates, with the LLAGN/luminous AGN classification based on Hα luminosity. The errors are purely statistical. The systematic uncertainty from converting the ASAS-SN photometry to a black hole mass is about 1.1 dex.

2.7. Discussion and Conclusions

We selected 37 AGN using the ASAS-SN light curves from a sample of 1218 bright ($g < 14$ mag) SDSS galaxies with spectra, although the exact number of candidates depends on analysis choices. To determine whether an object is variable, we calculated its excess variance in magnitudes. We also tried using the normalized excess variance, $\sigma_{\rm NXS} = \sigma_{\rm XS}/\overline{x}^2$, of the flux. This resulted in more objects being considered variable (203 in the V band and 322 in the g band with 103 in both), but none of the additional variable sources had AGN-like structure functions.

We also analyzed the V- and g-band light curves separately and found more AGN candidates in the V-band data, probably because of its longer time span (2000 vs. 600 days). Baldassare et al. (2020) also found that the number of variability selected AGN increases with the length of the light curve. Combining the V and g light curves is difficult because of the need to cross-calibrate them to 0.01 mag or better.

Excluding the seven luminous AGN in our sample, we found 30 LLAGN and constrain the LLAGN fraction to be 2.5% down to a median Eddington ratio of 2×10^{-3}. However, our AGN fraction estimate for the luminous AGN (1%) can be incomplete because known nearby luminous AGN can be excluded as SDSS spectroscopic targets (Strauss et al., 2002). In addition, variability selection can be insensitive to Type II AGN where there is no obvious emission from the accretion disk.

Compared to recent variability selected AGN studies, Baldassare et al. (2020) have the most consistent results with our study. Baldassare et al. (2020) measured the light curves of galaxies using Palomar Transient Factory R-band data and compared them to the DRW model to identify AGN. From the sample of $\sim 50,000$ galaxies, they identified $\sim 1\%$ as variability selected AGN. When they analyzed the available spectra, they found that approximately 60% of their candidates were in the star-forming region on the BPT diagram. They also found that those in the star-forming region tended to have lower stellar mass. They also used the DRW parameters to estimate the black hole mass and found that most of their AGN candidates have $M_{\rm BH} \sim 10^6 M_{\odot}$–$10^8 M_{\odot}$.

Elmer et al. (2020) selected AGN based on their long-term near-infrared variability in the UKIRT Infrared Deep Sky Survey Ultra Deep Survey. They selected objects with $\chi^2 > 30$ for being variable and with AGN-like colors and morphologies. They found 393 variability selected AGN from 152,682 sources or 0.3%, an order of magnitude lower than our fraction, but the typical UKIRT light curves have much lower cadence, at most seven epochs spanning over 7 yr. Many variability selection studies do not use galaxies as the parent sample and so cannot measure the AGN fraction (e.g., Butler & Bloom, 2011; MacLeod et al., 2011; Kumar et al., 2015; Sánchez-Sáez et al., 2019).

Other studies have found that the LLAGN fraction of still lower Eddington ratios is significantly higher. Ho et al. (1997b) report that approximately 43% of nearby galaxies from the Palomar Survey are active, down to Eddington ratios of 10^{-5}–10^{-6}, with over 85% of them having Hα luminosities less than 10^{40} erg s^{-1}. Kewley et al. (2006) analyzed SDSS spectra of over 80,000 emission-line galaxies and identified 17% of them as AGN. From the same AGN sample, Kauffmann et al. (2003) use the [O III] luminosity to identify LLAGN, down to $\log(L_{\rm [O\,III]}/L_{\odot}) = 7$. With this limit, over 80% of the sample was classified as LLAGN.

To summarize, we used variability to search 1218 bright ($g < 14$ mag) SDSS galaxies with spectra for AGN activity and found that

1. Approximately 3% of the galaxies are AGN candidates showing variability and a red noise structure function.

2. Of the AGN candidates, 60–80% are confirmed as AGN using SDSS spectra. About 10% are broad-line AGN and 50–70% lie in the AGN region of an emission line diagnostic plane.

3. The LLAGN fraction is 2% down to an Eddington ratio of $\sim 10^{-3}$. The luminous AGN fraction may be incomplete because it can be excluded from the SDSS spectroscopic sample.

The strength of this method is that it requires only photometric data, and large nonspectroscopic surveys can be used to construct the parent galaxy samples, such as SDSS, Pan-STARRS, DES, 2MASS, and WISE, and LSST/Rubin in the near future for fainter and more distant galaxies. With more and deeper data, we can constrain the AGN fraction among galaxies more accurately in the local universe than using the ASAS-SN survey. Furthermore, since the photometric galaxy sample is relatively unbiased compared to the spectroscopic sample, the variability selection can constrain the AGN fraction to certain Eddington limits including the luminous AGN and LLAGN.

2.8. Acknowledgments

We thank the anonymous referee for helpful comments and suggestions. We acknowledge the financial support from the NASA ADAP program NNX17AF26G. H.F. acknowledges support from NSF grants AST-1614326 and AST-2103251. C.S.K. and K.Z.S. are supported by NSF grants AST-1908570 and AST-1814440. We thank Las Cumbres Observatory and its staff for their continued support of ASAS-SN. ASAS-SN is funded in part by the Gordon and Betty Moore Foundation through grants GBMF5490 and GBMF10501 to the Ohio State University and also funded in part by the Alfred P. Sloan Foundation grant G-2021-14192.

CHAPTER 3

Multi-wavelength and Environmental Properties of Variability Selected Low Luminosity Active Galactic Nuclei

This chapter is the reproduction of Yuk et al. (2025), arXiv e-prints, arXiv:2501.17844, accepted for publication in ApJ.

3.1. Abstract

We present the multi-wavelength and environmental properties of 37 variability-selected active galactic nuclei (AGNs), including 30 low luminosity AGNs (LLAGNs), using a high cadence time-domain survey (ASAS-SN) from a spectroscopic sample of 1218 nearby bright galaxies. We find that high-cadence time-domain surveys uniquely select LLAGNs that do not necessarily satisfy other AGN selection methods, such as X-ray, mid-IR, or BPT methods. In our sample, 3% of them pass the mid-infrared color based AGN selection, 18% pass the X-ray luminosity based AGN selection, and 60% pass the BPT selection. This result is supported by two other LLAGN samples from high-cadence time-domain surveys of TESS and PTF, suggesting that the variability selection method from well-sampled light curves can find AGNs that may not be discovered otherwise.These AGNs can have moderate to small variability amplitudes from the accretion disk, but many of them lack strong corona, emission lines from the central engine, or accretion power to dominate the mid-IR emission. The X-ray spectra of a sub-sample of bright sources are consistent with a power law model. Upon inspecting the environments of our sample, we find that LLAGNs are more common in denser environments of galaxy clusters in contrast with the trend established in the literature for luminous AGNs at low redshifts, which is broadly consistent with our analysis result for luminous AGNs limited by a smaller sample size. This contrast in environmental properties between LLAGN and luminous AGNs suggests that LLAGNs may have different trigger mechanisms.

3.2. Introduction

It is now believed that most galaxies have supermassive black holes (SMBHs) at their centers (e.g., Kormendy & Richstone, 1995; Magorrian et al., 1998). Some of them are known to be actively accreting nearby matter, releasing a tremendous amount of energy during the process. These are known as active galactic nuclei (AGNs) and they are some of the most energetic phenomena in the observable universe. These are fascinating objects to study, as they provide unique opportunities to study accretion physics and galaxy evolution.

Many methods are used to identify AGNs, such as emission lines in optical spectra (e.g., Baldwin et al., 1981; Kewley et al., 2006), X-ray luminosity (e.g., Mushotzky, 2004), UV/optical colors (e.g., Schmidt & Green, 1983; Richards et al., 2002), mid-infrared colors (e.g., Stern et al., 2005; Assef et al., 2010; Stern et al., 2012), and radio emission (e.g., Tadhunter, 2016). Among many methods, variability selection (e.g., MacLeod et al., 2011; Baldassare et al., 2020; Yuk et al., 2022) has been gaining popularity in recent years with the availability of time-domain surveys.

Variability across the wide range of electromagnetic spectrum and timescales is one of the defining features of AGNs. However, the mechanism behind is still a topic of debate. There exist many theories on the origin of AGN variability, including thermal processes (e.g., Lightman & Eardley, 1974; Shakura & Sunyaev, 1976; Kelly et al., 2009), accretion disk instabilities (e.g., Rees, 1984; Kawaguchi et al., 1998; Trèvese & Vagnetti, 2002), photon reprocessing (e.g., Haardt & Maraschi, 1991; McHardy et al., 2018), and supernovae (e.g., Terlevich et al., 1992; Aretxaga et al., 1997). What is known, however, is that the AGN variability is stochastic (e.g., Kelly et al., 2009; MacLeod et al., 2010). This key characteristic is used to determine whether a galaxy displays an AGN-like variability. For example, MacLeod et al. (2011) used a damped random walk to model the AGN variability and analyzed the Sloan Digital Sky Survey (SDSS) Stripe 82 light curves of $\sim$10,000 variable objects to determine which ones display AGN-like variability. They were able to achieve the completeness of $>$90%, showing the robustness of this method.

Variability selection is becoming a more powerful tool as more high-quality photometry data is becoming available, enabling the discovery of more AGNs, especially in the low-luminosity regime. Many early variability selection studies used the SDSS Stripe 82 light curves (e.g., Sesar et al., 2007; Schmidt et al., 2010; Butler & Bloom, 2011; MacLeod et al., 2011). On average, the light curves MacLeod et al. (2011) used had over 60 epochs spanning over 10 years. Studies that followed used larger light curve databases. Sánchez-Sáez et al. (2019) used QUEST-La Silla Survey light curves which had about 120 epochs over 3.5 years on average. Baldassare et al. (2020) used Palomar Transient Factory (PTF) light curves with about 65 epochs over 4 years on average. Yuk et al. (2022) used All-Sky Automated Survey for SuperNovae (ASAS-SN) light curves with about 280 epochs over 5.5 years in V-band and 180 epochs over 1.6 years in g-band on average. Treiber et al. (2023) used the high cadence Transiting Exoplanet Survey Satellite (TESS) light curves with more than 1000 epochs over 30 days. With the better-sampled light curves, these new variability studies have selected AGNs with moderate to small variability amplitudes and are able to probe the low luminosity AGN (LLAGN) population. Variability-based AGN selection in infrared (IR) light curves also demonstrates the evolution of this method. There are many studies on IR variability of AGNs (e.g., Neugebauer et al., 1989; Sánchez et al., 2017; Son et al., 2022). However, it was only recently that IR variability selection became a viable method to find AGNs, as surveys gathered sufficient data (e.g., Elmer et al., 2020; Green et al., 2024).

LLAGNs are an interesting subset of AGNs, as they are speculated to have different trigger mechanisms (e.g., Hopkins & Hernquist, 2009; Hopkins et al., 2014) and accretion structure (e.g., Ho et al., 1997c; Nicastro, 2000; Laor, 2003; Elitzur & Shlosman, 2006). LLAGNs are traditionally selected using the BPT or X-ray methods (e.g., Kewley et al., 2006; Pellegrini et al., 2007; Ho, 2008; Wrobel et al., 2008), and variability adds an additional channel (e.g., Yuk et al., 2022; Messick et al., 2023; Treiber et al., 2023; Wasleske & Baldassare, 2023).

AGN population and evolution are also observed to have environmental dependence. Several studies report that the AGN fraction among galaxies in clusters is lower than that of among field galaxies at low redshifts (e.g., Kauffmann et al., 2004; Koulouridis & Plionis, 2010; Lopes et al., 2017; Mishra & Dai, 2020; Koulouridis et al., 2024). Within a galaxy cluster, the AGN fraction is observed to increase with the distance from the cluster center (e.g., Koulouridis et al., 2018, 2024). However, there are also other studies that observe no significant correlation between the local galaxy density and the AGN fraction (e.g., Miller et al., 2003; Silverman et al., 2009; Pimbblet et al., 2013). Man et al. (2019) find that the AGN fraction decreases with increasing overdensity of nearby galaxies, but is less dependent on the number of nearby star-forming galaxies. At higher redshifts, the overall AGN fraction is observed to increase (e.g., Eastman et al., 2007; Haggard et al., 2010; Martini et al., 2013; Yang et al., 2018). Eastman et al. (2007) report that the AGN fraction in clusters increases more rapidly with redshift than the field AGN fraction.

In this study, we examine the multi-wavelength and environmental properties of the galaxy and variability selected AGN sample of Yuk et al. (2022), where 70% of their AGN candidates are LLAGNs. From this analysis, we seek to constrain the overlap fraction among different AGN selection methods, and AGN fractions among field and cluster galaxies, especially for LLAGNs. In Section 3.3, we introduce the sample and the data used for this study. In section 3.4, we describe the methods we use to analyze. In Section 3.5, we present the results. In Section 3.6, we discuss the implications of the results. We summarize the results and conclusion in Section 3.7. For this study, we assume the ΛCDM cosmological model with $\Omega_\Lambda = 0.7$, $\Omega_M = 0.3$, and $H_0 = 70$ km s^{-1} Mpc^{-1}.

3.3. Data

Yuk et al. (2022) analyzed the All-Sky Automated Survey for SuperNovae (ASAS-SN) light curves of 1218 local galaxies. These galaxies are from the Sloan Digital Sky Survey (SDSS) galaxy catalog were selected with two criteria: SDSS g-band PSF magnitude brighter than 14 and have SDSS spectra available. These galaxies are nearby, where 98% of them have the redshift of less than 0.05. They measured the excess variance and classified targets with 3 sigma or above to be variable. Then they used structure function to determine if a given light curve has an AGN-like variability by fitting a power-law with white noise model. They found 37 of them to be variability-selected

AGNs, and classified 30 of them to be LLAGNs by using the Hα luminosity ($L_{\mathrm{H}\alpha} < 10^{40}$ erg s^{-1}). Upon analyzing the spectra, they found that about 10%-30% of the variability selected AGNs lie in the star-forming region in BPT diagrams, suggesting that the variability selection method can find AGNs that spectral classifications may miss. We note that the luminous AGN sample may be incomplete because the SDSS spectroscopic sample can exclude local luminous AGNs (Strauss et al., 2002). However, the comparisons of LLAGN or luminous AGN in different environments are not affected by this bias. We further study the infrared, X-ray, and environmental properties of this AGN sample.

For the infrared analysis, we use the data from Wide-field Infrared Survey Explorer (WISE; Wright et al. 2010). WISE launched in 2009 and surveyed the entire sky in four infrared bands, $W1$, $W2$, $W3$, and $W4$, with the central wavelengths at 3.4, 4.6, 12, and 22 μm, respectively. Its primary mission lasted until February 2011 and entered hibernation. In 2013, it was reactivated as NEOWISE and continued observations until 2024, which observed only in $W1$ and $W2$ bands. We specifically use the AllWISE catalog, which is the catalog of pre-hibernation data, as it includes more bands. WISE catalogs are available on NASA/IPAC Infrared Science Archive.

For X-ray analysis, we primarily used the data from the extended ROentgen Survey with an Imaging Telescope Array (eROSITA) which was built for an all-sky survey. The German eROSITA Consortium released the data to the public for the western galactic hemisphere ($179.9423568 < l < 359.94423568$) on the eROSITA-DE Data Release 1 (Merloni et al., 2024). To supplement, we also searched for X-ray counterparts to our variability selected AGNs in the High Energy Astrophysics Science Archive Research Center (HEASARC) archive for Chandra, Swift, and XMM-Newton data.

To analyze the environment of the sample, we used two different catalogs. First is the catalog of galaxy clusters by Wen & Han (2024) (WH24). WH24 includes approximately 1.58 million galaxy clusters within the redshift of 1.5 based on the Dark Energy Spectroscopic Instrument (DESI) Legacy Imaging Surveys. Wen & Han (2024) also report the cluster redshifts, where about 330,000 of them are spectroscopic. WH24 covers most of the sky except for the galactic plane. At redshifts comparable to the sample ($z \lesssim 0.10$), the number of galaxy clusters in WH24 is 4955, where 56% of them having spectroscopic redshift measurements. Second is the NASA Sloan Atlas (NSA), which is a catalog of local galaxies ($z < 0.15$) derived from SDSS data (Abdurro'uf et al., 2022). Both WH24 and NSA surveys encompass the survey area of our galaxy sample, so there is no significant incompleteness issue from the sky coverage for our environment analysis.

3.4. Methods

3.4.1. Infrared classification

AGNs are observed to have different spectra compared to quiescent galaxies. Quiescent galaxies, dominated by stellar emission, display blackbody spectra with a wide peak in the optical and near-IR wavelengths. In contrast, AGN spectra, with the accretion disk emission, has the shape of a power law. This makes AGNs redder in mid-IR and bluer in UV-optical. The different shapes of spectra allows colors to be a viable tool to identify AGNs. Assef et al. (2010) analyzed the mid-infrared colors of galaxies and devised a set of criteria to select AGNs using WISE colors. Their criteria are:

$$W1 - W2 > 0.85, \tag{3.1}$$

$$W3 - W4 > 2.1, \tag{3.2}$$

and

$$W1 - W2 > 1.67(W3 - W4) - 3.41, \tag{3.3}$$

where $W1$, $W2$, $W3$, and $W4$ are Vega magnitudes in the WISE wavelength bands. There are a few other studies reporting different versions of mid-IR color selection criteria. So, we also check the criteria of Jarrett et al. (2011), Mateos et al. (2012), Stern et al. (2012), Blecha et al. (2018), and Hviding et al. (2022).

3.4.2. X-ray detection

Many AGNs are known to be strong sources of X-ray emission from the energetic corona above the accretion disk. X-ray luminosity of 10^{42} erg s^{-1} is commonly used as the threshold to determine if a galaxy contains an AGN (Mushotzky, 2004).

We examined eROSITA-DE source catalog to check for any detections from our sample. Out of the 1218 sample galaxies, 614 of them are within this hemisphere, 22 of which are the variability selected AGNs. We computed the X-ray luminosity based on the flux in energy range of 0.2–8 keV. For non-detections, we obtained the upper limits in 0.2–5 keV energy range (Tubín-Arenas et al., 2024). With the X-ray flux and redshift, we calculated the X-ray luminosity with K-correction and galactic absorption correction.

In addition to eROSITA-DE, appropriate Chandra observations have been reduced and analyzed using the most recent version of the Chandra Interactive Analysis of Observations tool, CIAO 4.17, and calibration database CALDB 4.11.6. We started by downloading and reprocessing Chandra data, followed by cutting out small 60×60 arcsecond square images centered on galaxies of interest. We searched for nuclear X-ray excess emission by using the circular aperture as a source region extraction with the radius equal to the point spread function evaluated at the 90% enclosed fraction count level, and a source-free annular aperture as a background region with an inner and outer radius of 10″ and 15″, respectively.

We also manually queried the HEASARC for more archival X-ray flux data of the variability selected AGNs. Specifically, we checked the Second Swift-XRT Point Source Catalog (2XSPS; Evans et al. 2020) and the XMM-Newton Serendipitous Source Catalog (XMMSSC; Webb et al. 2020). 2XSPS data was taken in four energy bands, 0.3–10 keV, 0.3–1 keV, 1–2 keV and 3–10 keV. The observed and unabsorbed fluxes in 0.3-10 keV were estimated by fitting a power-law and APEC models. XMMSSC data was taken in five energy bands, 0.2–0.5 keV, 0.5–1.0 keV, 1.0–2.0 keV, 2.0–4.5 keV, and 4.5–12 keV. The flux in each band was calculated individually and reported in the catalog alongside the combined flux in 0.2-12 keV.

As all four X-ray data sets are in different energy bands, for comparison, we converted all Chandra, Swift, and XMM-Newton fluxes as well as eROSITA upper limits into unabsorbed fluxes in 0.2–8 keV using Portable, Interactive Multi-Mission Simulator (PIMMS). We assumed a power law model for the conversion. For Chandra, we used the photon indices we derived from spectral fitting, while we used the photon index of 1.9 for Swift and XMM-Newton.

3.4.3. AGN environment

We examined the global and local environment of the sample to check for the AGN fraction's environmental dependence, where we refer to global as a region equivalent to a cluster or group size and local as the region containing the nearest neighbors of the source.

We used two methods to check the global environment. First, we checked if the sample belongs to a galaxy cluster. For this, we used the WH24 catalog. Because photometric redshifts typically have large uncertainties, it is difficult to precisely measure the physical distance between the WH24 clusters and the sample galaxies. Because of this, to avoid incompleteness, we use a 2-D matching method. For a given sample galaxy, we check WH24 clusters within a redshift difference of ± 0.05 of the target galaxy. Then we check the angular separation that corresponds to 2 Mpc given its distance. Using this method, we determined whether the galaxies in the sample are in clusters. To check the robustness of the redshift range of ± 0.05, we also tested with ± 0.03.

Second, we checked the number of galaxies within 2 Mpc. We used NSA for this analysis. Since the sample and the NSA galaxies have spectroscopic redshift measured, it is possible to calculate the distance from a sample galaxy to catalog galaxies by combining the angular separation and redshift offset.

To examine the local environment, we computed two parameters using the NSA galaxies: distance to the nearest galaxy and the tidal index. The tidal index is a measurement of galaxy interactions (e.g., Karachentsev & Makarov, 1999; Karachentsev et al., 2004; Pearson et al., 2016), essentially the density of stellar mass in a sphere to the nearby massive member. We use the version

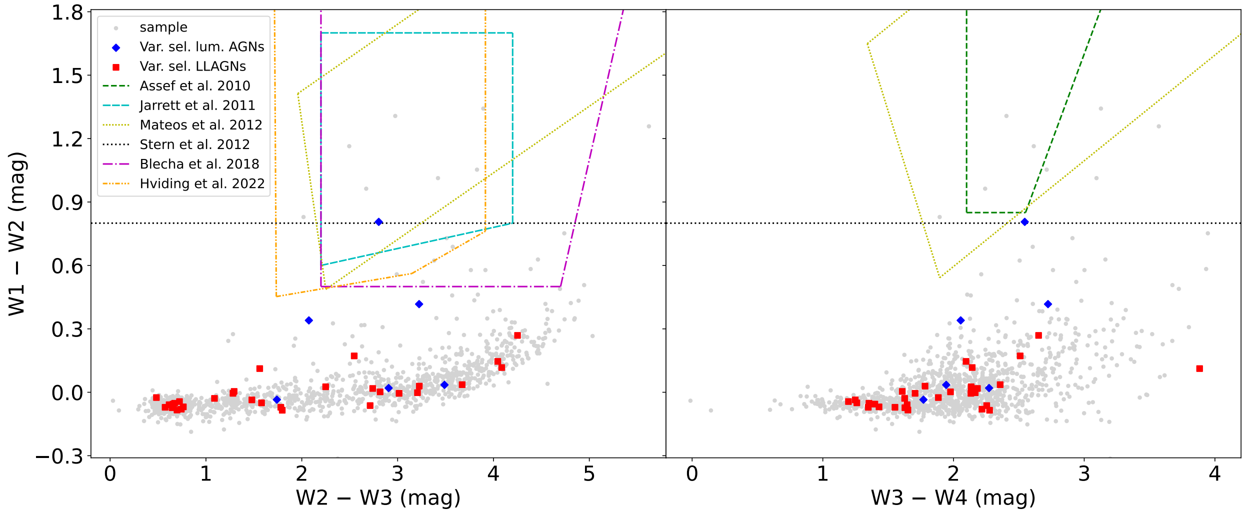

Figure 3.1: WISE color distributions of the variability selected AGNs and their parent galaxy sample with the IR color-based AGN selection boundaries labeled. Out of 36 variability selected AGNs with WISE measurements in all 4 wavelength bands, only 1 is classified as an AGN by any of the criteria.

of the tidal index by Pearson et al. (2016),

$$\Theta = \log\left(\frac{M_*/(10^{11}M_\odot)}{(D/\text{Mpc})^3}\right), \tag{3.4}$$

where M_* is the stellar mass of the neighboring galaxy and D is the distance to that galaxy. For each galaxy in the sample, we computed the tidal index with all NSA galaxies and took the maximum value. As the tidal index accounts for only the main disturber, we also explore taking account of all galaxies in the catalog by computing $\Theta_{\text{sum}} = \log[\Sigma(M_*/D^3)]$.

3.5. Results

3.5.1. Infrared classification

1187 out of 1218 total targets (36 out of 37 variability selected AGNs) have WISE data available. The infrared color-color diagram is shown in Figure 3.1. We find that 3 to 16 targets are classified as AGNs based on different criteria, where only 1 of them is a variability selected AGN. In other words, only about 3% of the variability selected AGNs are classified as IR AGNs. We individually examined the ASAS-SN light curves of galaxies that are classified as AGNs by IR colors but not by variability selection and found that they do not have significant variability above the detection threshold to be included in the variability-selected AGN sample.

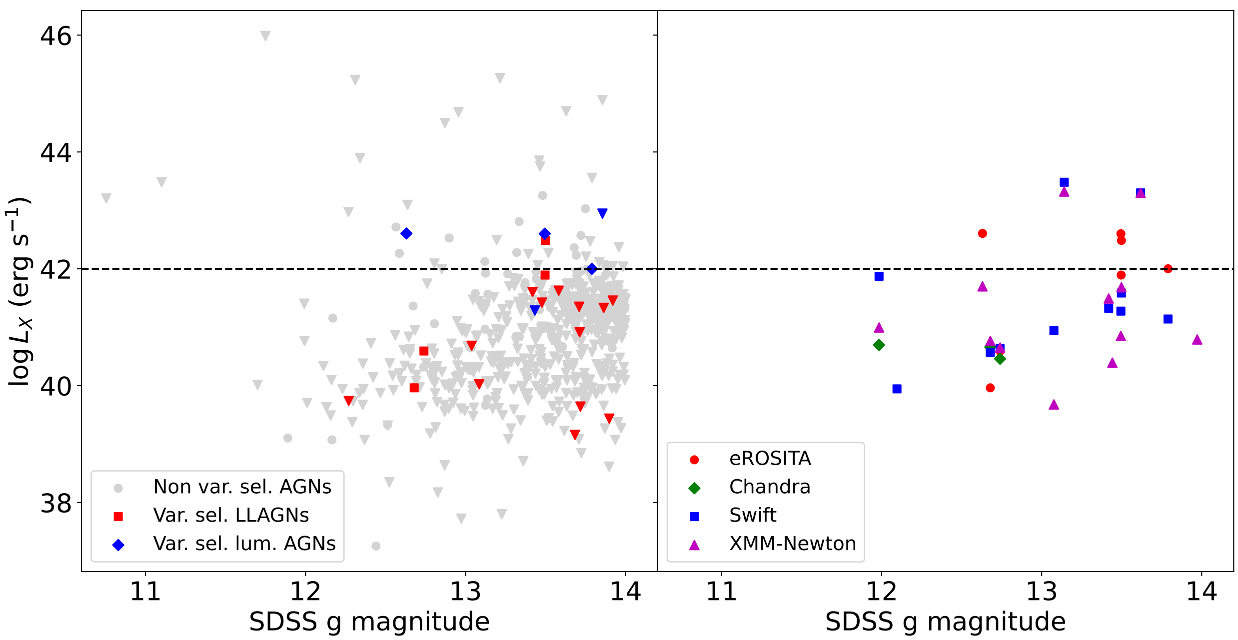

Figure 3.2: Left: X-ray luminosity distribution of the variability selected AGNs and their parent galaxy sample based on eROSITA-DE data. The red squares, blue diamonds, and gray circles represent the X-ray detections of variability selected LLAGNs, luminous AGNs, and galaxies. The upper limits are labeled with downward triangles. Out of 22 variability selected AGNs in the eROSITA-DE hemisphere, 7 had detections, and 3 are bright enough to be classified as AGNs. Right: X-ray luminosity distribution of the variability selected AGNs from different X-ray databases. The dashed line indicates the luminosity limit for AGNs ($L_X > 10^{42}$ erg s^{-1}).

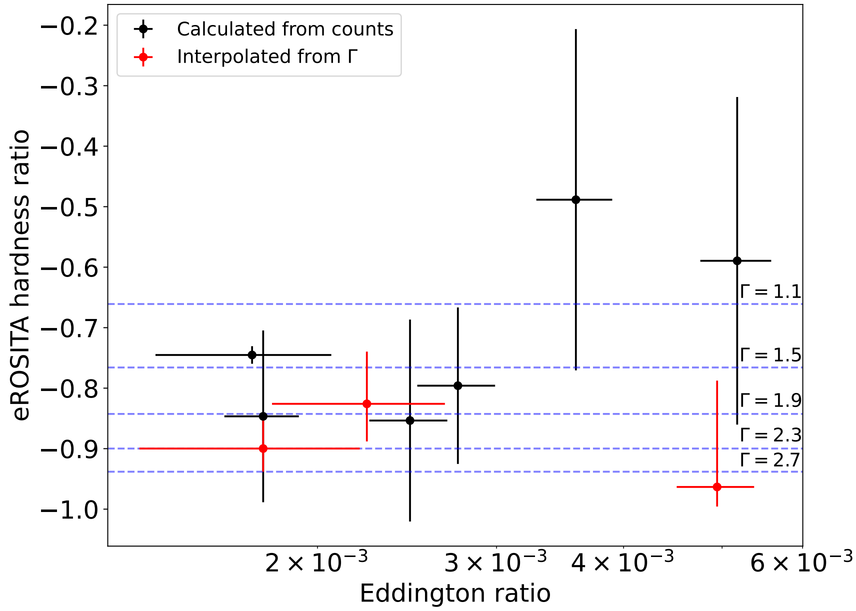

Figure 3.3: Hardness ratio versus Eddington ratio of X-ray detected variability selected AGNs. The Eddington ratios are estimated by scaling variability amplitudes. The blue dashed lines indicate the approximate hardness ratio corresponding to a set of photon indices by assuming a powerlaw model modified by Galactic absorption. Red points show the photon indices of three sources from the spectral fits of Chandra data, converted to equivalent eROSITA hardness ratios.

3.5.2. X-ray detection

We find that 76 of 614 targets in the western galactic hemisphere (7 out of 22 variability selected AGNs in that hemisphere) have eROSITA detections. The variability selected AGNs with eROSITA detections are NGC 4043, NGC 4061, NGC 4066, NGC 4224, NGC 4233, NGC 4235, and NGC 5162. 16 sources, including 4 of the variability selected AGNs (NGC 4043, NGC 4061, NGC 4066, and NGC 4235) have the X-ray luminosity greater than 10^{42} erg s^{-1}. When checking the upper limits, we find that 24 targets potentially have the X-ray luminosity of $> 10^{42}$ erg s^{-1}, where 1 of them is a variability selected AGN. The distribution of eROSITA X-ray luminosity is shown in Figure 3.2 left.

We also calculated additional X-ray properties of the variability selected AGNs. We computed the hardness ratio,

$$HR = \frac{C_H - C_S}{C_H + C_S}, \tag{3.5}$$

where C_H and C_S are photon counts in hard and soft bands, respectively, with the boundary at 2 keV. From the 7 variability selected AGNs with X-ray detections, one of them did not have sufficient counts to compute this ratio. We plotted hardness ratio against Eddington ratios in Figure 3.3.

From Chandra archive, we find three significantly detected point-like nuclear source in galaxies

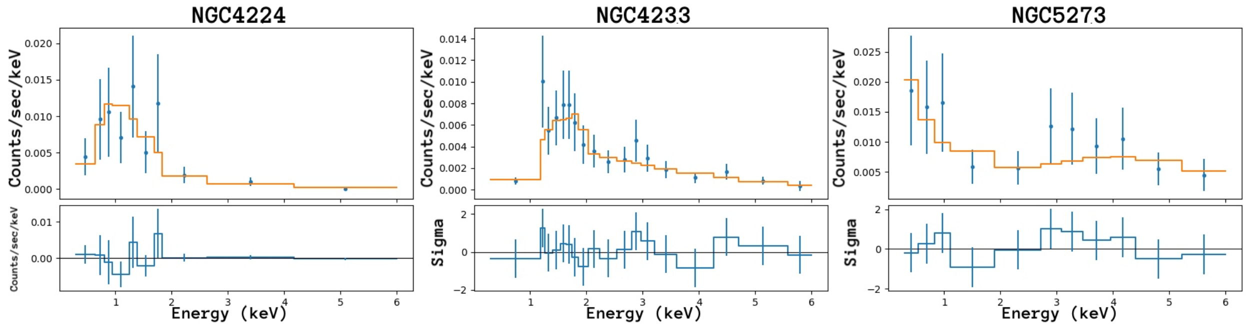

Figure 3.4: The Chandra spectral fits for NGC 4224, NGC 4233, and NGC 5273 with a power law model modified by Galactic absorption, where the photon index is constrained as 2.3 ± 0.4, 1.8 ± 0.4, and 3.1 ± 1.5, respectively. An additional blackbody component is needed to fit the NGC 5273 spectrum. The bottom panels show the residuals.

NGC 4224, NGC 4233, and NGC 5273, and detected with 28±5, 180±13, and 100±10 photons. For Chandra sources, we performed spectral fitting analysis of the three sources using SHERPA, CIAO's modeling and fitting application. NGC 4233 was fitted using the simple absorbed power law model, xsphabs×powlaw1d, while NGC 5273 required an additional black body component, xsphabs×(powlaw1d+xsbbody). NGC 4224, the faintest source with only 28 net counts, was fitted using the simple absorbed power law model, xsphabs×powlaw1d, and Cstat maximum likelihood function based on the Cash statistics (Cash, 1979). This approach is usually adopted for low-count X-ray spectral fitting (Marchesi et al., 2016; Mezcua et al., 2018; Mićić et al., 2022) since it does not require count binning in the spectral analysis. We find values of photon indices for NGC 4224, NGC 4233, and NGC 5273 to be 2.3 ± 0.4, 1.8 ± 0.4, and 3.1 ± 1.5, and their unabsorbed 0.2–10 keV luminosities to be 3×10^{40}, 5×10^{40}, and 5×10^{40} erg s^{-1}. The spectral fits of these three targets are shown on Figure 3.4. The hardness ratio and X-ray spectral analysis results show that the X-ray spectra of these LLAGN are consistent with power law models with photon indices ranging from 1–3, consistent with other AGNs (e.g., Dai et al., 2004; Saez et al., 2008; She et al., 2018; Panagiotou & Walter, 2020).

From the HEASARC archive, we found 12 sources from XMMSSC and 11 sources from 2SXPS. For targets with multiple entries in a catalog, we took the median flux. The summary of spectral fitting results and AGN X-ray properties is given in Table 3.1 and the distribution of luminosities are shown on Figure 3.2 right. Out of 14 sources with Chandra, Swift, or XMM-Newton detections, only 2 targets, NGC 0863 and NGC 5548, have X-ray luminosity greater than 10^{42} erg s^{-1}.

Table 3.1. Summary of derived values and multi-wavelength properties of variability selected AGNs

Name	$\log M_{\rm BH}$ ($M_\odot$)	$\lambda_{\rm Edd}$	W1−W2 (mag)	W3−W4 (mag)	$\log L_{X,\rm e}$ (erg s^{-1})	$\log L_{X,\rm C}$ (erg s^{-1})	$\log L_{X,\rm S}$ (erg s^{-1})	$\log L_{X,\rm XMM}$ (erg s^{-1})	eROSITA HR	Γ
NGC 0863	8.0	1.0×10^{-3}	0.417	2.723	···	···	43.3	43.3	···	···
UGC 02018	8.3	7.4×10^{-4}	-0.059	1.645	···	···	···	···	···	···
NGC 0988	7.1	3.4×10^{-3}	0.029	1.782	< 40.0	···	···	···	···	···
NGC 2552	5.7	1.6×10^{-3}	0.112	3.883	···	···	···	···	···	···
UGC 05215	8.1	8.1×10^{-4}	-0.005	2.133	< 41.3	···	···	···	···	···
NGC 3102	7.6	7.3×10^{-4}	-0.073	1.628	···	···	···	···	···	···
NGC 3499	7.0	1.7×10^{-3}	-0.050	1.260	···	···	···	···	···	···
NGC 3594	8.1	1.0×10^{-3}	-0.080	2.218	···	···	···	40.8	···	···
SDSS J1127+0250	9.5	1.4×10^{-2}	···	···	< 42.9	···	···	···	···	···
NGC 3835	7.6	5.1×10^{-4}	0.026	2.135	···	···	40.9	39.7	···	···
NGC 3886	8.4	8.7×10^{-4}	-0.052	1.353	< 41.4	···	···	···	···	···
NGC 3978	8.8	5.1×10^{-4}	0.146	2.096	···	···	···	···	···	···
NGC 4041	7.5	2.3×10^{-4}	0.269	2.651	···	···	39.9	···	···	···
NGC 4043	8.4	9.0×10^{-4}	0.020	2.272	42.0	···	41.1	···	-0.59 ± 0.27^a	···
NGC 4061	8.9	4.7×10^{-4}	-0.035	1.770	42.6	···	41.3	40.9	-0.85 ± 0.17^a	···
NGC 4062	6.7	4.9×10^{-4}	-0.063	2.254	< 39.7	···	···	···	···	···
NGC 4066	8.8	5.2×10^{-4}	-0.084	1.651	42.5	···	41.6	41.7	-0.80 ± 0.13^a	···
NGC 4070	8.9	3.8×10^{-4}	-0.005	1.706	< 41.6	···	41.3	41.5	···	···
NGC 4080	6.0	1.8×10^{-3}	-0.002	2.166	< 39.2	···	···	···	···	···
NGC 4092	8.3	8.0×10^{-4}	0.035	1.944	< 41.3	···	···	···	···	···
NGC 4095	8.8	3.0×10^{-4}	-0.036	1.248	< 41.5	···	···	···	···	···
NGC 4131	7.9	7.6×10^{-4}	-0.044	1.196	< 40.9	···	···	···	···	···
NGC 4158	7.6	7.8×10^{-4}	0.002	1.977	< 40.7	···	···	···	···	···
NGC 4213	8.8	3.2×10^{-4}	-0.071	1.348	< 41.4	···	···	···	···	···

Table 3.1 (cont'd)

Name	$\log M_{\rm BH}$ $(M_\odot)$	$\lambda_{\rm Edd}$	W1−W2 (mag)	W3−W4 (mag)	$\log L_{X,\rm e}$ (erg s^{-1})	$\log L_{X,\rm C}$ (erg s^{-1})	$\log L_{X,\rm S}$ (erg s^{-1})	$\log L_{X,\rm XMM}$ (erg s^{-1})	eROSITA HR	Γ
NGC 4224	7.8	3.0×10^{-4}	0.004	1.608	40.6	40.5	40.6	40.7	-0.85 ± 0.14^{a}	2.3 ± 0.4^{b}
NGC 4233	7.8	3.9×10^{-4}	-0.029	1.626	40.0	40.7	40.6	40.8	$-0.83^{+0.09}_{-0.06}$ ^{b}	1.8 ± 0.4^{b}
NGC 4235	7.2	7.3×10^{-4}	0.340	2.055	42.6	⋯	⋯	41.7	-0.75 ± 0.01^{a}	⋯
NGC 4241	6.0	2.4×10^{-3}	0.018	2.183	< 39.4	⋯	⋯	⋯	⋯	⋯
NGC 4272	8.9	2.9×10^{-4}	-0.025	1.884	< 41.6	⋯	⋯	⋯	⋯	⋯
NGC 4944	8.5	2.4×10^{-3}	-0.056	1.398	⋯	⋯	⋯	40.4	⋯	⋯
NGC 5032	8.3	1.8×10^{-3}	-0.071	1.552	⋯	⋯	⋯	⋯	⋯	⋯
NGC 5162	8.4	6.2×10^{-4}	-0.085	2.276	41.9	⋯	⋯	⋯	-0.49 ± 0.28^{a}	⋯
UGC 08516	6.5	1.0×10^{-3}	0.036	2.357	< 39.6	⋯	⋯	⋯	⋯	⋯
NGC 5273	6.5	1.5×10^{-3}	0.172	2.510	⋯	40.7	41.9	41.0	$-0.96^{+0.18}_{-0.03}$ ^{b}	3.1 ± 1.5^{b}
IC 4345	9.0	3.6×10^{-4}	-0.069	1.430	⋯	⋯	⋯	⋯	⋯	⋯
NGC 5548	7.8	5.2×10^{-3}	0.806	2.545	⋯	⋯	43.5	43.3	⋯	⋯
NGC 5633	7.7	4.2×10^{-4}	0.117	2.143	⋯	⋯	⋯	⋯	⋯	⋯

Note. — [a]Measured from eROSITA data. [b]Measured from Chandra data. SDSS J1127+0250 is short form of SDSS J112752.43+025038.3. The black hole mass and Eddington ratios are estimated by scaling the spheroid luminosity and fractional variability, respectively. The 4 X-ray luminosity columns, $L_{X,\rm e}$, $L_{X,\rm C}$, $L_{X,\rm S}$, and $L_{X,\rm XMM}$, represent the eROSITA, Chandra, Swift, and XMM-Newton luminosities, respectively. The X-ray energy range is 0.2–8 keV. The hardness ratios from Chandra Γ are computed by accounting for the sensitivity differences between the Chandra and eROSITA instruments.

3.5.3. AGN environment

When we check the WH24 catalog, we find that the number of all galaxies in the sample, variability selected LLAGNs, and luminous AGNs that are in a cluster are 620, 23, and 3, respectively, resulting LLAGN and luminous AGN fractions in the fields of 1.2%/0.7% and 3.7%/0.5% in the clusters. When we use the redshift range of $\Delta z = 0.03$ instead of $\Delta z = 0.05$, we find those included source numbers become 440, 21, and 3, respectively. While the number of AGNs in clusters is not strongly affected, the number of galaxies in clusters is reduced significantly, affecting the AGN fraction. Either result, however, displays significant difference between LLAGN fraction in clusters and fields. We present results using the redshift range of $\Delta z = 0.05$ to minimize the potential incompleteness.

The number of NSA galaxies near variability selected AGN within 2 Mpc ranges from 2 to 110, with a median of 15 and a standard deviation of 21. We binned the number of nearby galaxies with bins that would maximize the number of AGNs in each bin. We observe a positive correlation between the LLAGN fraction and the number of galaxies in 2 Mpc. Both global environment parameters suggest that the LLAGN fraction is greater in clusters or denser environments, while such correlation is not observed for luminous AGNs (Figure 3.5).

The local environment parameters do not appear to have a significant correlation with the AGN fraction. The AGN fraction appears to be approximately constant with the distance to the nearest galaxy and the tidal index for both LLAGNs and luminous AGNs (Figure 3.6). The summary of global and local environmental dependence is shown on Table 3.2.

3.6. Discussion

From the multi-wavelength analysis of properties of LLAGN selected from the ASAS-SN survey, we find that the overlap between these AGNs from different selection methods is between a few to 60 percent, 60% from BPT, 3% from mid-infrared colors, and 14% from X-ray luminosity. Our overlap fraction with X-ray classification standard is based on the eROSITA data, as it is an all-sky survey and upper limits are available for non-detections. We also find additional detections from Chandra, Swift, and XMM-Newton. We find the rate of detections above 10^{42} erg s^{-1} for these data sets are 0%, 18%, and 17%, respectively. However, these are accounting only detections of observations on targets that are not randomly selected from the sample, we cannot conclude that these ratios represent the entire sample. Overall, the overlap fractions we obtain are consistent with other analyses of variability selected LLAGNs.

Wasleske et al. (2022) examined the UV light curves of 1819 NSA galaxies and using the variability selection method, they classified 48 of them as AGNs. They checked other AGN selection methods and found that, of 48, 8 are classified as AGNs by BPT and 2 by mid-IR colors. Wasleske & Baldassare (2023) analyzed the X-ray properties of 23 AGN candidates selected based

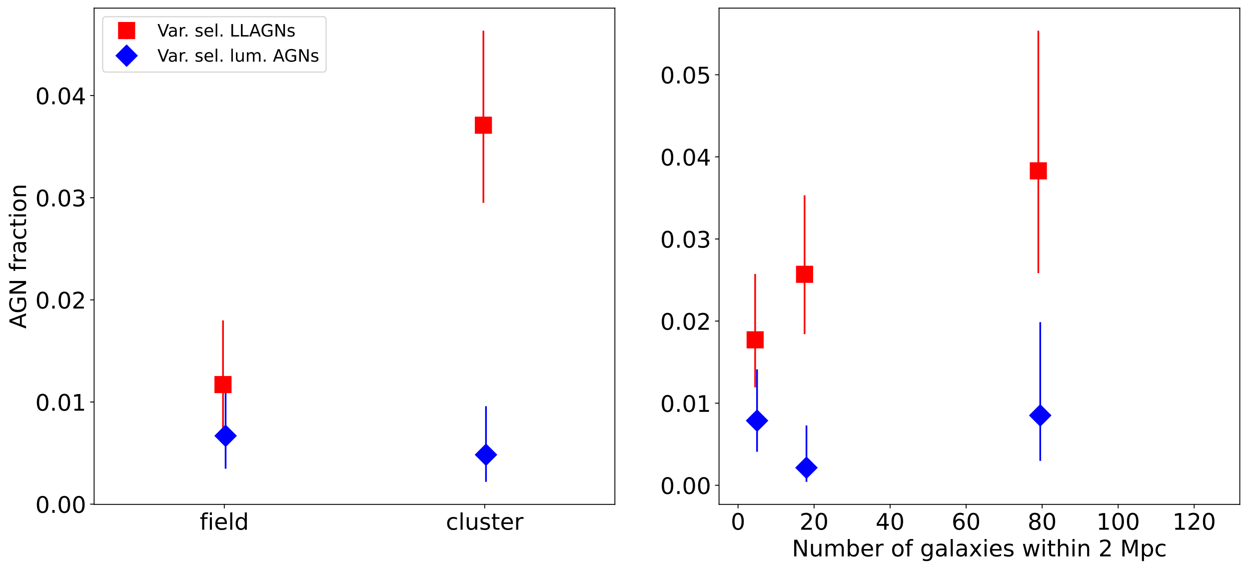

Figure 3.5: AGN fractions versus global environmental parameters of the association with WH24 galaxy clusters (left) and the number of NSA galaxies within 2 Mpc (right). The uncertainties are calculated by computing the confidence limit for binomial statistics for small number of events (Gehrels, 1986). The LLAGNs appear to be more prominent in denser environments, while luminous AGNs do not show such trend. The luminous AGN fraction may be underestimated for all bins due to the properties of the parent galaxy sample.

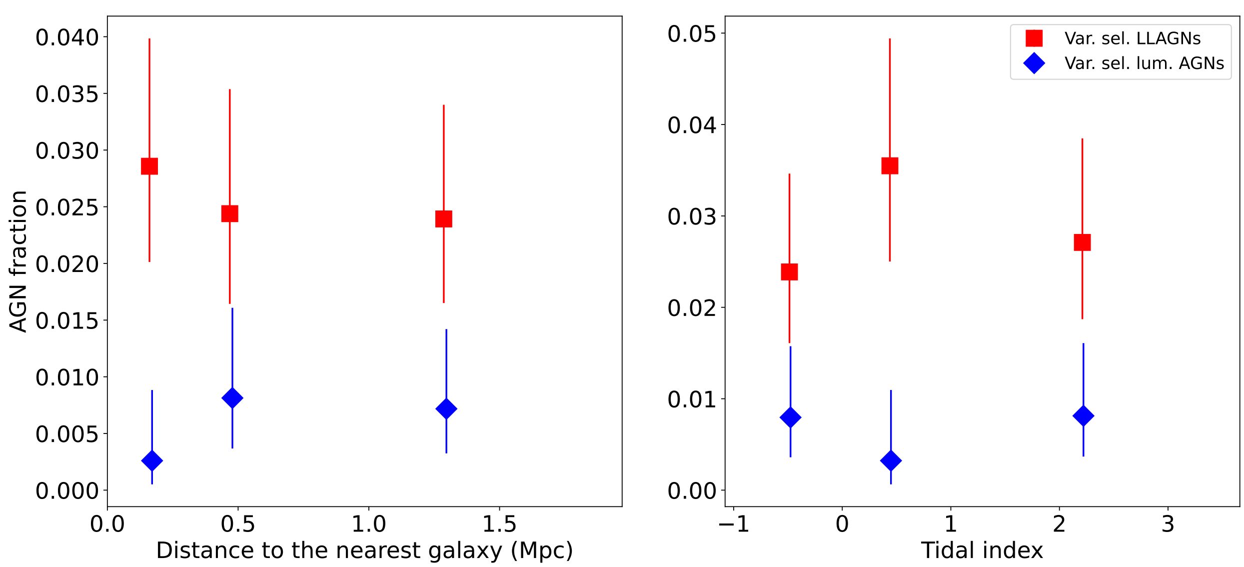

Figure 3.6: AGN fractions versus local environmental parameters of the distance to the nearest NSA galaxy (left) and the tidal index (right). The uncertainties are calculated by computing the confidence limit for binomial statistics for small number of events (Gehrels, 1986). Neither LLAGN fraction nor luminous AGN fraction displays a significant correlation with either parameter. The luminous AGN fraction may be underestimated for all bins due to the properties of the parent galaxy sample.

Table 3.2. Summary of global and local environments of variability selected AGNs

Category	All galaxies	LLAGNs	Luminous AGNs
All	1218	30	7
Near a WH24 galaxy cluster	620	23	3
$0 \leq N_{\rm 2Mpc} < 9$	508	9	4
$9 \leq N_{\rm 2Mpc} < 26$	467	12	1
$26 \leq N_{\rm 2Mpc} \leq 132$	235	9	2
$D_n < 0.33$	385	11	1
$0.33 \leq D_n < 0.61$	369	9	3
$0.61 \leq D_n \leq 1.97$	418	10	3
$-1.08 \leq \Theta < 0.12$	385	9	3
$0.12 \leq \Theta < 0.77$	310	11	1
$0.77 \leq \Theta \leq 3.66$	369	10	3

Note. — $N_{\rm 2Mpc}$ indicates the number of galaxies within 2 Mpc and D_n indicates the distance to the nearest galaxy in Mpc. For $N_{\rm 2Mpc}$, D_n, and Θ, the outer boundaries are set relative to the extrema values of AGNs to exclude the outlier galaxies.

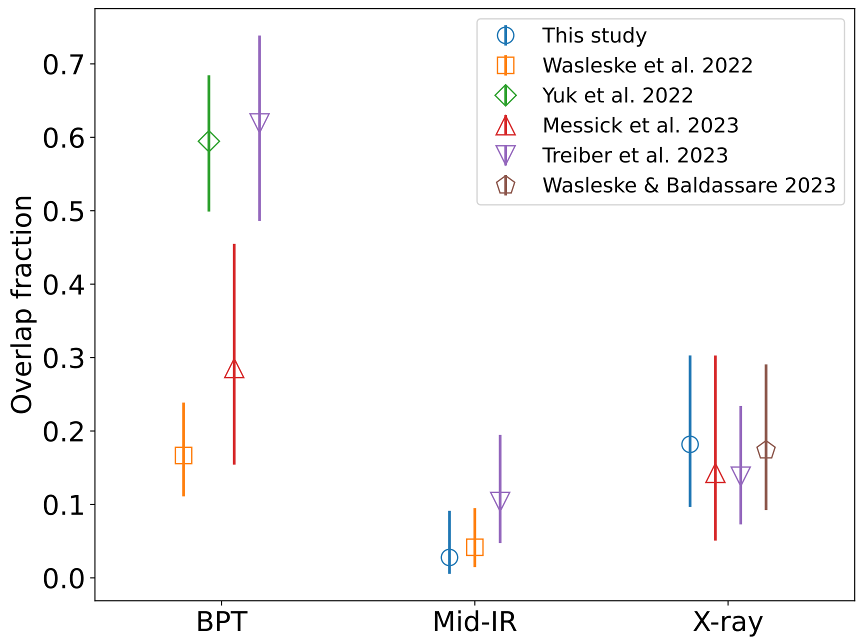

Figure 3.7: Summary of the fraction of variability selected AGNs that are classified as AGNs by other methods in the literature. The uniform standard of $L_X > 10^{42}$ erg s^{-1} is used for X-ray classifications. The uncertainties are calculated by computing the confidence limit for binomial statistics for small number of events (Gehrels, 1986). The overlap fraction between the variability selection method and other AGN selection methods ranges from a few percent with IR, 10–30% X-rays, to 20–70% optical line studies.

on UV variability. 11 of their candidates had X-ray detection from Chandra and/or XMM-Newton. They compared the X-ray luminosity (0.5–7 keV) and the expected X-ray emission from star formation to determine whether the X-ray was coming from the AGN. They classified 10 of them to be X-ray AGNs. Messick et al. (2023) performed a similar X-ray analysis on 14 nearby ($z < 0.044$) low-mass ($M_* \lesssim 5 \times 10^9 M_\odot$) variability selected AGNs. 4 of them had X-ray detections, all of which had X-ray luminosity (0.5–7 keV) greater than the anticipated emission from X-ray binaries. They also note that only 4 of their AGN candidates lie on AGN regime in the BPT diagrams. Treiber et al. (2023) made similar comparisons between the variability selection method and BPT, mid-IR, or X-ray based AGN selection methods. For their variability selected AGN sample, they analyzed Transiting Exoplanet Survey Satellite (TESS) light curves of 142,061 galaxies and identified 29 AGN candidates. They obtained optical spectra for 21 of them, and using BPT diagrams, they found 13 of them to be classified as AGNs. From mid-IR analysis, they found that 2 of their AGN candidates pass the Assef et al. (2010) criteria, 3 that pass the Stern et al. (2012) criterion. They also found that 4 of their candidates have the X-ray luminosity greater than 10^{42} erg s^{-1}. The compilation of comparisons between variability and other AGN selection methods in the literature is shown in Figure 3.7.

There exists a number of previous studies on AGNs' environmental dependence. However, it is not trivial to compare them with our results due to a number of complications. Some studies examine AGNs at low redshifts below 0.1 (e.g., Miller et al., 2003; Kauffmann et al., 2004; Gavazzi et al., 2011), while some others probe higher redshifts (e.g., Silverman et al., 2009; Martini et al., 2013). Different AGN classifications methods are used including BPT (e.g., Miller et al., 2003; Pimbblet et al., 2013; Lopes et al., 2017), [O III] luminosity (e.g., Kauffmann et al., 2004), mid-infrared color (e.g., Mishra & Dai, 2020), X-ray luminosity (e.g., Silverman et al., 2009; Haggard et al., 2010), or combination of multiple methods (e.g., Martini et al., 2013; Ellison et al., 2019). For environmental analyses, different aspects were examined, such as galaxy cluster association (e.g., Haggard et al., 2010; Mishra & Dai, 2020), local galaxy density (e.g., Miller et al., 2003; Kauffmann et al., 2004; Silverman et al., 2009; Gavazzi et al., 2011), distance from a galaxy cluster center (e.g., Pimbblet et al., 2013; Koulouridis et al., 2024), and signs of merger interactions in morphology (e.g., Ellison et al., 2019). In our best efforts to compare our results with previous studies, we selected a set of papers exploring AGN environment at redshifts $z \lesssim 1.0$ and categorize cluster or field fractions accordingly. For studies using distance from cluster center, AGN fraction nearest to the center is considered the cluster fraction, and the farthest fraction is considered the field fraction. Similarly, for studies using local galaxy density, AGN fraction in the densest environment is considered the cluster fraction, while AGN fraction with low local galaxy density are considered the field fraction. We then categorized them based on their AGN selection methods.

Previous works used for comparison are Miller et al. 2003, Kauffmann et al. 2004, Silverman et al. 2009, Haggard et al. 2010, Gavazzi et al. 2011, Pimbblet et al. 2013, Lopes et al. 2017, Koulouridis et al. 2018, Mishra & Dai 2020, and Koulouridis et al. 2024. The summary of the properties of these works are shown on Table 3.3 and the AGN fraction ratio, $f_{\rm cluster}/f_{\rm field}$, is shown on Figure 3.8. Previous studies, mostly focusing on luminous AGNs, report that the AGN fraction in the field is greater than or comparable to the AGN fraction in clusters at low redshifts. Our result of variability selected luminous AGN fractions is consistent with previous studies. However, for variability selected LLAGNs, we found that the AGN fraction is higher in clusters.

The different environmental properties of LLAGNs may suggest different triggering mechanisms. For example, Mishra & Dai (2020) speculate that fields allow more gas inflows during mergers without the ram pressure stripping effect in galaxy clusters, making field galaxies more likely to trigger AGNs at low redshifts. On the other hand, LLAGNs are thought to be more triggered by tidal disruptions and disk instabilities, which can be triggered by mergers (e.g., Hopkins & Hernquist, 2009; Hopkins et al., 2014). This is consistent with our measurements of higher LLAGN fractions in the galaxy clusters, the global overdensity factor in a relatively large region; however, when only considering the local density factors, such as the tidal index or distance to the nearest galaxy, we did not measure significantly different AGN fractions on these local density parameters. Our analysis suggests factors related to being inside global overdensity regions, e.g., velocity of galaxies before mergers and other factors, are especially important for contributing to the higher occurrence rate of LLAGNs in these regions.

Table 3.3. Summary of previous studies on AGN environments

Work	redshift	AGN selection method	Cluster vs. field	$f_{\rm cluster}/f_{\rm field}$
This work (LLAGN)	$z \lesssim 0.05$	Optical variability	cluster: $r < 2$ Mpc with $\Delta z = 0.05$ field: $r > 2$ Mpc with $\Delta z = 0.05$	$3.17^{+1.41}_{-1.82}$
This work (lum. AGN)	$z \lesssim 0.05$	Optical variability	cluster: $r < 2$ Mpc with $\Delta z = 0.05$ field: $r > 2$ Mpc with $\Delta z = 0.05$	$0.72^{+0.79}_{-0.70}$
Miller et al. (2003)*	$0.05 \leq z \leq 0.095$	BPT	cluster: $n_{75} = 0.2$ with $\Delta z = 1500$ km s^{-1} field: $n_{75} = 6.0$ with $\Delta z = 1500$ km s^{-1}	$1.03^{+0.20}_{-0.19}$
Kauffmann et al. (2004)*	$0.05 < z < 0.10$	$L_{\rm [O\,III]}$	cluster: $N_{\rm 2Mpc} > 12$ with $\Delta z = 500$ km s^{-1} field: $N_{\rm 2Mpc} < 2$ with $\Delta z = 500$ km s^{-1}	$0.45^{+0.11}_{-0.12}$
Silverman et al. (2009)	$0.1 < z < 1.0$	$L_{\rm X}$	cluster: zCOSMOS galaxy groups field: COSMOS fields	$0.79^{+0.20}_{-0.20}$
Haggard et al. (2010)	$z \leq 0.7$	$L_{\rm X}$	cluster: literature membership data field: Chandra fields	$0.74^{+0.29}_{-0.22}$
Gavazzi et al. (2011)*	$0.013 < z < 0.032$	WHAN	cluster: $-1.0 < \log(1+\delta_{1,1000}) < 0.0$ field: $1.3 < \log(1+\delta_{1,1000}) < 2.0$	$0.56^{+0.11}_{-0.10}$
Pimbblet et al. (2013)*	$0.070 < z < 0.084$	BPT	cluster: $r = 0.3r_{\rm virial}$ field: $r = 2.5r_{\rm virial}$	$0.70^{+0.27}_{-0.26}$
Lopes et al. (2017)	$z \leq 0.1$	BPT	cluster: $r < 2.50h^{-1}$ Mpc with $\Delta z = 4000$ km s^{-1} field: $r > 4$ Mpc with $\Delta z = 0.06$	$0.48^{+0.06}_{-0.06}$
Koulouridis et al. (2018)	$0.1 < z < 0.5$	$L_{\rm X}$	cluster: $r \leq 2r_{500}$ field: computed from mock clusters	$1.30^{+0.38}_{-0.30}$
Mishra & Dai (2020)	$z < 0.5$	Mid-IR color	cluster: $r < r_{500}$ with $\Delta z = 0.05z_{\rm cl}$ field: $5r_{500} < r < 10r_{500}$ with $\Delta z = 0.05z_{\rm cl}$	$0.46^{+0.08}_{-0.08}$
Koulouridis et al. (2024)	$0.16 \lesssim z \lesssim 0.26$	$L_{\rm X}$	cluster: $r = 0.5r_{500}$ field: $r = 1.5r_{500}$	$0.48^{+0.22}_{-0.19}$

Note. — WHAN refers to the equivalent width of Hα to [N II]/Hα diagnostic (Cid Fernandes et al., 2011). r, $r_{\rm virial}$, and r_{500} represent the projected distance from the cluster center, the virial radius, and the radius where the density is 500 times greater than the critical density, respectively. $z_{\rm cl}$ represents the redshift of the cluster. n_{75}, $\delta_{1,1000}$, and $N_{\rm 2Mpc}$ represent the projected surface galaxy density in units of h_{75}^2 Mpc^{-2}, number density within the radius of $1h$ Mpc^{-1} with $\Delta z = 1000$ km s^{-1}, and the number of neighboring galaxies within 2 Mpc, respectively. * indicates that the study presented a range of values and we used the extrema for our comparison. Kauffmann et al. (2004) presented a set of AGN fractions for different stellar mass ranges, so we took the mean value of the AGN fraction ratios.

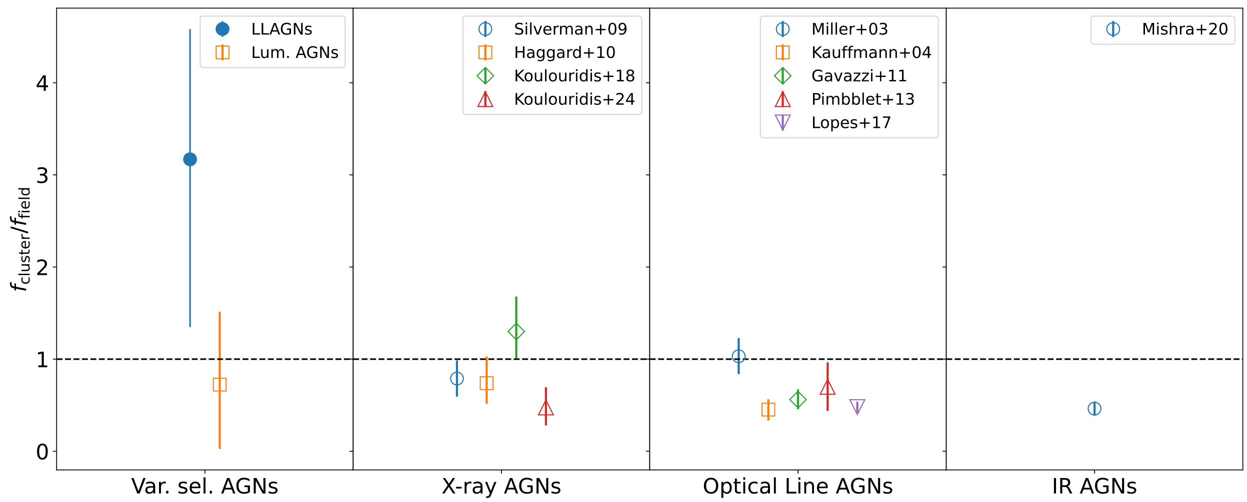

Figure 3.8: Compilation of cluster AGN fraction to field AGN fraction ratios from this work and past studies at low redshifts, classified by AGN selection methods. The dashed line represents unity. Previous studies using X-ray, optical lines, or IR AGN selection methods report that the cluster AGN fraction is in general lower than the field AGN fraction, which is consistent with our results with variability selected luminous AGNs. However, variability selected LLAGNs have much greater cluster AGN fraction than the field fraction.

Throughout this study, we used the Hα luminosity based LLAGN definition. It is possible to classify LLAGNs by different metrics, such as Eddington ratios (i.e., $\lambda < 10^{-2}$, e.g., de Menezes et al. 2020). As almost all of the variability selected AGNs we examined have low Eddington ratios, they would all be classified as LLAGNs by this standard except for 1 object (SDSS J112752.43+025038.3). Using the Eddington based definition only minimally affects the analysis results on the overlapping fractions between LLAGN selection from the variability and other methods and the environmental results. We are not able to measure the environmental effect for luminous AGN using the Eddington ratio definition.

3.7. Conclusion

We analyzed the multi-wavelength and environmental properties for a sample 1218 low-redshift bright galaxies where 37 of them are classified as variability selected AGNs by Yuk et al. (2022). We examined whether the variability selected AGNs are classified as AGNs by other AGN selection methods utilizing multi-wavelength data, including mid-infrared colors and X-ray luminosity, and if there is a correlation between AGN fraction and environment.

Out of the variability selected AGNs, 60% lie on the AGN region on BPT diagrams (Yuk et al., 2022), 3% are classified as AGNs by any of the WISE-based mid-IR color criteria, and 18% have eROSITA-DE X-ray luminosities greater than 10^{42} erg s^{-1}. These results agree with previous multi-wavelength studies on variability selected AGNs by Wasleske et al. (2022), Messick et al.

(2023), Treiber et al. (2023), and Wasleske & Baldassare (2023). The small to moderate overlap fraction between variability selection method and other AGN selection methods suggests that the variability selection method is important for discovering AGNs, especially LLAGNs, that other methods may miss.

From the environment analysis, we find that the LLAGNs are more commonly found in denser global environments, while local environments do not appear to affect AGN fractions. Previous studies on AGN abundance dependence on environments (e.g., Miller et al., 2003; Kauffmann et al., 2004; Silverman et al., 2009) suggest that the AGN fraction in field is greater than or comparable to cluster AGN fractions. The discrepancy between our results and previous studies may be due to different samples of AGNs. AGNs used in these previous studies used traditional methods, such as BPT, mid-IR color, or X-ray luminosity, to classify AGNs, are dominated by luminous AGNs, and the discrepancy can be interpreted as the difference between luminous AGNs and LLAGNs. This difference between AGN fraction's environmental dependence may be potentially due to different triggering mechanisms for LLAGNs.

As demonstrated, the sample of variability selected AGNs have different properties compared to AGNs classified by traditional methods. This means that the variability selection method is crucial for discovering a wider classes of AGNs. With many high-quality time-series surveys online and under construction, we expect many more AGNs to be discovered that were not previously classified as AGNs and they will be valuable for better understanding AGNs.

3.8. Acknowledgments

H.Y. and X.D. would like to acknowledge NASA funds 80NSSC22K0488, 80NSSC23K0379 and NSF fund AAG2307802. H.Y. also thanks the Avenir fellowship. We would also like to thank the anonymous referee and R. Mushotzky for constructive feedback.

This publication makes use of data products from the Wide-field Infrared Survey Explorer, which is a joint project of the University of California, Los Angeles, and the Jet Propulsion Laboratory/California Institute of Technology, funded by the National Aeronautics and Space Administration.

Parts of this work is based on data from eROSITA, the soft X-ray instrument aboard SRG, a joint Russian-German science mission supported by the Russian Space Agency (Roskosmos), in the interests of the Russian Academy of Sciences represented by its Space Research Institute (IKI), and the Deutsches Zentrum für Luft- und Raumfahrt (DLR). The SRG spacecraft was built by Lavochkin Association (NPOL) and its subcontractors, and is operated by NPOL with support from the Max Planck Institute for Extraterrestrial Physics (MPE). The development and construction of the eROSITA X-ray instrument was led by MPE, with contributions from the Dr. Karl Remeis Observatory Bamberg & ECAP (FAU Erlangen-Nuernberg), the University of

Hamburg Observatory, the Leibniz Institute for Astrophysics Potsdam (AIP), and the Institute for Astronomy and Astrophysics of the University of Tübingen, with the support of DLR and the Max Planck Society. The Argelander Institute for Astronomy of the University of Bonn and the Ludwig Maximilians Universität Munich also participated in the science preparation for eROSITA.

CHAPTER 4

High-frequency Breaks in the Optical Active Galactic Nucleus Power Spectral Density

This chapter is the reproduction of Yuk & Dai (2025), A&A, 698, A105.

4.1. Abstract

Context. Variability is a ubiquitous feature of active galactic nuclei (AGNs), and the characterisation of this variability is crucial to constraining its physical mechanism and proper applications in AGN studies. The advent of all-sky and high-cadence optical surveys allows more accurate measurements of AGN variability down to short timescales as well as direct comparisons with X-ray variability from the same sample of sources.

Aims. We aim to analyse the optical power spectral density (PSD) of AGNs with measured X-ray PSDs.

Methods. We used light curves from the All-Sky Automated Survey for SuperNovae (ASAS-SN) and the Transiting Exoplanet Survey Satellite (TESS) and used the Lomb-Scargle periodogram to obtain PSDs. The joint optical PSD is measured over up to six orders of magnitude in frequency space on timescales of minutes to a decade. We fitted either a damped random walk (DRW) or a broken power law (BPL) model to constrain the PSD model and break frequency.

Results. We find a set of break frequencies ($\lesssim 10^{-2}$ day^{-1}) from DRW and BPL fits that generally confirm previously reported correlations between break frequencies and the black hole mass. In addition, we find a second set of break frequencies at higher frequencies ($> 10^{-2}$ day^{-1}). We observe a potential weak correlation between the high-frequency breaks with the X-ray break frequencies and the black hole mass. We further explored the dependence of the correlations on other AGN parameters, finding that adding X-ray, optical, or bolometric luminosity as the third correlation parameter can substantially improve the correlation significances. The newly identified high-frequency optical breaks can constrain different aspects of the physics of AGNs.

4.2. Introduction

Variability is a ubiquitous characteristic of active galactic nuclei (AGNs), and is observed at all wavelengths (e.g. Mushotzky et al. 1993; Vanden Berk et al. 2004) and on all timescales (e.g. Grandi et al. 1992; Markowitz et al. 2003). The mechanism driving the variability is still debated. A number of theories have been suggested, such as accretion disc instabilities (e.g. Kawaguchi et al. 1998;

Trèvese & Vagnetti 2002), global inhomogeneities from infall or thermal processes (e.g. Lightman & Eardley 1974; Shakura & Sunyaev 1976; Kelly et al. 2009), local disc communication processes on sound crossing or Alfvén timescales (Dexter & Agol, 2011), magnetorotational instabilities (e.g. Balbus & Hawley 1991; Reynolds & Miller 2009), and reprocessing between the disc and the corona on light crossing timescales (e.g. Haardt & Maraschi 1991; McHardy et al. 2018).

Though its origin is uncertain, AGN variability provides clues about the physical properties of the central engine. The variability at different wavelengths is known to arise from different regions of the AGN, and the variability time lags in different wavelengths can be used for reverberation mapping to measure the physical size of the AGN structure and the mass of the central supermassive black hole (SMBH; e.g. Wandel et al. 1999; Kaspi et al. 2000; Peterson et al. 2005). Different classes of AGNs also show different variability features (e.g. Ptak et al. 1998), and by studying these differences, we can learn specific details about each class. As a behaviour common to all AGNs, variability can also be used to find AGNs (e.g. Butler & Bloom 2011; MacLeod et al. 2011; Ruan et al. 2012; Treiber et al. 2022; Yuk et al. 2022).

The stochastic variability of AGNs can be characterised by its power spectral density (PSD). PSDs are characterised by red noise, where the power increases for lower frequencies and then saturates below some frequency (e.g. Uttley et al. 2002). For optical variability this is commonly modelled as a damped random walk (DRW; e.g. Kelly et al. 2009; Kozłowski 2016). In these models, the DRW break frequency, the frequency where the PSD starts to flatten, is correlated with the mass of the SMBH powering the AGN (e.g. Kelly et al. 2009; MacLeod et al. 2010; Burke et al. 2021). With the recent advent of high-cadence optical data, we can now probe the optical PSD on short timescales (e.g. Smith et al. 2018), where steeper power law slopes than -2, the slope from the DRW model, were inferred (Mushotzky et al., 2011).

The X-ray variability of AGNs has been observed down to very short timescales (< 1 day; e.g. Grandi et al. 1992; Uttley et al. 2002), and many PSD and break frequency studies have been conducted (e.g. Uttley et al. 2002; McHardy et al. 2004; González-Martín & Vaughan 2012; González-Martín 2018; Smith et al. 2018). However, previous studies were limited by the differences in optical and X-ray timing surveys, and direct comparisons betweens optical and X-ray PSDs for the same set of sources were difficult. For this study, we combined the long-term, low-cadence, ground-based data from the All-Sky Automated Survey for SuperNovae (ASAS-SN; Shappee et al. 2014a; Kochanek et al. 2017) and the short-term, high-cadence, space-based data from the Transiting Exoplanet Survey Satellite (TESS; Ricker et al. 2015). We constructed a PSD separately for each dataset and then merged them to identify the break frequencies. This allowed the first systematic comparison of optical and X-ray break frequencies in the power spectra of AGNs. For this comparison, we used the sample of AGNs with X-ray break frequencies measured by González-Martín (2018). We introduce the sample, the ASAS-SN and TESS data, and the data analysis procedure in Section 4.3. We describe the methods for extracting and fitting the PSDs in Section 4.4. In Section 4.5, we present the resulting break frequencies and examine how they relate to previous results. We discuss the implications in Section 4.6.

4.3. Data

4.3.1. Data Properties and the Sample

ASAS-SN (Shappee et al. 2014a; Kochanek et al. 2017) began surveying the sky in 2012. After several expansions, it now consists of 20 14-cm telescopes distributed over five 'units' and can cover the visible sky nightly in good conditions. The two original units initially used the V-band filter. The three new units commissioned in 2017 use g-band filters and the original two units switched to the g band in 2018. During the transition, there were approximately 400 days when both the V band and the g band were used. ASAS-SN images have limiting magnitudes of $V \sim 16.5 - 17.5$ and $g \sim 17.5 - 18.5$ depending on lunation, a field of view of 4.5 deg^2, a pixel scale of $8\farcs0$, and a typical full width half maximum (FWHM) of ~ 2 pixels.

Launched in 2018, TESS (Ricker et al. 2015) is equipped with four cameras and its TESS bandpass spans a wavelength range of 600 to 1000 nm. Each camera has a field of view of 24° by 24°. The combined 24° by 96° field of view is called a sector. TESS observes each sector for approximately 27.4 days. For the primary mission, the 26 sectors observed until July 2020, the full-frame images (FFIs) were taken with a 30-minute cadence. The first extended mission, which lasted until sector 55 in September 2022, collected FFIs with a 10-minute cadence. In the current, second extended mission, the FFIs are taken with a 200-second cadence. Each sector is divided into two cycles, each lasting for approximately 13 days, with ∼1 day gap in between for data transmission. The FFIs have the pixel scale of $21\farcs0$ with a typical FWHM of ~ 2 pixels. The FFIs used for this study can be found in Mikulski Archive for Space Telescopes (MAST[1]).

González-Martín (2018) provided the most recent compilation of AGNs with measured X-ray breaks in their power spectra. This sample includes 22 AGNs, with their black hole masses, $\log(M_{\rm BH}/M_\odot)$, ranging from 5.4 to 8.5. Majority of the black hole masses are measured by reverberation mapping, while others are measured by different methods including $M - \sigma$ relation, 5100Å continuum luminosity, water masers, and radio fundamental plane. Their bolometric luminosities, $\log(L_{\rm bol}/\text{erg s}^{-1})$, range from 41 to 46. These AGNs are nearby, with their redshifts ranging from 0.001 to 0.05, with the exception of PKS 0558-504 with a redshift of 0.14. These AGNs all have *XMM-Newton* observations with 88–1095 ks exposure times. González-Martín (2018) binned the 2–10 keV data into 50-second bins (with a few exceptions using 100- and 200-second bins), and produced light curve segments of 10, 20, 40, 60, 80, and 100 ks. The PSD of each light curve was modelled with a broken power law (BPL) to measure the break frequency. Each

[1]http://dx.doi.org/10.17909/0cp4-2j79

light curve segment for a target was fit separately, leading to a range of break frequency estimates. We compared the optical and X-ray properties of the power spectra of this sample in this paper. Five of these targets (MRK 335, IC 4329A, NGC 5506, ARK 564, and NGC 7469) were not observed by TESS by the end of the first extended mission. For these objects, we used only the ASAS-SN light curves.

4.3.2. Data Reduction

To extract the ASAS-SN light curves, we used image subtraction (Alard & Lupton, 1998; Alard, 2000) and aperture photometry (see Jayasinghe et al., 2018 for more details). For calibration, we used the AAVSO Photometric All-Sky Survey (APASS) catalogue (Henden et al., 2015). We corrected the zero-point offsets between different cameras and recalculated the photometric errors as described in Jayasinghe et al. (2018) and Jayasinghe et al. (2019), respectively.

We used a similar method to extract the TESS light curves, with the modifications described in Fausnaugh et al. (2021) and Vallely et al. (2021). We first cut out 750-pixel postage stamps around the target from the FFIs. Then we created a reference image using 100 high-quality images that have no mission-provided data quality flags and have point spread function widths and background levels lower than the median values for the sector. We then scaled and subtracted the reference image from all the individual images. We used a median filtering method to minimise the effects of background structures (the 'straps' and complex internal reflection artefacts) and then performed point spread function photometry on the subtracted images. We used the subtraction method over aperture photometry because TESS's large pixel size makes source blending a significant challenge to aperture photometry, while the subtraction method simply measures the flux changes relative to the reference image (Vallely et al., 2021).

Once the initial TESS light curve is extracted, a few additional adjustments are made. To check for any anomalies, we also extracted light curves for a grid of nearby pixels as shown in Figure 4.1. At the beginning of each cycle of a TESS Sector, there is often a spike in the backgrounds lasting for a few days. For some objects, this greatly affects the photometry. For example, Figure 4.1 shows that all the nearby pixels display the same pattern at the beginning of each cycle. The affected segments tend to have greater flux uncertainty, so we computed the median and standard deviation of the flux uncertainty, and took out the portion with uncertainties that deviate significantly from the median. The observations for a sector are interrupted at the middle for data transmission. Sometimes, there is an offset between these two sub-sections (also seen in Figure 4.1), which we also corrected.

Some sources have anomalous TESS light curves and were discarded. For example, the TESS light curves of 1H 0707−495 (Figure 4.2) display a periodic behaviour where the flux drops regularly. However, this pattern is observed in most of the nearby pixels, and it is due to contamination from

Table 4.1. TESS sectors used for the sample

Name	TESS sectors
MRK 335	...
ESO 113-G010	1, 2, 28, 29
Fairall 9	2, 28, 29
PKS 0558-504	1*, 5, 6, 7, 11*, 32, 33, 34
1H 0707-495	6*, 7*, 8*, 32*, 33*, 34*
ESO 434-G040	9, 35
NGC 3227	45, 46, 48
RE J1034+396	21, 48
NGC 3516	14, 20, 21, 41, 47, 48
NGC 3783	10, 36, 37
NGC 4051	22, 49
NGC 4151	49
MRK 766	22
NGC 4395	22, 49
MCG-06-30-15	11*, 37
IC 4329A	...
Circinus	11*, 12*, 38
NGC 5506	...
NGC 5548	23, 50
NGC 6860	13, 27
ARK 564	...
NGC 7469	...

Note. — * Discarded data.

a nearby eclipsing binary. All six TESS sectors are affected by the binary, so we rejected all the TESS light curves of this target for analysis. We confirmed that there are no other similar cases by checking the ASAS-SN variable stars database (Shappee et al. 2014a; Jayasinghe et al. 2018) for variable stars near each target. Similarly, when we observed unusual features in a TESS light curve, we looked at the light curves of nearby pixels to determine if the feature is likely to be real or that the sector should be rejected. Table 4.1 lists the TESS sectors used for each target and labels which ones are discarded.

The ASAS-SN light curves are measured in millijanskys or magnitudes, while the TESS light curves are measured in units of counts relative to the reference frame. Before we extracted the power spectra, we converted the TESS light curves into millijanskys, using the TESS calibration

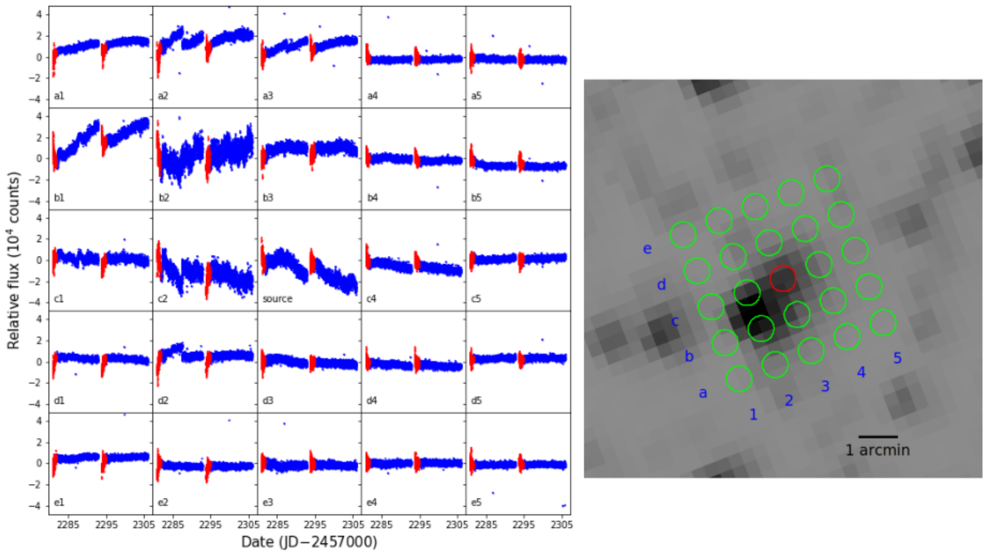

Figure 4.1: Left: TESS sector 36 light curve of NGC 3783 and nearby pixels. The centre panel labelled ‘source’ is the light curve of the target and the other 24 panels are the light curves of nearby pixels. The red points are the data points with uncertainties greater than the standard deviation of uncertainties from the median of each light curve. Right: TESS image and the locations of NGC 3783 (red circle) and the nearby pixels (green circles) where the light curves on the left were extracted.

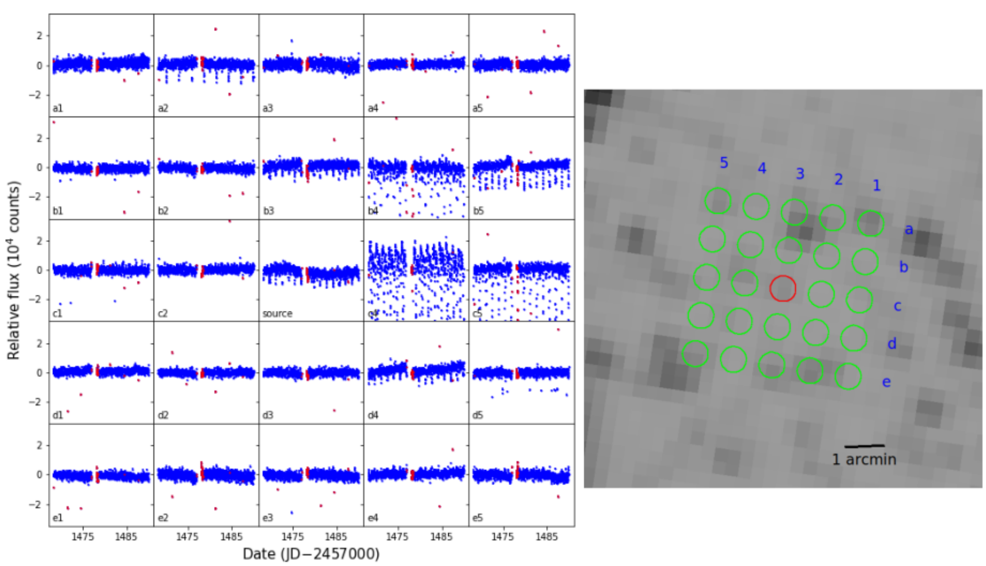

Figure 4.2: Same as Figure 4.1 for the TESS sector 6 light curve of 1H 0707-495. The source light curve shows periodic variability due to a nearby eclipsing binary, so this TESS light curve was discarded.

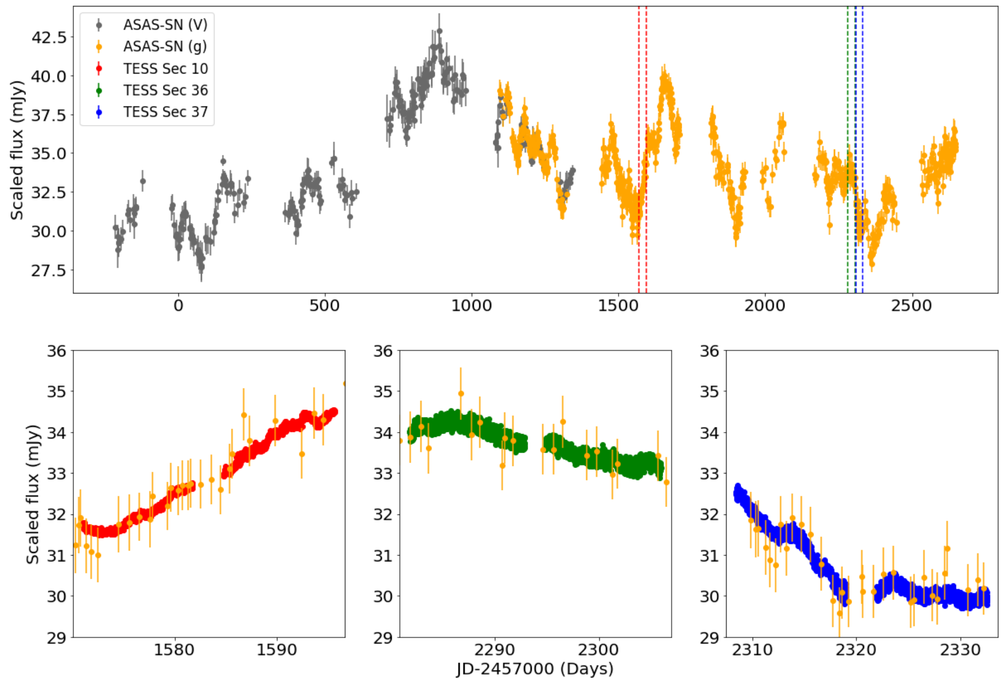

Figure 4.3: Top: ASAS-SN light curves of NGC 3783 with the TESS sectors marked. Bottom: TESS light curves along with ASAS-SN data. The light curves are scaled to overlap.

that one count $= 20.44 \pm 0.05$ mag with a zero point of 2631.9 Jy (Vanderspek et al., 2018).

A representative compilation of light curves (NGC 3783) is shown in Figure 4.3. It shows that the TESS and ASAS-SN light curves have similar trends with offsets due to the filter differences. The light curves for Circinus are shown in Figure 4.4. For sectors 11 and 12, a sinusoidal pattern was found in the nearby pixels affecting the target's light curve, while that pattern is not seen in sector 38. We discarded sectors 11 and 12 and used only sector 38 for the PSD analysis.

4.4. Methods

4.4.1. Power Spectra

In general, there are two approaches to constraining PSDs from the light curves: one is the backward method of transforming the light curves into frequency domain and the other is the forward method of assuming a parametric model to fit the light curves. Most previous studies of optical PSDs of AGNs were using the forward method because of the sparse sampling of the light curves (e.g. Kelly et al. 2009; Kozłowski et al. 2010; MacLeod et al. 2010; Zu et al. 2013); however, with the high cadence optical survey, the more intuitive backward method were used in more analyses (e.g. Mushotzky et al. 2011; Burke et al. 2020; Petrecca et al. 2024). Since the forward method can only apply to parametrised PSD models, mostly the DRW model in optical studies, it is beneficial to use the backward methods to infer the general characteristics of the PSD

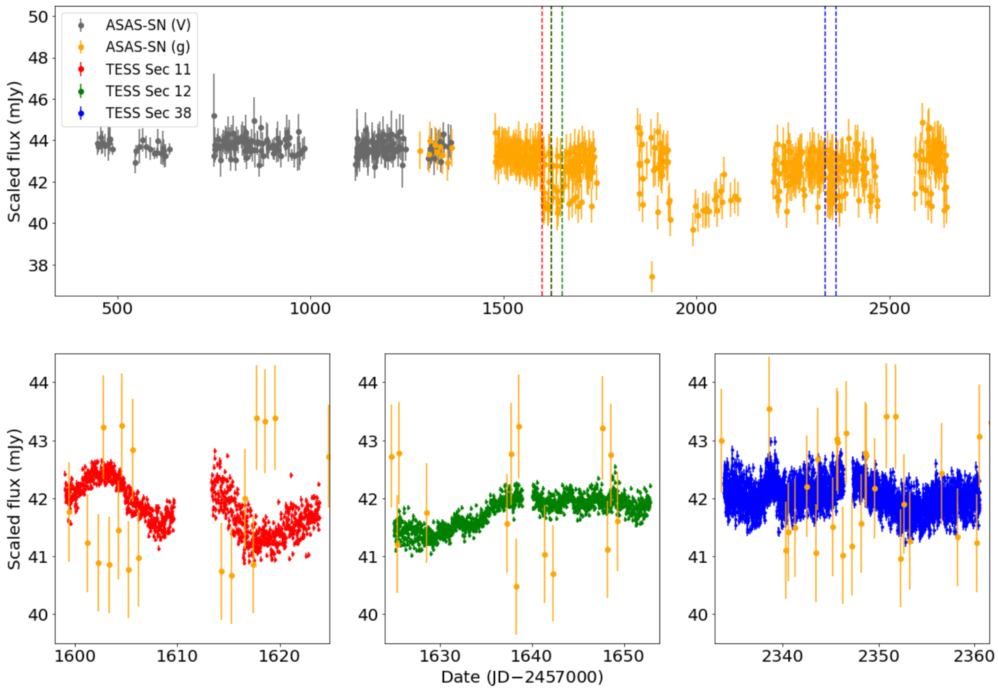

Figure 4.4: Same as Figure 4.3 for Circinus with TESS sectors 11, 12, and 38.

with the inclusion of the new high-frequency TESS data in this paper, which potentially can reveal new PSD features that are absent in commonly assumed optical PSD models. In addition, most previous forward modelling analyses were applied to one dataset, and the computation time and calibration effort will increase significantly when dealing with multiple datasets as in this study. Here, we used a backward Lomb-Scargle periodogram (Lomb 1976; Scargle 1982) to construct the power spectra with simulations to constrain its biases imposed in the PSD break measurement. A forward-fitting analysis will be presented in a separate paper.

The lower frequency limit is set at $1/T$, where $T = t_N - t_1$ is the time span of the observations, and the upper limit is set at $1/(2\Delta T_{\text{samp}})$, where ΔT_{samp} is the typical sampling interval (1 day for ASAS-SN, 30 minutes for TESS sectors $\leq$26, 10 minutes for TESS sectors >26). The raw periodograms from the different datasets do not line up perfectly, so we applied several corrections. First, we applied the rms normalisation $2\Delta T_{\text{samp}}/(\bar{x}^2 N)$ (e.g. Vaughan et al. 2003), where $\bar{x}$ is the mean flux. Such rms normalisations will also minimise the biases due to the filter differences of the different datasets, assuming that the wavelength-dependent AGN variability mainly manifests in the rms amplitudes (e.g. MacLeod et al. 2010). We next separately normalised the PSDs between the ASAS-SN V- and g-band PSDs, and between the multiple TESS sectors' PSDs. There can be additional offsets between ASAS-SN and TESS PSD measurements such as differences in the rms variability between wavelengths. It is challenging to normalise the ASAS-SN and TESS PSDs because the ASAS-SN PSDs are dominated by noise in the overlapping region. So we preliminarily

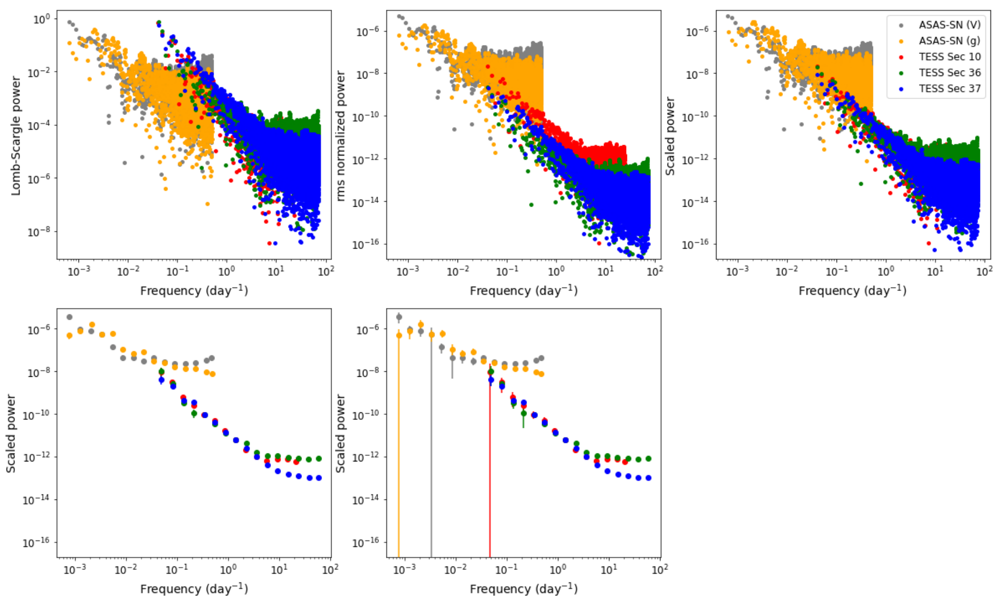

Figure 4.5: Steps to produce the PSDs used in the model fits. Top: Original Lomb-Scargle periodogram of NGC 3783 (left), with rms normalisation (middle), and after additional scaling to line up the PSDs (right). Bottom: Binned periodogram with the standard deviation of the mean as the uncertainty (left), and with the additional estimated systematic uncertainties (middle).

normalised the TESS and ASAS-SN components by lining up the PSDs at $< 10^{-2}$ day^{-1}. Then, for the fitting process, we included the normalisation factor for each PSD as free parameters.

Before fitting, the periodogram is binned and averaged linearly into logarithmic frequency bins with a width of a factor of 1.6 (0.2 dex) in frequency. The uncertainties are the standard deviations about the mean. To estimate any additional systematic error contribution, we fitted a simple power law plus white noise model, $P(\nu) = A\nu^{-\alpha} + C$, calculated the reduced χ^2 statistic, $\chi^2_{\rm red}$, and then scaled the uncertainties to make $\chi^2_{\rm red}$ unity. On average, $\chi^2_{\rm red}$ before accounting for systematic uncertainties is about 5 for the TESS data, 25 for the V-band ASAS-SN data, and 10 for the g-band ASAS-SN data. Figure 4.5 shows an example of the periodograms before and after the scaling, binning, and the addition of the estimated systematic uncertainties.

4.4.2. Fitting

We fitted two models to the periodogram, the BPL and DRW models. The main difference between the two models is that the low-frequency and high-frequency power indices are not fixed at 0 and -2, respectively, in the BPL model. We fitted all models by minimising a χ^2 statistic. We first fitted a BPL plus white noise model. Compared to the DRW model, this model has several additional parameters, so we approached the fit in several steps. First, we fitted the simple power law with white noise model, $P(\nu) = A\nu^{-\alpha} + C$ to the individual datasets. Using those fit parameters as initial guesses, the combined periodograms were fit with the smoothly BPL plus white noise power spectrum,

$$P(\nu) = A_i \left(\frac{\nu}{\nu_{\text{br}}}\right)^{-\alpha_1} \left\{\frac{1}{2}\left[1 + \left(\frac{\nu}{\nu_{\text{br}}}\right)^{1/\Delta}\right]\right\}^{(\alpha_1-\alpha_2)\Delta} + C_i, \tag{4.1}$$

where ν_{br} is the break frequency, A_i is the amplitude at ν_{br}, α_1 and α_2 are the low and high-frequency slopes, respectively, Δ is the smoothness parameter, where the larger values of Δ mean smoother break, and C_i is the noise level for light curve i (Astropy Collaboration et al., 2022). The parameters ν_{br}, α_1 α_2, and Δ are the same for all PSDs, while the amplitude A_i and noise C_i are different for each dataset. The adjustments in the amplitudes allow us to account for any remaining normalisation differences between different PSD measurements. We first made fits with Δ fixed at 0.1, 0.2, 0.3, 0.4, and 0.5 and all other parameters free. We found that $\Delta = 0.1$ resulted in the smallest χ^2, so we fixed $\Delta = 0.1$ for all subsequent fits. Next, we tested the dependence of χ^2 on two model parameters: the TESS-to-ASAS-SN scaling factor and ν_{br}. Though we adjusted the A_i individually, tests showed that the results are very sensitive to the initial conditions. So, we fitted the data on a fixed two-dimensional grid of scaling factor and ν_{br}. The scaling factor that yields the overall lowest χ^2 was chosen and the ν_{br} at the χ^2 minimum is used as the initial guess for the model, with a $\pm 10\%$ prior constraint on the frequency. Because there are still many parameters to fit, we used the shared value of the amplitude. There are two χ^2 minima in some cases, as shown by the example in Figure 4.6. For these, we separately tried fits at both minima. After this fit, the constant terms C_i were constrained to be within $\pm 10\%$ of the values from the previous fit and the amplitudes A_i were allowed to vary independently. For the final fit, we constrained the amplitudes A_i and noise terms C_i to be within 10% of the prior trial fit values and allowed the power law indices to be free parameters.

We also fitted the DRW model, also known as the continuous-time first-order autoregressive (CAR(1)) process (e.g. Kelly et al. 2009), plus white noise. The DRW model has the power spectrum

$$P(\nu) = \frac{2\sigma^2\tau^2}{1 + (2\pi\tau\nu)^2}, \tag{4.2}$$

where σ is the characteristic timescale and τ is the relaxation time. The relaxation time τ defines the break frequency of $\nu_{\text{br}} = 1/2\pi\tau$. Since most previous optical PSD studies did not use light curves with a high cadence of TESS, we fitted the DRW model to both the separate and combined ASAS-SN and TESS PSDs. In general, the DRW fits yield break frequencies in the ASAS-SN frequency regime, which is consistent with previous studies. An example of the combined PSDs with the fits and the corresponding χ^2 are shown in Figure 4.7 and 4.8.

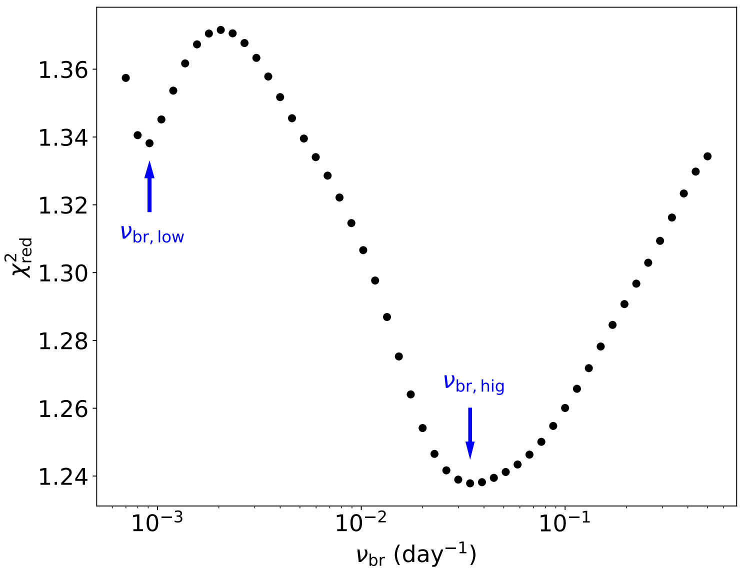

Figure 4.6: Reduced chi-squared for the BPL model fitting as a function of the break frequencies for MRK 766. The positions we identify as the two break frequencies are labelled.

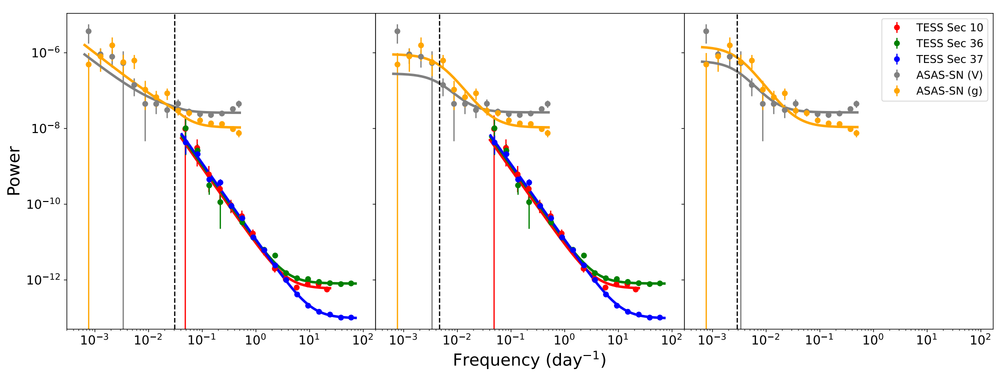

Figure 4.7: Binned periodogram of NGC 3783 fit with a BPL with the high-frequency break (left), a DRW using both TESS and ASAS-SN data (middle), and using only the ASAS-SN (right), The vertical dashed lines mark the break frequencies.

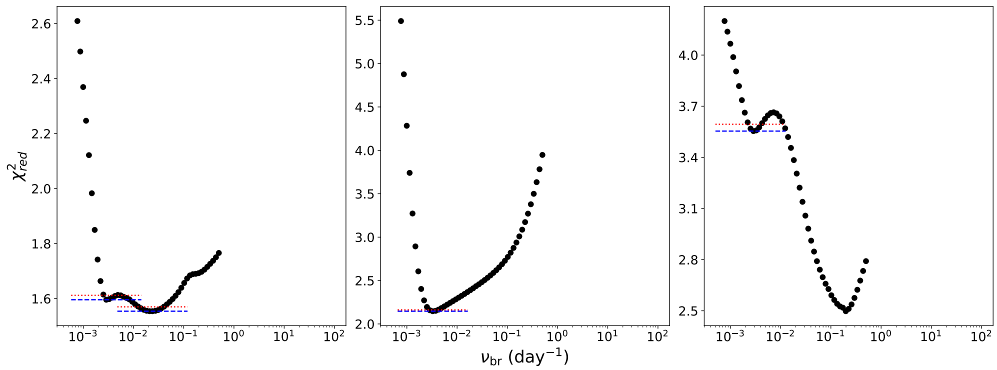

Figure 4.8: Reduced chi-squared as a function of break frequency for the three fits shown in Figure 4.7. There are two minima for the DRW fit to the ASAS-SN PSDs, but the minimum at the higher frequency is in the noise-dominated region, so the low-frequency break is used. The dashed blue lines indicate the local minima and the dotted red lines indicate the 1-sigma confidence level.

4.4.3. Comparison between Long-term ASAS-SN and TESS Light Curves and PSDs

Since most of the high-frequency breaks lie in the overlapping frequency range of the TESS and ASAS-SN PSDs, it is important to compare TESS and ASAS-SN light curves and PSDs on these timescales for potential calibration issues or variability characteristic differences between filters. Typical TESS Sectors are too short for this purpose. However, TESS observes the ecliptic poles continuously for 13 sectors, so it is possible to extract long-term, nearly continuous TESS light curves for objects near the poles. For this analysis, we used PG 1613+658, a Seyfert I galaxy near the north ecliptic pole observed over Sectors 14 to 26 during the primary mission. The combined light curve is shown in Figure 4.9.

We constructed the PSD for the combined TESS light curve using the same procedures to examine if the low-frequency regime of the combined TESS PSDs is consistent with those measured by ASAS-SN, up to a normalisation difference. To do so, we estimated and subtracted the white noise of each PSD. We compared the PSDs of the continuous TESS light curve, the PSDs of ASAS-SN V-band and g-band light curves, and the average of the 13 PSDs for the individual TESS sectors in Figure 4.10, finding that the TESS and ASAS-SN PSDs are consistent in the overlapping regions and have similar slopes at low frequencies. We did not use the PSD from all 13 sectors because it has strong artificial peaks at $14n$ ($n = 1, 2, 3, ...$) days created by the observing cadence that strongly affects the fits to the PSD. The results for the BPL PSD fits are shown in Figure 4.11. Break frequencies measured are $\log(\nu_{\text{br,hig}}/\text{day}^{-1}) = -1.09 \pm 0.03$ and $\log(\nu_{\text{br,low}}/\text{day}^{-1}) = -2.97 \pm 0.01$, which are within the typical range of break frequencies of the AGN sample.

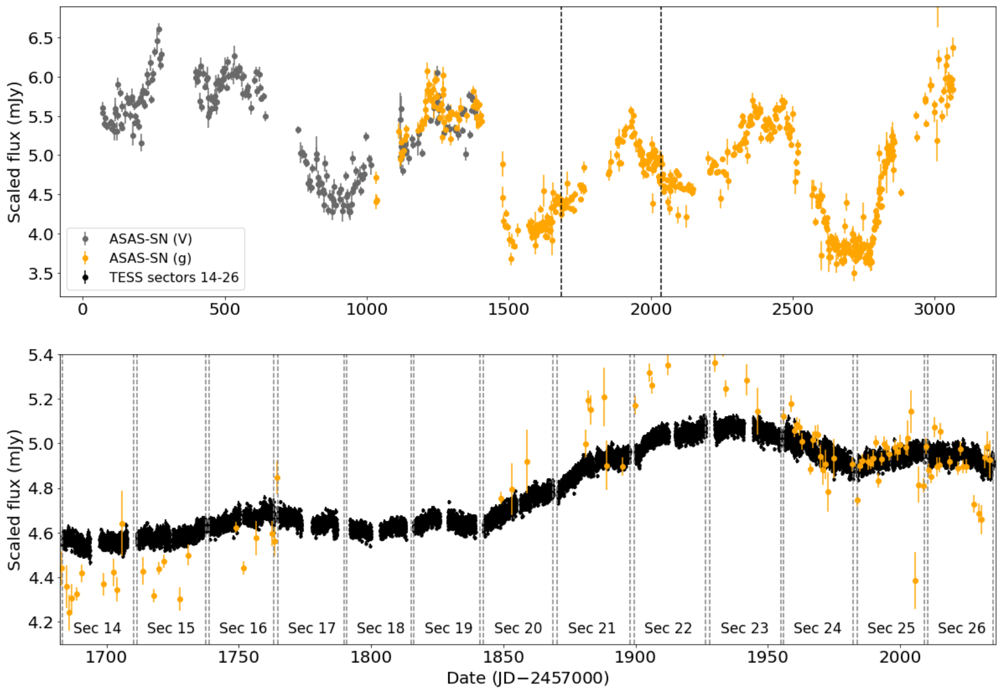

Figure 4.9: Top: ASAS-SN light curve of PG 1613+658 with the observation window of PG 1613+658 during the TESS primary mission marked. Bottom: TESS primary mission light curve of PG 1613+658 along with the ASAS-SN g-band data. The vertical dashed lines are the sector boundaries.

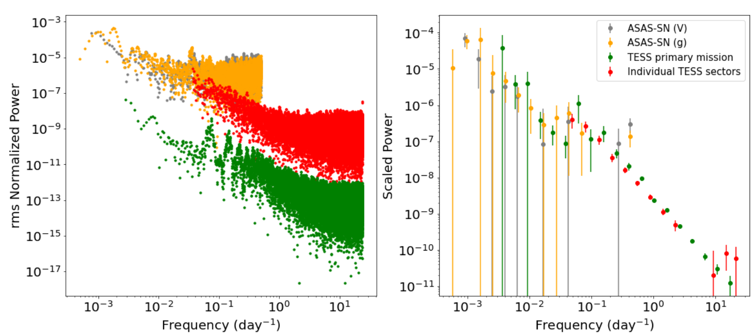

Figure 4.10: Left: rms-normalised PSDs of PG 1613+658. The PSD in green was constructed using the continuous 13 sector TESS light curve, while the red is the collection of the individual sector PSDs. Right: Binned PSDs with the white noise level subtracted and scaled to line up. The individual TESS sector PSDs were averaged before being binned.

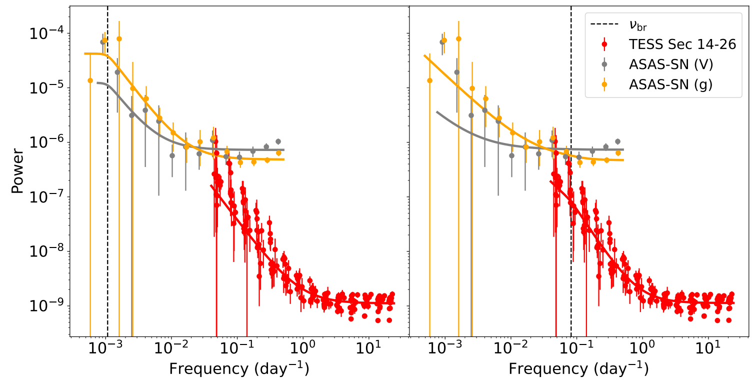

Figure 4.11: PSDs with the BPL fit of PG 1613+658. The PSDs in red labelled TESS sectors 14-26 are the PSDs of the individual sectors.

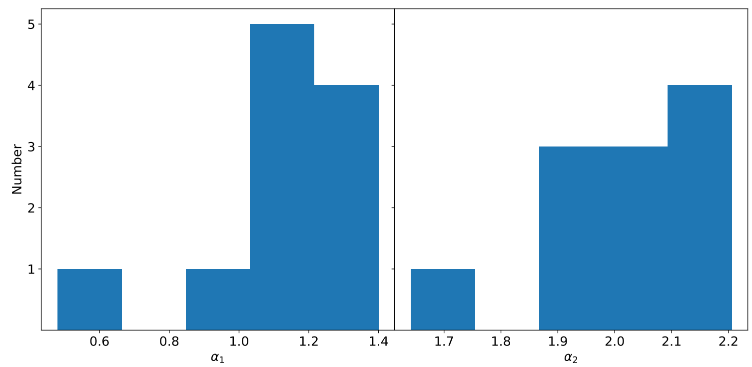

Figure 4.12: Distribution of the low-frequency (left, α_1) and high-frequency (right, α_2) slopes for the BPL fits using $\nu_{\mathrm{br,hig}}$.

4.5. Results

From the BPL fits, we find two sets of break frequencies, low- and high-frequency breaks with the dividing line at around 10^{-2} day^{-1}. The low-frequency breaks $\nu_{\mathrm{br,low}}$ are measured in objects with only ASAS-SN data, joint fits with TESS and ASAS-SN with a single χ^2_{red} minimum below 10^{-2} day^{-1}, as well as the low-frequency χ^2_{red} minimum for joint fits with two χ^2_{red} minima. These break frequencies and their associated slopes are similar to those from the DRW fits, meaning that the break frequencies are close to DRW break frequencies and power law indices are about $\alpha_1 = 0$ and $\alpha_2 = 2$. The high-frequency breaks $\nu_{\mathrm{br,hig}}$, meaning a χ^2_{red} minimum at frequencies higher than 10^{-2} day^{-1}, are prominent in most targets with both ASAS-SN and TESS data. These $\nu_{\mathrm{br,hig}}$ are typically in the overlapping region of the ASAS-SN and TESS power spectra. For ASAS-SN, the PSDs at these frequencies are dominated by white noise. For the fits yielding $\nu_{\mathrm{br,hig}}$, the power law indices for the low and high frequencies deviate from 0 and 2, especially the low-frequency slopes α_1 (Figure 4.12).

We have two estimates of the low-frequency break from the DRW models (PSD models for

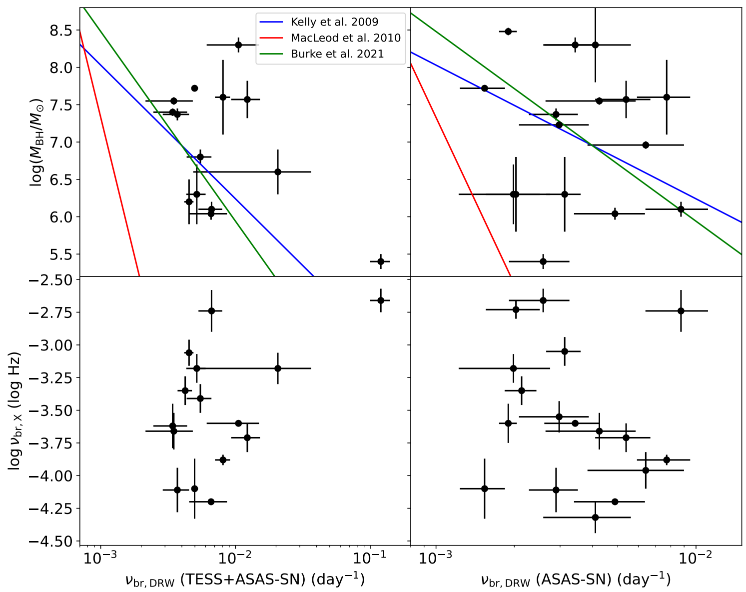

Figure 4.13: $\nu_{\rm br,X}$ and $M_{\rm BH}$ versus $\nu_{\rm br} = 1/(2\pi\tau)$ from the DRW model fit on TESS and ASAS-SN PSDs (left), and on ASAS-SN PSDs only (right).

either the ASAS-SN or the ASAS-SN plus TESS data), and a set of low and high-frequency breaks from the BPL fits to the ASAS-SN plus TESS PSDs. All breaks related to the DRW models are in the low-frequency regime. We compare these breaks with the X-ray break frequencies and black hole masses from González-Martín (2018) in Figures 4.13, 4.14, and 4.15. We used the average and uncertainties of X-ray break frequencies presented by González-Martín (2018) Figure 3. To test the relationship between the optical break frequencies and black hole mass and X-ray break frequencies, we computed Pearson's correlation coefficient (Table 4.2). We discuss the low and high-frequency regimes separately.

Table 4.2. Pearson correlation coefficients between break frequencies and previously measured parameters.

$\nu_{\rm br}$ from	$M_{\rm BH}$		$\nu_{\rm br,X}$	
	r	p	r	p
BPL fit with $\nu_{\rm br,low}$	-0.39	0.15	0.50	0.06
BPL fit with $\nu_{\rm br,hig}$	-0.56	0.06	0.57	0.04
BPL fit with corrected $\nu_{\rm br,hig}$	-0.67	0.02	0.65	0.02
DRW fit with all data	-0.43	0.13	0.48	0.07
DRW fit with ASAS-SN data	-0.06	0.82	-0.16	0.55

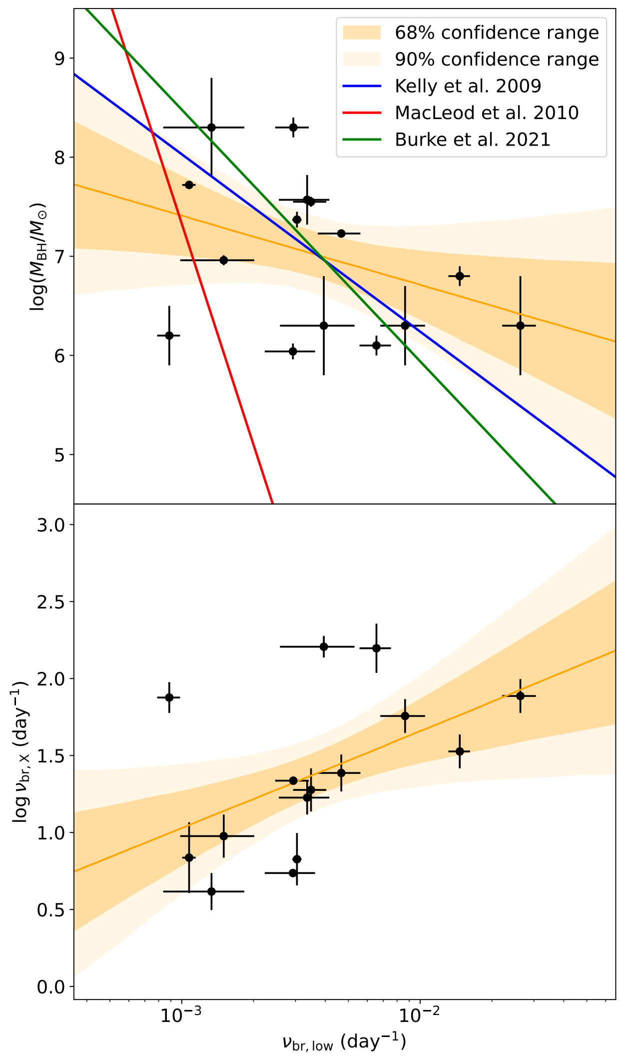

Figure 4.14: X-ray break frequency $\nu_{\text{br,X}}$ and M_{BH} versus low optical break frequency $\nu_{\text{br,low}}$ with the best linear fit and its uncertainties. The upper panel shows similar fits from Kelly et al. (2009), MacLeod et al. (2010), and Burke et al. (2021).

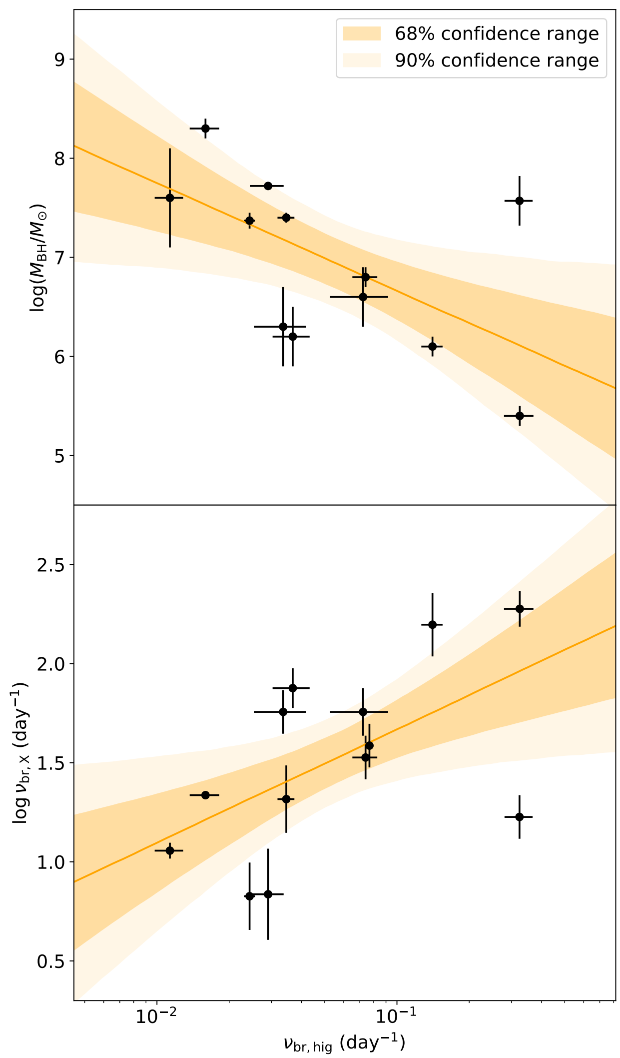

Figure 4.15: Black hole mass and X-ray break frequency versus the high optical break frequencies along with linear fits and their uncertainties.

Table 4.3. Properties of the AGN sample.

Name	$\log(M/M_{\odot})$	$\log \nu_{\text{br,X}}$ (Hz)	$\log \nu_{\text{br,DRW}}$ (day^{-1})	$\log \nu_{\text{br,low}}$ (day^{-1})	$\log \nu_{\text{br,hig}}$ (day^{-1})
MRK 335	7.23 ± 0.04	[-3.9,-2.6]	-2.53 ± 0.13	-2.33 ± 0.09	$\cdots$
ESO 113-G010	$\cdots$	[-3.7,-2.9]	-2.67 ± 0.06	$\cdots$	-1.11 ± 0.02
Fairall 9	8.3 ± 0.1	-3.6	-2.46 ± 0.10	-2.53 ± 0.07	-1.80 ± 0.06
PKS 0558-504	8.48 ± 0.05	[-4.0,-2.8]	-2.72 ± 0.03	$\cdots$	$\cdots$
1H0707-495	6.3 ± 0.5	[-3.5,-2.7]	-2.51 ± 0.07	-1.58 ± 0.07	$\cdots$
ESO 434-G040	7.57 ± 0.25	[-4.1,-2.9]	-2.27 ± 0.10	-2.47 ± 0.10	-0.49 ± 0.06
NGC 3227	6.8 ± 0.1	[-3.6,-2.5]	$\cdots$	-1.83 ± 0.05	-1.13 ± 0.05
REJ 1034+396	6.6 ± 0.3	[-3.5,-2.9]	$\cdots$	$\cdots$	-1.14 ± 0.12
NGC 3516	7.40 ± 0.05	[-4.5,-2.8]	$\cdots$	$\cdots$	-1.46 ± 0.04
NGC 3783	7.37 ± 0.08	[-4.4,-3.4]	-2.54 ± 0.09	-2.52 ± 0.02	-1.61 ± 0.02
NGC 4051	6.1 ± 0.1	[-3.6,-2.2]	-2.06 ± 0.12	-2.18 ± 0.07	-0.85 ± 0.04
NGC 4151	7.55 ± 0.05	[-4.0,-2.9]	-2.37 ± 0.16	-2.46 ± 0.07	$\cdots$
MRK 766	6.2 ± 0.3	[-3.7,-2.4]	$\cdots$	-3.05 ± 0.05	-1.43 ± 0.08
NGC 4395	5.4 ± 0.1	[-3.2,-2.4]	-2.59 ± 0.11	$\cdots$	-0.49 ± 0.06
MCG-06-30-15	6.3 ± 0.4	[-3.7,-2.6]	-2.70 ± 0.17	-2.06 ± 0.09	-1.47 ± 0.11
IC 4329A	8.3 ± 0.5	[-4.4,-3.0]	-2.39 ± 0.16	-2.88 ± 0.16	$\cdots$
Circinus	6.04 ± 0.08	[-4.2,-4.2]	-2.31 ± 0.13	-2.53 ± 0.10	$\cdots$
NGC 5506	8.1 ± 0.2	[-3.9,-2.8]	$\cdots$	$\cdots$	$\cdots$
NGC 5548	7.72 ± 0.02	[-4.2,-2.9]	-2.81 ± 0.09	-2.97 ± 0.03	-1.54 ± 0.07
NGC 6860	7.6 ± 0.5	[-4.0,-2.9]	-2.11 ± 0.10	$\cdots$	-1.95 ± 0.06
ARK 564	6.3 ± 0.5	[-3.1,-2.2]	-2.69 ± 0.10	$\cdots$	$\cdots$
NGC 7469	6.96 ± 0.05	[-4.1,-2.7]	-2.19 ± 0.18	-2.82 ± 0.15	$\cdots$

Note. — $\log(M/M_{\odot})$ and $\log \nu_{\text{br,X}}$ are from González-Martín (2018) and references therein. $\log \nu_{\text{br,DRW}}$ are from fits using the ASAS-SN PSDs only.

4.5.1. Low-frequency Optical Breaks

From the three sets of low-frequency optical breaks, we focused on those from the BPL fits, since they correlate better with the black hole mass and X-ray breaks of the sample.

The ranked correlation test shows that the low-frequency break from the BPL fits weakly correlate with both the black hole mass and the X-ray break frequencies with null probabilities of 0.15 and 0.06, respectively. The break versus black hole mass relation is quite consistent with previous relations (Figure 4.14). We fitted the relationships using

$$\log(\frac{\nu_{\rm br,X}}{\rm day^{-1}}) = \beta_1 \log(\frac{\nu_{\rm br,low}}{10^{-1}{\rm day}^{-1}}) + \delta_1 \tag{4.3}$$

and

$$\log(\frac{M_{\rm BH}}{M_\odot}) = \beta_2 \log(\frac{\nu_{\rm br,low}}{10^{-1}{\rm day}^{-1}}) + \delta_2. \tag{4.4}$$

We find that $\beta_1 = 0.63^{+0.35}_{-0.36}$, $\delta_1 = 2.30^{+0.51}_{-0.54}$, $\beta_2 = -0.69^{+0.59}_{-0.60}$, and $\delta_2 = 6.01^{+0.89}_{-0.87}$, with the results shown in Figure 4.14. Although the relation between $\nu_{\rm br,low}$ and $M_{\rm BH}$ is not statistically significant in this paper, we list our relation as a comparison with previous studies, who found the relation significant (e.g. Kelly et al., 2009; MacLeod et al., 2010; Burke et al., 2021). PG 1613+658, the Seyfert I galaxy with 13 continuous TESS sectors discussed earlier, has a reverberation mapping black hole mass measurement of $\log(M_{\rm BH}/M_\odot) = 8.38^{+0.25}_{-0.16}$ (Kaspi et al., 2000). Using the break frequency from the PSD of the continuous TESS light curve and this $M_{\rm BH}$-$\nu_{\rm br}$ relationship (Equation 4.4), we get $\log(M_{\rm BH}/M_\odot) = 7.39^{+1.43}_{-1.44}$, which agrees with the previous measurement.

4.5.2. High-frequency Optical Breaks

The high-frequency optical breaks were detected in the BPL fits to the combined ASAS-SN and TESS PSDs. They are all at frequencies above 10^{-2} day^{-1}, and resemble the steepening of optical PSDs found in *Kepler* data (Mushotzky et al. 2011; Kasliwal et al. 2015; Aranzana et al. 2018; Smith et al. 2018). Here, we can compare them with the X-ray break frequencies measured for the same set of objects. The high-frequency optical $\nu_{\rm br,hig}$ and X-ray $\nu_{\rm br,X}$ break frequencies are given in Table 4.3 along with $M_{\rm BH}$ and shown in Figure 4.15. The ranked correlation test shows that the high-frequency optical breaks and X-ray breaks are correlated with a null probability of 4%. We also find a hint of a correlation between the high-frequency breaks and the black hole masses, but at lower significance with a null probability of 6%. Figure 4.15 shows fits to the correlations using

$$\log(\frac{\nu_{\rm br,X}}{\rm day^{-1}}) = \beta_3 \log(\frac{\nu_{\rm br,hig}}{10^{-1}{\rm day}^{-1}}) + \delta_3 \tag{4.5}$$

and

$$\log(\frac{M_{\text{BH}}}{M_{\odot}}) = \beta_4 \log(\frac{\nu_{\text{br,hig}}}{10^{-1}\text{day}^{-1}}) + \delta_4. \tag{4.6}$$

With these equations we find that $\beta_3 = 0.57^{+0.30}_{-0.29}$, $\delta_3 = 1.67^{+0.15}_{-0.14}$, $\beta_4 = -1.09^{+0.56}_{-0.56}$, and $\delta_4 = 6.66^{+0.29}_{-0.29}$. If we apply this M_{BH}-ν_{br} relationship to PG 1613+658, we get $\log(M_{\text{BH}}/M_{\odot}) = 6.76^{+0.30}_{-0.30}$, which does not agree with the previous measurement. Further studies are needed to evaluate the validity of this relationship.

We find that the slopes of the BPL fits do not have a strong correlation with the black hole mass or the break frequency. The Pearson's correlation test parameters are $r = -0.17$ and $p = 0.63$ for $\alpha_1 - M_{\text{BH}}$, $r = 0.33$ and $p = 0.32$ for $\alpha_1 - \nu_{\text{br,hig}}$, $r = -0.38$ and $p = 0.28$ for $\alpha_2 - M_{\text{BH}}$, and $r = -0.22$ and $p = 0.51$ for $\alpha_2 - \nu_{\text{br,hig}}$ pairs.

4.5.3. Testing the PSD Fitting Method

To determine whether our PSD fitting method is robust and ensure that the high-frequency breaks are not simply artefacts of combining two sets of PSDs, we selected a number of model parameters, simulated light curves, and performed the PSD fits method as described in Section 4.4 to test if the true model parameters can be recovered. We used the method of Timmer & Koenig (1995) to simulate light curves of a given PSD. Then we added white noise and applied the same sampling windows as the observations. To account for potential misestimation of the measurement noise, we used the three-point method to scale the original measurement uncertainty; we checked three consecutive data points within a certain time frame, find the linear fit, and find the scaling factor for the measurement uncertainties such that $\chi^2 = 1$. This process was repeated for each ASAS-SN and TESS light curve. For this testing, we started with a specific set of parameters, and changed one parameter at a time. We used two different sets of initial parameter sets: $\log(\nu_{\text{br}}/\text{day}^{-1}) = -2.5$, $\alpha_1 = 0.3$, and $\alpha_2 = 2.1$, which correspond to the typical values for low-frequency breaks, and $\log(\nu_{\text{br}}/\text{day}^{-1}) = -1.5$, $\alpha_1 = 1.2$, and $\alpha_2 = 2.1$, which correspond to the typical values for high-frequency breaks. The ranges of parameters are $0.0 \leq \alpha_1 \leq 1.5$, $1.5 \leq \alpha_2 \leq 3.0$ with steps of 0.3, and $-2.8 \leq \log \nu_{\text{br}} \leq -1.0$ with steps of a 0.3 dex.

The results are shown on Figure 4.16. We observe varying levels of biases between the best-fit and input model parameter values. However, the biases can be estimated. For the break frequency, we find that the input and measured break frequencies have an approximately linear relationship, but with offsets. With a shallow α_1 (varying from the low-frequency break setup), measured break frequencies deviate more towards larger values at lower frequencies. With a steeper α_1 (varying form the high-frequency break setup), cases with more TESS sectors show better agreement, while having fewer TESS sectors appears to lead to almost constant values. For both cases, the discrepancy is greatest at the lowest break frequency, but that may be caused by the fact that it is near the PSD lower frequency measurement limit. For power law indices, it appears the measured values have some upper limit to what this method can measure.

To determine which factor contributes the most to the observed discrepancies, we tried using simulated light curves by adding different observational biases one at a time. We tested adding white noise, our treatment of measurement uncertainties, and the effect of observing sampling windows. We used the three simulated TESS sectors for the tests. We find that the light curve sampling window affects the results the most (Figure 4.17), while the white noise and our treatment of measurement uncertainties had little effect on the measured PSD parameters. Since the sampling window effect is significant for ASAS-SN, it makes sense that the discrepancy is greater when there are fewer TESS sectors, where the ASAS-SN PSDs contribute more to the fit. In summary, figures 4.16 and 4.17 show that combining two sets of PSDs from TESS and ASAS-SN introduces a bias on measured break frequency towards higher values. However, the measured values are mostly consistent with true values, suggesting that the $\nu_{\rm br,hig}$ we measured are not due to combining PSDs.

We also attempted calculating the correction for the measured high-frequency break. After correction, the linear trend is still there, but the error bars are much larger and the slope is much shallower (Figure 4.18). The newly measured correlation parameters are $\beta_3 = 0.20^{+0.61}_{-0.69}$, $\delta_3 = 1.52^{+0.49}_{-0.38}$, $\beta_4 = -0.39^{+1.13}_{-1.11}$, and $\delta_4 = 6.94^{+0.70}_{-0.73}$, with the correlation null probabilities of 0.02 and 0.02. With the break frequency correction, $\log(\nu_{\rm br,hig}/{\rm day}^{-1})$ of PG 1613+658 becomes -0.68 ± 1.72, and with the new correlation parameters, its black hole mass is $\log(M_{\rm BH}/M_{\odot}) = 6.76^{+1.58}_{-1.53}$. Compared to the reverberation mapping measurement, the difference in central values is still large, the two values agree within 2σ because of the large uncertainties in the correlation.

4.5.4. Multi-variable Correlation Plane

A number of studies have explored the correlation between the X-ray break frequency and black hole mass, and also examines how other parameters, such as bolometric luminosity and obscuration, can better constrain that correlation (e.g. McHardy et al., 2006; González-Martín & Vaughan, 2012; González-Martín, 2018). We also tested if our newly found correlations are affected by the obscuration, bolometric luminosity, X-ray luminosity, optical luminosity, or optical-to-X-ray luminosity ratio. González-Martín (2018) reports the range of values of N_H and $L_{\rm bol}$ for the sample. The reported $L_{\rm bol}$ is derived from the X-ray luminosity at 2–10 keV:

$$\log\left(\frac{L_{\rm bol}}{L(2-10\ {\rm keV})}\right) = 1.54 + 0.24\mathcal{L} + 0.012\mathcal{L}^2 - 0.0015\mathcal{L}^3, \qquad (4.7)$$

where $\mathcal{L} = \log(L_{\rm bol}/L_{\odot}) - 12$ (Marconi et al., 2004). We used the middle values from the range of N_H and $L_{\rm bol}$ reported by González-Martín (2018) and derived $L_{\rm X}$ from $L_{\rm bol}$. For optical luminosity, we used the median ASAS-SN V-band magnitude, after correcting for galactic reddening and K-correction, to estimate the V-band luminosity of the sample.

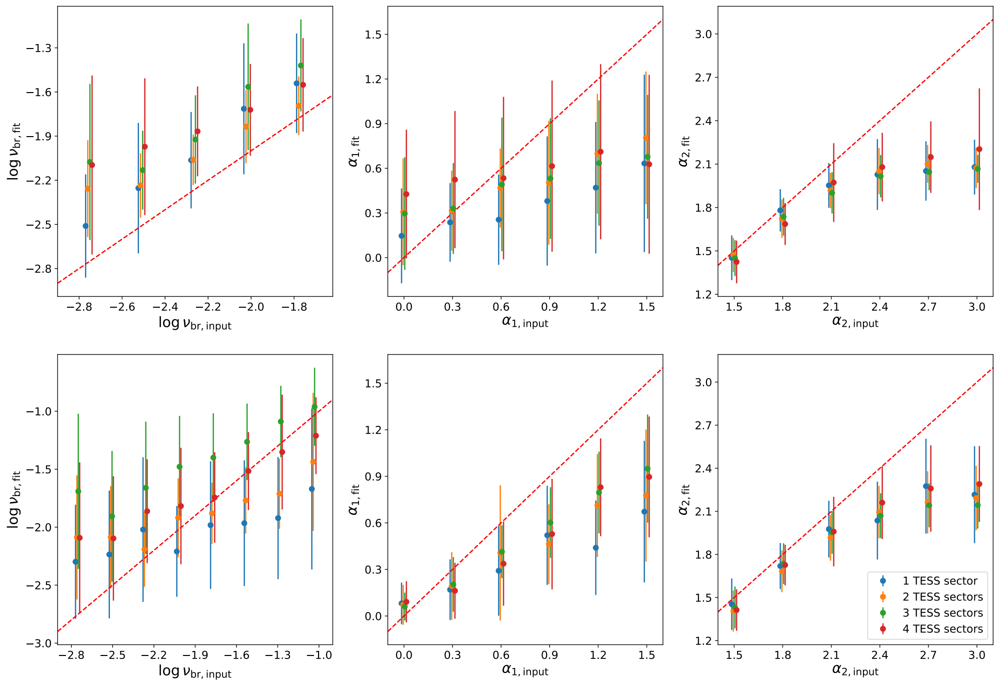

Figure 4.16: Comparisons of BPL model parameters from the PSD fitting method and the true values used for light curve simulations. Variations from the low-frequency and high-frequency break parameters are shown on top and bottom panels, respectively. The dashed red line in each panel represents the one-to-one relation. The data points are slightly offset along the x-axis to make them distinguishable.

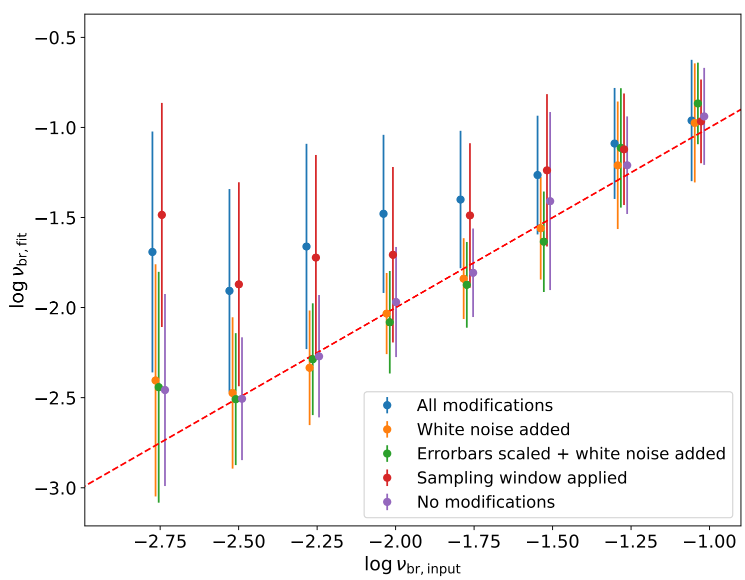

Figure 4.17: Measured break frequencies with different levels of modifications on the light curves versus the input break frequencies for the light curve simulations. The dashed red line represents the one-to-one relation. The data points are slightly offset along the x-axis to make them distinguishable.

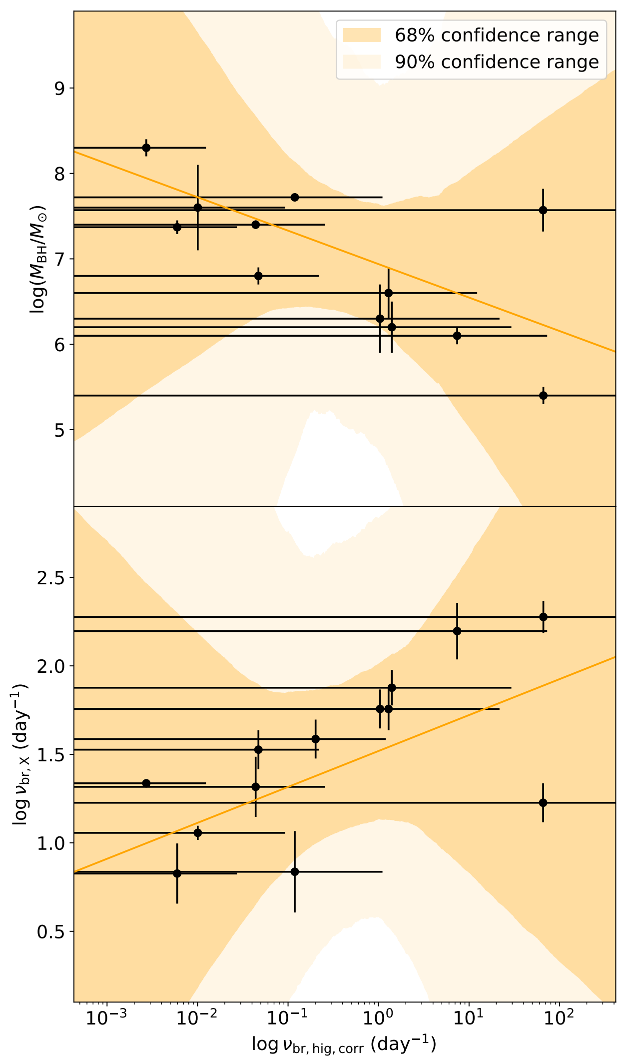

Figure 4.18: Same as Figure 4.15, but with $\nu_{\mathrm{br,hig}}$ corrected for distortion.

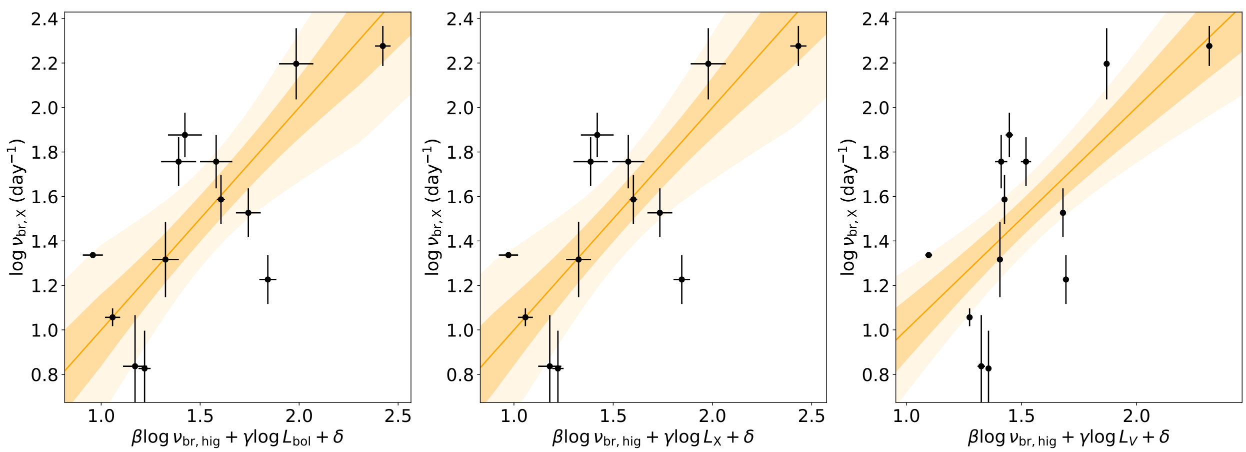

Figure 4.19: Results of fitting the correlation between $\log \nu_{\rm br,X}$ and $\log \nu_{\rm br,hig}$ with the addition of $L_{\rm bol}$ (left), $\log L_{\rm X}$ (middle), or $\log L_V$ (right). The dark and lightly shaded regions represent the 68% and 95% confidence ranges, respectively.

We fitted the multi-variable correlation,

$$Y = \beta \log \nu_{\rm br,opt} + \gamma X + \delta, \tag{4.8}$$

where Y is either $\log \nu_{\rm br,X}$ or $\log M_{\rm BH}$ and $\log \nu_{\rm br,opt}$ is the optical break frequency ($\log \nu_{\rm br,low}$, $\log \nu_{\rm br,hig}$, or $\log \nu_{\rm br,hig,corr}$), X is $\log N_H$, $\log L_{\rm bol}$, $\log L_{\rm X}$, $\log L_V$, or $\log(L_V/L_{\rm X})$ and β, γ, and δ are constants for fitting. We tested all combinations with X, Y, and $\log \nu_{\rm br,opt}$. In most cases, the best-fit β values are consistent with the 1σ range of the original two-parameter correlation values. For some of the combinations, $|\beta|$ approaches zero for the best fit, and the multi-variable correlation is driven by the parameters Y and X. These cases are not related to the main goal of this paper, which is to explore the correlations related to $\nu_{\rm br,opt}$ of either high or low frequencies. Thus, we fixed β values at the best-fit values from the two-parameter correlations for these cases.

We find that, for all combinations, the correlations improve significantly with the addition of X-ray or optical luminosity and slightly with the addition of optical-to-X-ray luminosity ratio or obscuration. The only exception is $\nu_{\rm br,low} - \log M_{\rm BH}$ correlation with the addition of $\log N_{\rm H}$, which had nearly no improvement. For all the multi-variate correlations with the additional X-ray or optical luminosity parameter we tested, the median significance has improved to $p = 0.01$ compared to the median significance of $p = 0.05$ when considering only the original two parameter correlations. By nature of bolometric luminosity being derived from the X-ray luminosity, the effect of adding $L_{\rm bol}$ is nearly the same as adding $L_{\rm X}$. For example, the original two-parameter correlation between $\log \nu_{\rm br,hig}$ and $\log \nu_{\rm X}$ has the correlation coefficient of $r = 0.57$ with $p = 0.04$. With the addition of $\log L_{\rm bol}$, $\log L_{\rm X}$, or $\log L_V$, the correlation coefficient becomes $r = 0.73$ with $p = 0.005$, $r = 0.73$ with $p = 0.005$, and $r = 0.69$ with $p = 0.009$, respectively (Figure 4.19). We present the entirety of our multi-variable fit results in Appendix 4.10.

4.6. Summary and Discussion

We studied AGN variability over six orders of magnitude from minute to decade timescales by combining TESS and ASAS-SN light curves. Our analysis shows that the ASAS-SN and TESS PSDs can be jointly modelled with a normalisation offset due to differences in noise levels and filters. We analysed PG 1613+658, a brigh target in the TESS continuous monitoring regions, that had a TESS light curve spanning more than a year, meaning that there is a significant overlap between PSDs, and found consistent light curves and PSD measurements.

We also compared our results to scaling relations between the low-frequency break and black hole mass from Kelly et al. (2009), MacLeod et al. (2010), and Burke et al. (2021). To compare with the multi-variate correlation from MacLeod et al. (2010), we used their relations assuming a rest frame wavelength of $\lambda_{\rm RF} = 8000$Å, an absolute magnitude of $M_i = -21.3$, and a redshift of $z = 0.02$. All three relations are shown in Figures 4.13 and 4.14.

The $\nu_{\rm br} - M_{\rm BH}$ relationship found using the various DRW fits does not agree with previous studies very well, though the DRW PSD fits that use TESS and ASAS-SN have a similar trend (Figure 4.13). Although the correlations between these DRW break frequencies and X-ray break frequencies are not significant, as can be seen in the bottom panels in Figure 4.13, the X-ray break dependence on the DRW breaks is almost flat, which is contrary to the slope of $\beta_1 = 0.63^{+0.35}_{-0.36}$ between the low-frequency breaks from the BPL model and X-ray breaks.

Burke et al. (2020) performed a similar break frequency analysis on NGC 4395. They used the TESS sector 22 light curve to construct the PSD and fit a BPL. They find a break frequency of $\log(\nu_{\rm br}/{\rm day}^{-1}) = -0.94 \pm 0.25$, which differs from our value of $\log(\nu_{\rm br}/{\rm day}^{-1}) = -0.49 \pm 0.06$. This may be due to our using both TESS and ASAS-SN data. Using only the TESS PSDs, we find $\log(\nu_{\rm br}/{\rm day}^{-1}) = -0.93 \pm 0.07$, which agrees with Burke et al. (2020).

Active galactic nucleus variability PSDs are generally characterised by power laws with breaks; distinct break frequencies have been observed in both optical (e.g. Kelly et al. 2009; MacLeod et al. 2010; Simm et al. 2016; Burke et al. 2021) and X-ray data (e.g. Uttley et al. 2002; Markowitz et al. 2003; González-Martín & Vaughan 2012; González-Martín 2018). Both the optical and X-ray break frequencies are correlated with the black hole mass, but with different scaling relations (e.g. Simm et al. 2016; Burke et al. 2021). The fact that the break frequency and black hole mass have a statistically significant correlation suggests that the AGN variability is closely related to accretion physics.

This paper presents the first analysis comparing optical and X-ray PSDs by exploiting the all-sky nature of the ASAS-SN and TESS surveys. We find a set of high-frequency breaks ($\gtrsim 10^{-2}$day^{-1}) in the joint optical light curves. These high-frequency breaks were previously observed as a steepening of the optical PSD at high frequencies (Mushotzky et al. 2011; Kasliwal et al. 2015; Aranzana et al. 2018; Smith et al. 2018). We find a potential correlation between the X-ray and high-frequency optical break frequencies. The slope of the power law relation of $\beta_3 = 0.59^{+0.27}_{-0.27}$ is close to a relation of $\beta_3 = 0.5$, given the uncertainty, which is shallower than a simple proportional relation of $\beta_3 = 1$. We can interpret the offset between the optical and X-ray break frequencies as the light crossing time between the X-ray and optical emission regions. A slope shallower than a proportional relation implies that the X-ray emission region is smaller than the optical for higher $M_{\rm BH}$. There is also an indication that the high-frequency optical breaks may be correlated with the black hole mass, albeit weakly. This could be a new scaling relationship $\nu_{\rm br} - M_{\rm BH}$, different from those found in previous studies, providing an alternative method for estimating the black hole mass. However, with corrections for sampling, the correlations between the high-frequency breaks and X-ray break frequencies and the black hole mass become less significant. A larger sample is needed to better establish the correlation with more accurate slope measurements.

We further explored whether the correlations discussed in this paper are affected by the X-ray luminosity, optical luminosity, optical-to-X-ray luminosity ratio, or obscuration. We find that including the X-ray, optical, or bolometric luminosity as the third parameter can significantly improve the correlation significances, the optical-to-X-ray luminosity ratio or obscuration only modestly improves the correlation significances. With the inclusion of an additional parameter, the dependence between the X-ray and high-frequency optical break has a power law slope of β_3 in the range 0.1 to 0.8 with a median value of 0.52 (Table 4.6), which is consistent with the original two-parameter slope of $\beta_3 = 0.59 \pm 0.27$.

If the optical and X-ray frequencies are indeed correlated, we can speculate on the implications. The X-ray emission is produced from inverse Compton scattering between UV seed photons from the accretion disc and electrons in the corona. The X-ray emission then irradiates the accretion disc, heating the disc and modifying the optical emission. Therefore, the optical and X-ray variability should show correlations. In fact, short-timescale correlations between optical and X-ray light curves are well established and used as a tool in continuous reverberation mapping studies to constrain optical and X-ray emission sizes (e.g. Shappee et al. 2014b; Edelson et al. 2015; Troyer et al. 2016; McHardy et al. 2018). The correlation we find between the X-ray and optical PSD break frequencies provides independent support that the optical and X-ray emissions are closely related on short timescales. Since the optical PSD on these scales deviates from the extrapolation from longer timescales, the variation in the X-ray emission, through 'reprocessing', can be the main driver for the interaction between optical and X-ray emission on short timescales.

The X-ray emission, which can vary on very short timescales, is speculated to come from the innermost part of the AGN, near the SMBH. On the other hand, the optical emission is believed to come from the accretion disc. Studies in quasar microlensing (e.g. Morgan et al. 2008; Dai et al.

2010) and reverberation mapping (e.g. Shappee et al. 2014b; Edelson et al. 2015; Cackett et al. 2018; Jha et al. 2022) find that the sizes of X-ray and optical emission regions range from 10^{14} to 10^{15} cm and from 10^{15} to 10^{16} cm, respectively. This scale is comparable to our observed difference in characteristic timescales, with $\tau = 1/(2\pi\nu_{\rm br}) \sim 10^{-2}$ day for the X-rays and $\sim 10^{0}$ days for the optical.

In the low-frequency regime ($\lesssim 10^{-2}$day^{-1}), we also find a correlation between the optical and X-ray breaks, with a similar slope $\beta_1 = 0.63^{+0.35}_{-0.36}$. Our analysis results show that the DRW model fits the ASAS-SN PSDs well. We also roughly recover the DRW break versus black hole mass relation measured in the literature. When high-frequency TESS PSDs are introduced, the DRW work less well. The BPL fits show that the power law indices deviate from the DRW values of 0 and -2, as shown on the distributions on Figure 4.12, especially for the low-frequency slope. A few objects potentially have two break frequencies, according to the BPL fits (Figure 4.6). This means that AGN variability is more complicated and may be governed by different physical processes at different scales. For example, the longer-term variability could be mainly described by a DRW model, physically related to magnetorotational instability or other disc variability mechanisms (e.g. Kelly et al. 2009; MacLeod et al. 2010), while the short-term optical variability is strongly affected by other variability mechanisms, such as the reprocessing of X-rays.

4.7. Data availability

Tables 4.4 and 4.5 are available in full in electronic form at the CDS via anonymous ftp to cdsarc.u-strasbg.fr (130.79.128.5) or via http://cdsweb.u-strasbg.fr/cgi-bin/qcat?J/A+A/.

4.8. Acknowledgments

We thank the anonymous referee for constructive suggestions. H.Y. and X.D. would like to acknowledge NASA funds 80NSSC22K0488, 80NSSC23K0379 and NSF fund AAG2307802. H.Y. thank the Avenir fellowship. We also thank the OU Supercomputing Center for Education & Research (OSCER) at the University of Oklahoma for providing the computing resources.

Table 4.4. ASAS-SN light curves used for this study (extract).

Name	Filter	Date (HJD)	Flux (mJy)	Flux err (mJy)
MRK 335	V	2456233.79722	8.67400	0.15044
	V	2456461.02849	8.27800	0.25125
	V	2456470.02629	8.55800	0.38962
		...	...	...
MRK 335	g	2458017.75063	5.93600	0.15929
	g	2458035.89937	5.95800	0.15955
	g	2458035.89942	6.47800	0.16570
		...	...	...
ESO 113-G010	V	2456789.93382	7.86700	0.38656
	V	2456805.91323	7.31200	0.10935
	V	2456809.90571	7.12700	0.12181
		...	...	...

Note. — This table is available in a machine-readable form.

4.9. Appendix A: Light curve compilation

Here, we present the compilation of light curves used for this study in both text and visual formats. ASAS-SN and TESS light curves are shown in Tables 4.4 and 4.5 and Figures 4.20, 4.21, and 4.22.

4.10. Appendix B: Multi-variable correlation fitting results

In this section, we present the results of fitting the multi-variable correlations (Equation 4.8). Figures 4.23 and 4.24 show the fitting plots with the addition of X-ray and V-band luminosities, which improved the fit the most. Table 4.6 lists all values we obtained from the fits. The units used for $\nu_{\rm br}$, $M_{\rm BH}$, N_H, and L are day^{-1}, $M_\odot$, cm^{-2}, and erg s^{-1}, respectively.

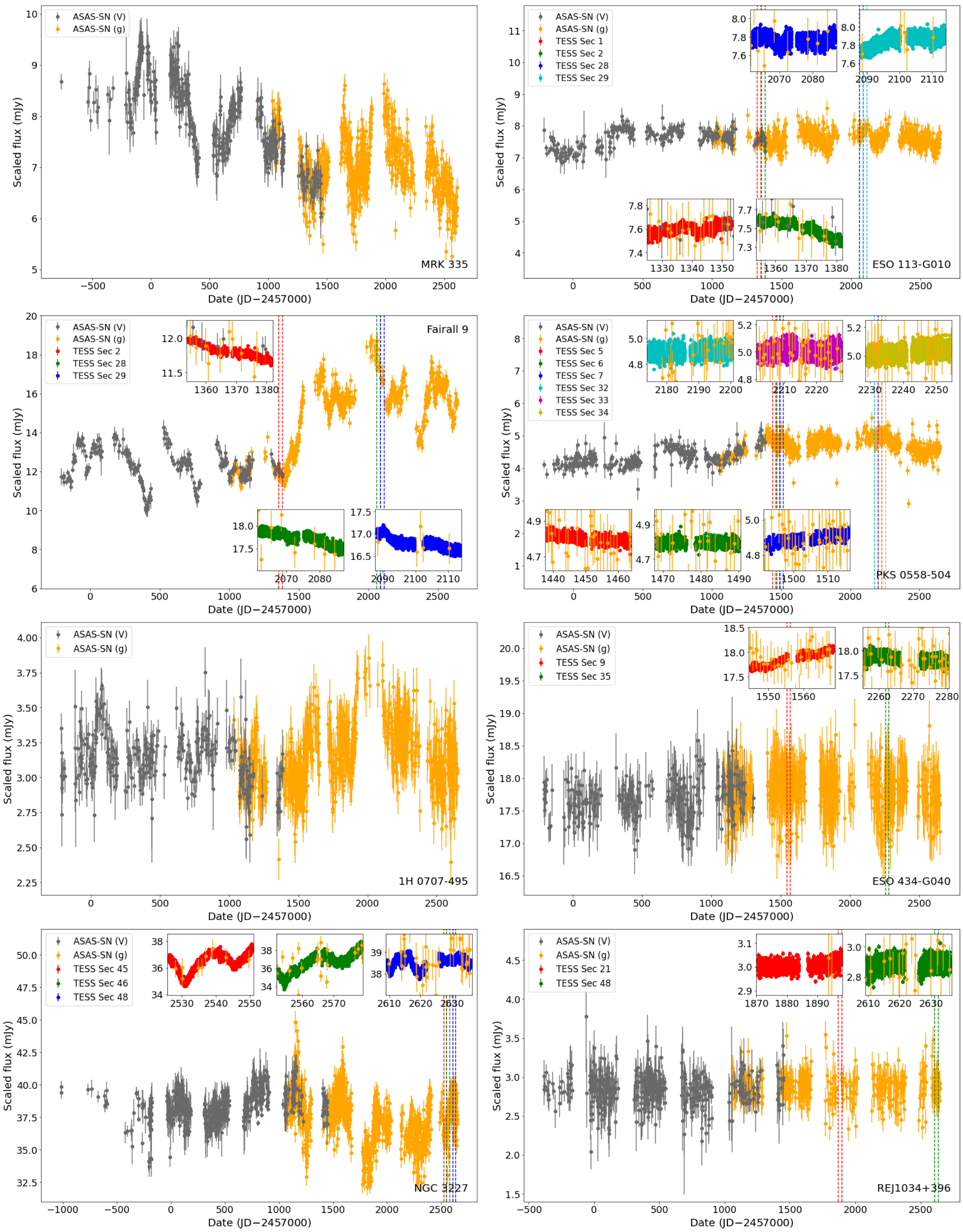

Figure 4.20: ASAS-SN light curves of MRK 335, ESO 113-G010, Fairall 9, PKS 0558-504, 1H 0707-495, ESO 434-G040, NGC 3227, and RE J1034+396. The TESS sectors are marked and shown in the insets. The light curves are scaled to overlap.

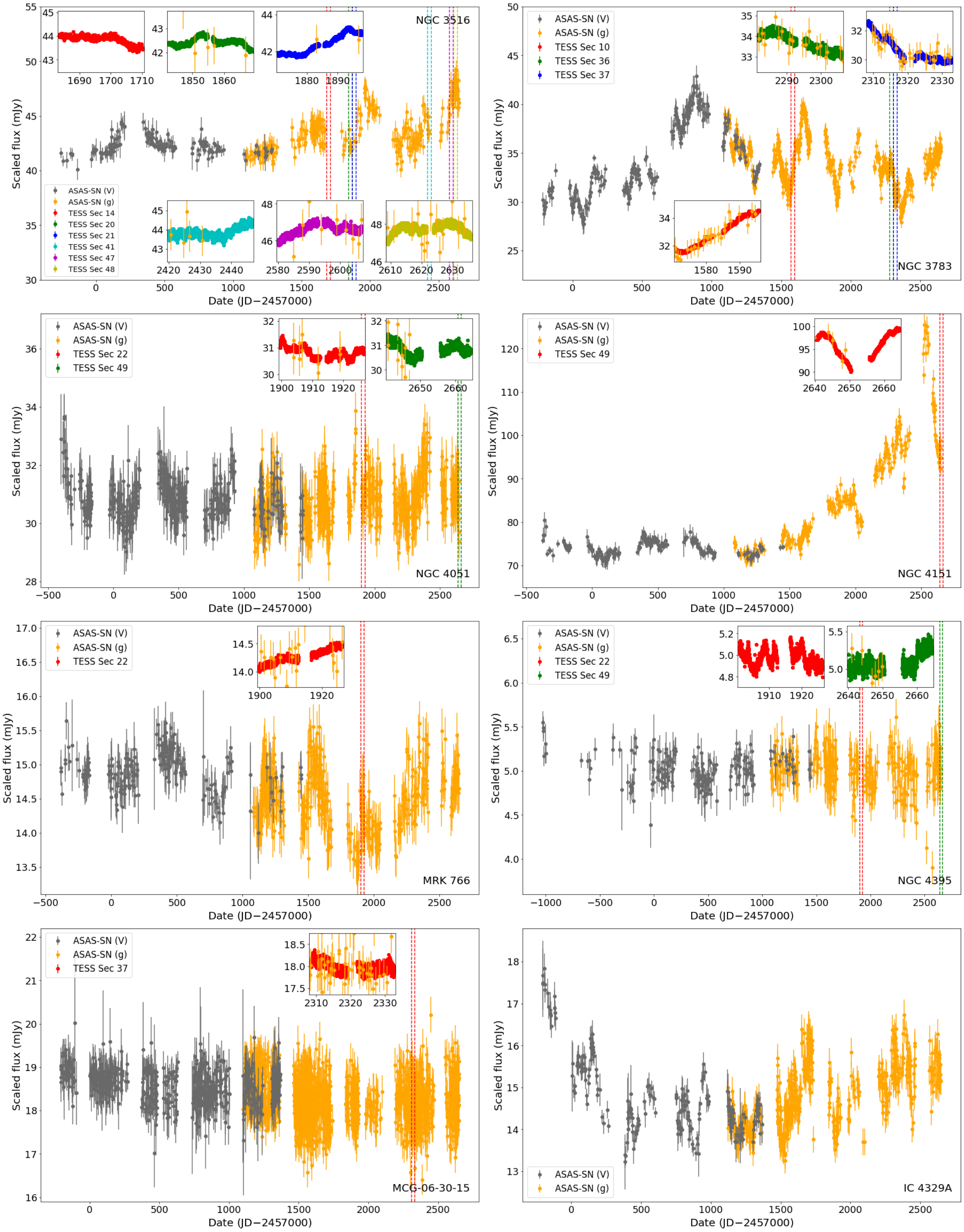

Figure 4.21: Continuation of Figure 4.20, for NGC 3516, NGC 3783, NGC 4051, NGC 4151, MRK 766, NGC 4395, MCG-06-30-15, and IC 4329A.

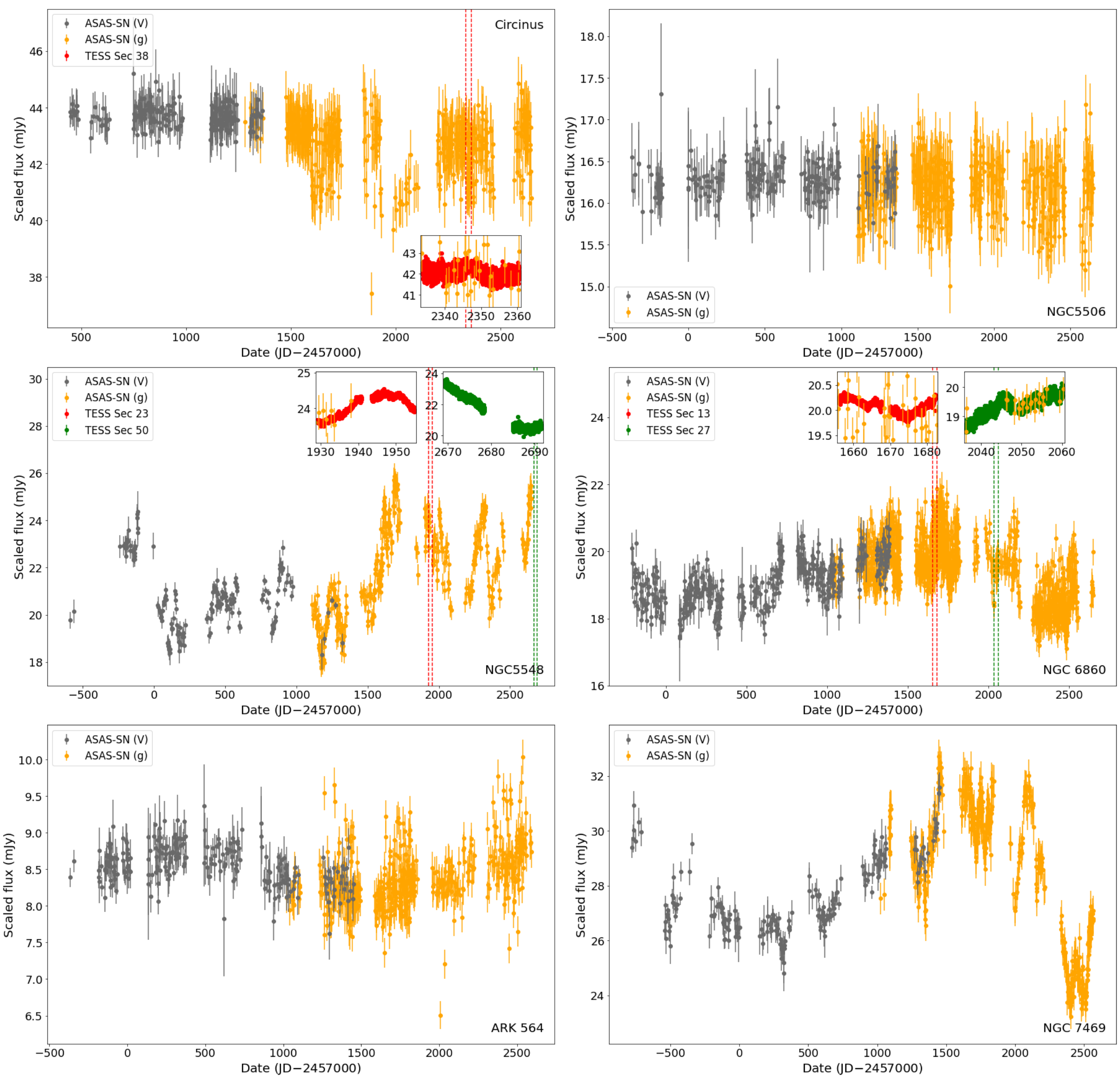

Figure 4.22: Continuation of Figure 4.20, for Circinus, NGC 5506, NGC 5548, NGC 6860, ARK 564, and NGC 7469.

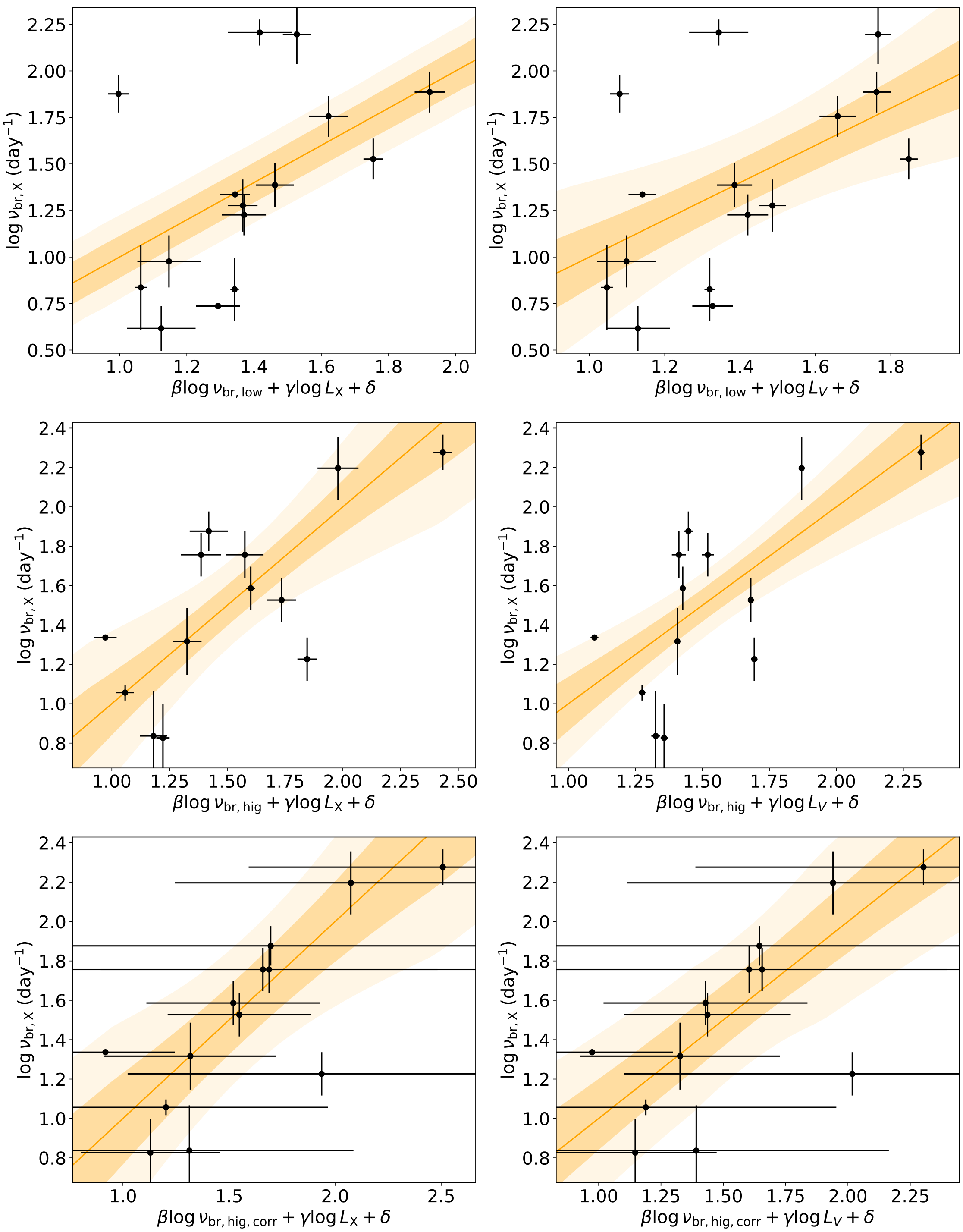

Figure 4.23: Multi-variable correlation between X-ray break frequency and different optical break frequencies–$\log \nu_{\rm br,low}$ (top), $\log \nu_{\rm br,hig}$ (middle), and $\log \nu_{\rm br,hig,corr}$ (bottom)–with the addition of X-ray luminosity (left) or V-band luminosity (right). The dark and lightly shaded regions represent the 68% and 95% confidence ranges, respectively.

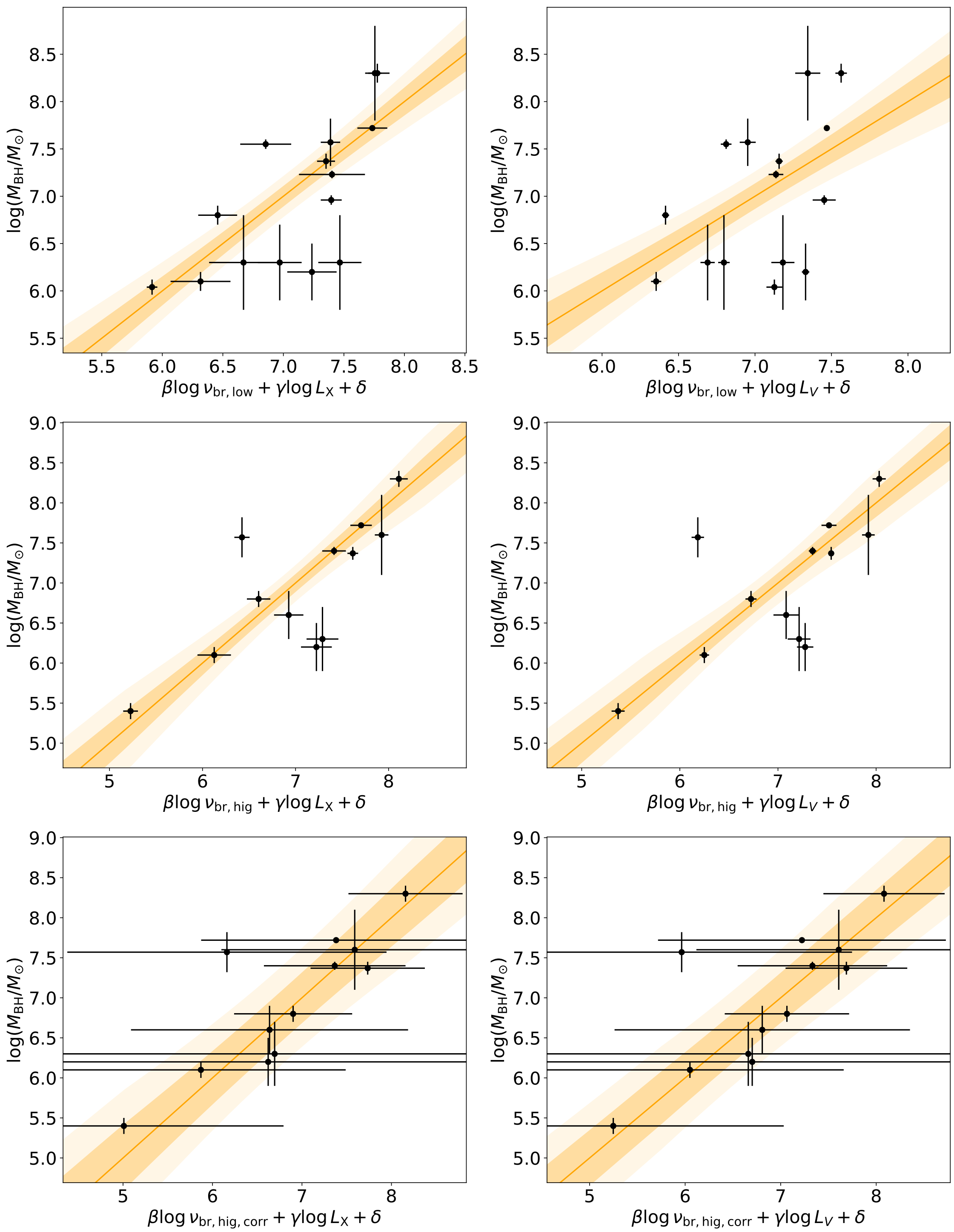

Figure 4.24: Same as Figure 4.23, but with $M_{\rm BH}$ instead of $\nu_{\rm br,X}$.

Table 4.5. TESS light curves used for this study (extract).

Name	Sector	Date (TJD)[1]	Flux (mJy)	Flux err (mJy)
ESO 113-G010	1	1325.315786	8.58287	0.01241
	1	1325.336620	8.58208	0.01249
	1	1325.357454	8.61625	0.01255
		...	...	...
ESO 113-G010	2	1354.107720	8.64351	0.01330
	2	1354.128553	8.60523	0.01331
	2	1354.149386	8.61716	0.01331
		...	...	...
Fairall 9	2	1354.107720	13.76622	0.01327
	2	1354.128553	13.81294	0.01326
	2	1354.149386	13.79073	0.01326
		...	...	...

Note. — This table is available in a machine-readable form. [1]TJD = JD - 2457000.

Table 4.6. Parameters obtained from multi-variable correlation fittings to Equation 4.8 and Pearson correlation strength and null probability.

Y	$\log \nu_{\rm br,opt}$	X	β	γ	δ	r	p
$\log \nu_{\rm br,X}$	$\log \nu_{\rm br,low}$	$\log N_H$	$0.83^{+0.05}_{-0.05}$	$-0.12^{+0.07}_{-0.07}$	$6.07^{+1.42}_{-1.44}$	0.50	0.06
		$\log L_{\rm bol}$	$0.63^{+0.05}_{-0.05}$	$0.01^{+0.02}_{-0.02}$	$2.48^{+0.81}_{-0.82}$	0.50	0.06
		$\log L_{\rm X}$	$0.63^{+0.05}_{-0.05}$	$0.02^{+0.02}_{-0.02}$	$2.22^{+0.73}_{-0.73}$	0.50	0.06
		$\log L_V$	$0.52^{+0.05}_{-0.05}$	$-0.19^{+0.06}_{-0.06}$	$11.13^{+2.59}_{-2.59}$	0.54	0.04
		$\log(L_V/L_{\rm X})$	$0.74^{+0.05}_{-0.05}$	$-0.18^{+0.08}_{-0.08}$	$3.40^{+0.17}_{-0.17}$	0.53	0.04
	$\log \nu_{\rm br,hig}$	$\log N_H$	$0.65^{+0.04}_{-0.03}$	$-0.47^{+0.11}_{-0.11}$	$12.48^{+2.29}_{-2.42}$	0.63	0.02
		$\log L_{\rm bol}$	0.57	$-0.18^{+0.05}_{-0.05}$	$10.25^{+2.09}_{-2.1}$	0.73	0.005
		$\log L_{\rm X}$	0.57	$-0.21^{+0.05}_{-0.05}$	$11.25^{+2.24}_{-2.26}$	0.73	0.005
		$\log L_V$	$0.21^{+0.04}_{-0.04}$	$-0.25^{+0.05}_{-0.05}$	$12.75^{+2.28}_{-2.29}$	0.69	0.009
		$\log(L_V/L_{\rm X})$	$0.66^{+0.04}_{-0.04}$	$0.60^{+0.09}_{-0.09}$	$1.70^{+0.13}_{-0.13}$	0.69	0.01
	$\log \nu_{\rm br,hig,corr}$	$\log N_H$	$0.18^{+0.06}_{-0.06}$	$-0.72^{+0.21}_{-0.21}$	$17.08^{+4.49}_{-4.56}$	0.59	0.03
		$\log L_{\rm bol}$	0.20	$-0.18^{+0.06}_{-0.06}$	$9.33^{+2.45}_{-2.49}$	0.78	0.002
		$\log L_{\rm X}$	0.20	$-0.21^{+0.06}_{-0.06}$	$10.43^{+2.56}_{-2.59}$	0.78	0.002
		$\log L_V$	0.20	$-0.12^{+0.04}_{-0.04}$	$6.66^{+1.68}_{-1.57}$	0.70	0.008
		$\log(L_V/L_{\rm X})$	$0.11^{+0.03}_{-0.03}$	$0.65^{+0.09}_{-0.1}$	$0.79^{+0.15}_{-0.16}$	0.71	0.006
$\log M_{\rm BH}$	$\log \nu_{\rm br,low}$	$\log N_H$	$-0.86^{+0.09}_{-0.09}$	$0.1^{+0.04}_{-0.04}$	$2.74^{+0.86}_{-0.85}$	0.39	0.15
		$\log L_{\rm bol}$	$-0.30^{+0.09}_{-0.09}$	$0.53^{+0.06}_{-0.06}$	$-16.62^{+2.42}_{-2.43}$	0.71	0.003
		$\log L_{\rm X}$	$-0.30^{+0.09}_{-0.09}$	$0.62^{+0.06}_{-0.06}$	$-19.81^{+2.7}_{-2.7}$	0.71	0.003
		$\log L_V$	$-0.50^{+0.09}_{-0.09}$	$0.45^{+0.07}_{-0.07}$	$-13.94^{+3.01}_{-2.92}$	0.49	0.07
		$\log(L_V/L_{\rm X})$	$-0.52^{+0.09}_{-0.09}$	$-0.58^{+0.08}_{-0.08}$	$6.52^{+0.26}_{-0.26}$	0.60	0.02
	$\log \nu_{\rm br,hig}$	$\log N_H$	$-1.60^{+0.08}_{-0.08}$	$1.18^{+0.18}_{-0.18}$	$-19.92^{+3.85}_{-3.82}$	0.61	0.03
		$\log L_{\rm bol}$	-1.09	$0.38^{+0.05}_{-0.05}$	$-10.78^{+2.02}_{-2.02}$	0.77	0.003
		$\log L_{\rm X}$	-1.09	$0.43^{+0.05}_{-0.05}$	$-12.72^{+2.26}_{-2.28}$	0.77	0.004
		$\log L_V$	-1.09	$0.33^{+0.05}_{-0.05}$	$-8.61^{+2.0}_{-1.99}$	0.70	0.01
		$\log(L_V/L_{\rm X})$	$-1.29^{+0.08}_{-0.08}$	$-1.08^{+0.1}_{-0.1}$	$6.45^{+0.18}_{-0.18}$	0.64	0.02
	$\log \nu_{\rm br,hig,corr}$	$\log N_H$	$-0.45^{+0.13}_{-0.13}$	$1.63^{+0.18}_{-0.19}$	$-27.93^{+3.99}_{-3.93}$	0.66	0.02
		$\log L_{\rm bol}$	-0.39	$0.36^{+0.06}_{-0.06}$	$-9.01^{+2.4}_{-2.39}$	0.84	0.0006
		$\log L_{\rm X}$	-0.39	$0.42^{+0.06}_{-0.06}$	$-11.00^{+2.7}_{-2.69}$	0.84	0.0007
		$\log L_V$	-0.39	$0.29^{+0.04}_{-0.04}$	$-5.88^{+1.77}_{-1.76}$	0.77	0.003

Table 4.6 (cont'd)

Y	$\log \nu_{\rm br,opt}$	X	β	γ	δ	r	p
		$\log(L_V/L_{\rm X})$	$-0.26^{+0.06}_{-0.06}$	$-1.07^{+0.1}_{-0.1}$	$8.10^{+0.25}_{-0.25}$	0.74	0.006

Note. — β values with no uncertainties indicate the cases where β was fixed.

CHAPTER 5

Conclusions

This dissertation contains a series of studies presenting the variability analyses of AGNs.

Previous studies on variability-based AGN selection methods used data sets with limited sensitivity, short light curve duration, and small numbers of data points. Such data sets were unable to detect small variability amplitude, so most previous variability selected AGNs were luminous AGNs. This dissertation demonstrated that, with high quality light curves, many LLAGNs with small variability amplitude can be discovered. Also, many of these variability selected LLAGNs are not classified as AGNs by traditional methods, which means that this method is a powerful tool to discover many new AGNs.

The AGN fraction among galaxies and its environmental dependence is important to study, as they can provide clues about galaxy evolution and the AGN activity timescale. To measure the AGN fraction, it is crucial to identify AGNs from a parent sample of galaxies. Previous studies on this topic used traditional methods for AGN classification, so their AGN samples largely consisted of luminous AGNs with a significant incompleteness in the LLAGN regime. With the variability selection method, more LLAGNs can be discovered, which can give a more complete picture of AGN populations.

However, my AGN fraction analysis is also incomplete. Our parent sample includes only bright galaxies with SDSS spectra, which is only a small fraction of all galaxies. It may also be slightly biased; the SDSS spectroscopic sample excludes many luminous AGNs, which is potentially the reason our variability selected AGNs were mostly LLAGNs. This incompleteness can be improved by using a larger and more complete sample of galaxies in future studies.

My optical PSD analysis has two traits that distinguishes itself from previous AGN PSD studies. First, I examined the joint PSDs from both ground-based and space-based observations that span over 6 orders of magnitude. In contrast, most previous AGN optical PSD studies only cover 2–3 orders of magnitude. As a result, a new set of break frequencies at high frequency was discovered. Second, the all-sky nature of ASAS-SN and TESS surveys allowed me to compare optical and X-ray PSDs of the same sample, and I checked for a correlation between optical and X-ray break frequencies, while previous studies on optical and X-ray PSDs analyzed different samples. This analysis led to a discovery of a potential correlation between optical and X-ray break frequencies. This provides a new method of spatial analysis of AGN structures.

Below, I list the detailed conclusions from this dissertation.

1. Variability is a useful tool to identify AGNs among quiescent galaxies.

2. The variability selection method is effective in discovering LLAGNs using high-cadence long-timescale timing surveys.

3. The variability selected AGN fraction is measured to be approximately 3%, which is mostly LLAGNs. Many luminous AGNs are likely to be excluded from the parent sample of galaxies used for this study.

4. Variability selected AGNs are often not classified as AGNs by traditional methods, suggesting that this method is important for discovering new AGNs.

5. LLAGNs appear to be more common in denser environments, which is an opposite trend compared to luminous AGNs, possibly hinting different trigger mechanisms; while luminous AGNs are more commonly triggered by gas inflows in the absence of the ram pressure stripping effect in galaxy clusters, LLAGNs are more commonly triggered by tidal disruptions and disk instabilities from merger events.

6. A new set of break frequencies in optical AGN PSDs is discovered at 1–2 orders of magnitude greater than previously measured break frequencies.

7. Optical break frequencies appear to be correlated with X-ray break frequencies, suggesting a potential interaction between X-ray emitting region and optical emitting region within the AGN structure.

AGN variability studies are expected to improve in upcoming years, both in quantity and quality. An unprecedented amount of data is being produced every night right now. In addition to current facilities accumulating more data, more powerful instruments are scheduled to be deployed. The Vera C. Rubin Observatory is planned to go online in 2025. Its main project is the Legacy Survey of Space and Time (LSST; Ivezić et al. 2019), which is expected to produce terabytes of data every night. The Nancy Grace Roman Space Telescope (Mosby et al., 2020), planned to launch in 2026, is planned to conduct multiple time-domain surveys. Earth 2.0 (Zang et al., 2024) is another space-based survey project, planned to launch to the L2 Lagrange point in 2027. Though its primary mission is searching for exoplanets, it is expected to yield a great amount of high quality data for other fields including AGN variability studies, just like TESS did.

These upcoming instruments will be able to detect fainter objects and smaller variability amplitudes. The Vera C. Rubin Observatory will have the limiting magnitude of approximately $r \sim 25$, which means it is two orders of magnitude more powerful than ASAS-SN, which has the limiting magnitude of $g \sim 18$. Applying the variability selection method in this dissertation on these data sets will result in discovering many new AGNs and at much higher redshifts. Applying the PSD analysis in this dissertation to these future data sets can measure orders of magnitude more high frequency optical PSD breaks at different redshifts and constrain their correlation with AGN parameters, such as the black hole mass. In addition, the Nancy Grace Roman Space Telescope will be observing in the near-infrared, which will enable AGN variability studies in the infrared, which is currently largely unexplored.

Bibliography

Abdurro'uf, Accetta, K., Aerts, C., et al. 2022, ApJS, 259, 35, doi: 10.3847/1538-4365/ac4414

Ahumada, R., Prieto, C. A., Almeida, A., et al. 2020, ApJS, 249, 3, doi: 10.3847/1538-4365/ab929e

Alard, C. 2000, A&AS, 144, 363, doi: 10.1051/aas:2000214

Alard, C., & Lupton, R. H. 1998, ApJ, 503, 325, doi: 10.1086/305984

Alberts, S., Pope, A., Brodwin, M., et al. 2016, ApJ, 825, 72, doi: 10.3847/0004-637X/825/1/72

Alcock, C., Allsman, R. A., Alves, D., et al. 1997, ApJ, 486, 697, doi: 10.1086/304535

Antonucci, R. 1993, ARA&A, 31, 473, doi: 10.1146/annurev.aa.31.090193.002353

Aranzana, E., Körding, E., Uttley, P., Scaringi, S., & Bloemen, S. 2018, MNRAS, 476, 2501, doi: 10.1093/mnras/sty413

Aretxaga, I., Cid Fernandes, R., & Terlevich, R. J. 1997, MNRAS, 286, 271, doi: 10.1093/mnras/286.2.271

Assef, R. J., Kochanek, C. S., Brodwin, M., et al. 2010, ApJ, 713, 970, doi: 10.1088/0004-637X/713/2/970

Astropy Collaboration, Price-Whelan, A. M., Lim, P. L., et al. 2022, ApJ, 935, 167, doi: 10.3847/1538-4357/ac7c74

Balbus, S. A., & Hawley, J. F. 1991, ApJ, 376, 214, doi: 10.1086/170270

Baldassare, V. F., Geha, M., & Greene, J. 2020, ApJ, 896, 10, doi: 10.3847/1538-4357/ab8936

Baldwin, J. A., Phillips, M. M., & Terlevich, R. 1981, PASP, 93, 5, doi: 10.1086/130766

Bauer, A., Baltay, C., Coppi, P., et al. 2009, ApJ, 696, 1241, doi: 10.1088/0004-637X/696/2/1241

Bellm, E. C., Kulkarni, S. R., Graham, M. J., et al. 2019, PASP, 131, 018002, doi: 10.1088/1538-3873/aaecbe

Bennert, V. N., Treu, T., Ding, X., et al. 2021, ApJ, 921, 36, doi: 10.3847/1538-4357/ac151a

Bentz, M. C., & Manne-Nicholas, E. 2018, ApJ, 864, 146, doi: 10.3847/1538-4357/aad808

Blecha, L., Snyder, G. F., Satyapal, S., & Ellison, S. L. 2018, MNRAS, 478, 3056, doi: 10.1093/mnras/sty1274

Bornancini, C., & García Lambas, D. 2018, MNRAS, 479, 2308, doi: 10.1093/mnras/sty1659

Borucki, W. J., Koch, D., Basri, G., et al. 2010, Science, 327, 977, doi: 10.1126/science.1185402

Brinchmann, J., Charlot, S., White, S. D. M., et al. 2004, MNRAS, 351, 1151, doi: 10.1111/j.1365-2966.2004.07881.x

Burke, C. J., Shen, Y., Chen, Y.-C., et al. 2020, ApJ, 899, 136, doi: 10.3847/1538-4357/aba3ce

Burke, C. J., Shen, Y., Blaes, O., et al. 2021, Science, 373, 789, doi: 10.1126/science.abg9933

Butler, N. R., & Bloom, J. S. 2011, AJ, 141, 93, doi: 10.1088/0004-6256/141/3/93

Cackett, E. M., Chiang, C.-Y., McHardy, I., et al. 2018, ApJ, 857, 53, doi: 10.3847/1538-4357/aab4f7

Cappellari, M., & Emsellem, E. 2004, PASP, 116, 138, doi: 10.1086/381875

Cash, W. 1979, ApJ, 228, 939, doi: 10.1086/156922

Chen, K., & Halpern, J. P. 1989, ApJ, 344, 115, doi: 10.1086/167782

Chen, Y.-C., & Hwang, C.-Y. 2017, Ap&SS, 362, 230, doi: 10.1007/s10509-017-3210-0

Cid Fernandes, R., Stasińska, G., Mateus, A., & Vale Asari, N. 2011, MNRAS, 413, 1687, doi: 10.1111/j.1365-2966.2011.18244.x

Constantin, A., Hoyle, F., & Vogeley, M. S. 2008, ApJ, 673, 715, doi: 10.1086/524310

Dai, X., Chartas, G., Eracleous, M., & Garmire, G. P. 2004, ApJ, 605, 45, doi: 10.1086/382205

Dai, X., Kochanek, C. S., Chartas, G., et al. 2010, ApJ, 709, 278, doi: 10.1088/0004-637X/709/1/278

de Menezes, R., Nemmen, R., Finke, J. D., Almeida, I., & Rani, B. 2020, MNRAS, 492, 4120, doi: 10.1093/mnras/staa083

Dexter, J., & Agol, E. 2011, ApJL, 727, L24, doi: 10.1088/2041-8205/727/1/L24

di Clemente, A., Giallongo, E., Natali, G., Trevese, D., & Vagnetti, F. 1996, ApJ, 463, 466, doi: 10.1086/177261

Dyson, F. W., Eddington, A. S., & Davidson, C. 1920, Philosophical Transactions of the Royal Society of London Series A, 220, 291, doi: 10.1098/rsta.1920.0009

Eastman, J., Martini, P., Sivakoff, G., et al. 2007, ApJL, 664, L9, doi: 10.1086/520577

Edelson, R., Turner, T. J., Pounds, K., et al. 2002, ApJ, 568, 610, doi: 10.1086/323779

Edelson, R., Gelbord, J. M., Horne, K., et al. 2015, ApJ, 806, 129, doi: 10.1088/0004-637X/806/1/129

Edge, D. O., Shakeshaft, J. R., McAdam, W. B., Baldwin, J. E., & Archer, S. 1959, MmRAS, 68, 37

Einstein, A. 1915, Sitzungsberichte der Königlich Preussischen Akademie der Wissenschaften, 844

Eisenhauer, F., Genzel, R., Alexander, T., et al. 2005, ApJ, 628, 246, doi: 10.1086/430667

Elitzur, M., & Shlosman, I. 2006, ApJL, 648, L101, doi: 10.1086/508158

Ellison, S. L., Patton, D. R., Mendel, J. T., & Scudder, J. M. 2011, MNRAS, 418, 2043, doi: 10.1111/j.1365-2966.2011.19624.x

Ellison, S. L., Viswanathan, A., Patton, D. R., et al. 2019, MNRAS, 487, 2491, doi: 10.1093/mnras/stz1431

Elmer, E., Almaini, O., Merrifield, M., et al. 2020, MNRAS, 493, 3026, doi: 10.1093/mnras/staa381

Evans, P. A., Page, K. L., Osborne, J. P., et al. 2020, ApJS, 247, 54, doi: 10.3847/1538-4365/ab7db9

Event Horizon Telescope Collaboration, Akiyama, K., Alberdi, A., et al. 2019, ApJL, 875, L1, doi: 10.3847/2041-8213/ab0ec7

—. 2022, ApJL, 930, L12, doi: 10.3847/2041-8213/ac6674

Fausnaugh, M. M., Vallely, P. J., Kochanek, C. S., et al. 2021, ApJ, 908, 51, doi: 10.3847/1538-4357/abcd42

Ferrarese, L., & Merritt, D. 2000, ApJL, 539, L9, doi: 10.1086/312838

Fu, H., Steffen, J. L., Gross, A. C., et al. 2018, ApJ, 856, 93, doi: 10.3847/1538-4357/aab364

Gavazzi, G., Savorgnan, G., & Fumagalli, M. 2011, A&A, 534, A31, doi: 10.1051/0004-6361/201117461

Gebhardt, K., Bender, R., Bower, G., et al. 2000, ApJL, 539, L13, doi: 10.1086/312840

Gehrels, N. 1986, ApJ, 303, 336, doi: 10.1086/164079

Gkini, A., Plionis, M., Chira, M., & Koulouridis, E. 2021, A&A, 650, A75, doi: 10.1051/0004-6361/202140278

González-Martín, O. 2018, ApJ, 858, 2, doi: 10.3847/1538-4357/aab7ec

González-Martín, O., & Vaughan, S. 2012, A&A, 544, A80, doi: 10.1051/0004-6361/201219008

Graham, A. W., Onken, C. A., Athanassoula, E., & Combes, F. 2011, MNRAS, 412, 2211, doi: 10.1111/j.1365-2966.2010.18045.x

Grandi, P., Tagliaferri, G., Giommi, P., Barr, P., & Palumbo, G. G. C. 1992, ApJS, 82, 93, doi: 10.1086/191710

Green, K., Elmer, E., Maltby, D. T., et al. 2024, MNRAS, 531, 2551, doi: 10.1093/mnras/stae1322

Haardt, F., & Maraschi, L. 1991, ApJL, 380, L51, doi: 10.1086/186171

Haggard, D., Green, P. J., Anderson, S. F., et al. 2010, ApJ, 723, 1447, doi: 10.1088/0004-637X/723/2/1447

Henden, A. A., Levine, S., Terrell, D., & Welch, D. L. 2015, in American Astronomical Society Meeting Abstracts, Vol. 225, American Astronomical Society Meeting Abstracts #225, 336.16

Ho, L. C. 2008, ARA&A, 46, 475, doi: 10.1146/annurev.astro.45.051806.110546

Ho, L. C., Filippenko, A. V., & Sargent, W. L. W. 1997a, ApJS, 112, 315, doi: 10.1086/313041

—. 1997b, ApJ, 487, 568, doi: 10.1086/304638

Ho, L. C., Filippenko, A. V., Sargent, W. L. W., & Peng, C. Y. 1997c, ApJS, 112, 391, doi: 10.1086/313042

Hopkins, P. F., & Elvis, M. 2010, MNRAS, 401, 7, doi: 10.1111/j.1365-2966.2009.15643.x

Hopkins, P. F., & Hernquist, L. 2009, ApJ, 698, 1550, doi: 10.1088/0004-637X/698/2/1550

Hopkins, P. F., Kocevski, D. D., & Bundy, K. 2014, MNRAS, 445, 823, doi: 10.1093/mnras/stu1736

Hviding, R. E., Hainline, K. N., Rieke, M., et al. 2022, AJ, 163, 224, doi: 10.3847/1538-3881/ac5e33

Ivezić, Ž., Kahn, S. M., Tyson, J. A., et al. 2019, ApJ, 873, 111, doi: 10.3847/1538-4357/ab042c

Jarrett, T. H., Cohen, M., Masci, F., et al. 2011, ApJ, 735, 112, doi: 10.1088/0004-637X/735/2/112

Järvelä, E., Savolainen, T., Berton, M., et al. 2024, MNRAS, 532, 3069, doi: 10.1093/mnras/stae1701

Jayasinghe, T., Kochanek, C. S., Stanek, K. Z., et al. 2018, MNRAS, 477, 3145, doi: 10.1093/mnras/sty838

Jayasinghe, T., Stanek, K. Z., Kochanek, C. S., et al. 2019, MNRAS, 485, 961, doi: 10.1093/mnras/stz444

Jha, V. K., Joshi, R., Chand, H., et al. 2022, MNRAS, 511, 3005, doi: 10.1093/mnras/stac109

Karachentsev, I. D., Karachentseva, V. E., Huchtmeier, W. K., & Makarov, D. I. 2004, AJ, 127, 2031, doi: 10.1086/382905

Karachentsev, I. D., & Makarov, D. I. 1999, in IAU Symposium, Vol. 186, Galaxy Interactions at Low and High Redshift, ed. J. E. Barnes & D. B. Sanders, 109

Kasliwal, V. P., Vogeley, M. S., & Richards, G. T. 2015, MNRAS, 451, 4328, doi: 10.1093/mnras/stv1230

Kaspi, S., Smith, P. S., Netzer, H., et al. 2000, ApJ, 533, 631, doi: 10.1086/308704

Kauffmann, G., White, S. D. M., Heckman, T. M., et al. 2004, MNRAS, 353, 713, doi: 10.1111/j.1365-2966.2004.08117.x

Kauffmann, G., Heckman, T. M., Tremonti, C., et al. 2003, MNRAS, 346, 1055, doi: 10.1111/j.1365-2966.2003.07154.x

Kawaguchi, T., Mineshige, S., Umemura, M., & Turner, E. L. 1998, ApJ, 504, 671, doi: 10.1086/306105

Keel, W. C., Kennicutt, R. C., J., Hummel, E., & van der Hulst, J. M. 1985, AJ, 90, 708, doi: 10.1086/113779

Kelly, B. C., Bechtold, J., & Siemiginowska, A. 2009, ApJ, 698, 895, doi: 10.1088/0004-637X/698/1/895

Kewley, L. J., Groves, B., Kauffmann, G., & Heckman, T. 2006, MNRAS, 372, 961, doi: 10.1111/j.1365-2966.2006.10859.x

Kochanek, C. S., Shappee, B. J., Stanek, K. Z., et al. 2017, PASP, 129, 104502, doi: 10.1088/1538-3873/aa80d9

Kormendy, J., & Richstone, D. 1995, ARA&A, 33, 581, doi: 10.1146/annurev.aa.33.090195.003053

Koss, M., Mushotzky, R., Treister, E., et al. 2012, ApJL, 746, L22, doi: 10.1088/2041-8205/746/2/L22

Koulouridis, E., Gkini, A., & Drigga, E. 2024, A&A, 684, A111, doi: 10.1051/0004-6361/202348212

Koulouridis, E., & Plionis, M. 2010, ApJL, 714, L181, doi: 10.1088/2041-8205/714/2/L181

Koulouridis, E., Ricci, M., Giles, P., et al. 2018, A&A, 620, A20, doi: 10.1051/0004-6361/201832974

Kozłowski, S. 2016, ApJ, 826, 118, doi: 10.3847/0004-637X/826/2/118

—. 2017, ApJ, 835, 250, doi: 10.3847/1538-4357/aa56c0

Kozłowski, S., Kochanek, C. S., Ashby, M. L. N., et al. 2016, ApJ, 817, 119, doi: 10.3847/0004-637X/817/2/119

Kozłowski, S., Kochanek, C. S., Udalski, A., et al. 2010, ApJ, 708, 927, doi: 10.1088/0004-637X/708/2/927

Kumar, S., Gezari, S., Heinis, S., et al. 2015, ApJ, 802, 27, doi: 10.1088/0004-637X/802/1/27

Laor, A. 2003, ApJ, 590, 86, doi: 10.1086/375008

Li, W. D., Filippenko, A. V., Treffers, R. R., et al. 2000, in American Institute of Physics Conference Series, Vol. 522, Cosmic Explosions: Tenth AstroPhysics Conference, ed. S. S. Holt & W. W. Zhang (AIP), 103–106, doi: 10.1063/1.1291702

Lightman, A. P., & Eardley, D. M. 1974, ApJL, 187, L1, doi: 10.1086/181377

Lomb, N. R. 1976, Ap&SS, 39, 447, doi: 10.1007/BF00648343

Lopes, P. A. A., Ribeiro, A. L. B., & Rembold, S. B. 2017, MNRAS, 472, 409, doi: 10.1093/mnras/stx2046

MacLeod, C. L., Ivezić, Ž., Kochanek, C. S., et al. 2010, ApJ, 721, 1014, doi: 10.1088/0004-637X/721/2/1014

MacLeod, C. L., Brooks, K., Ivezić, Ž., et al. 2011, ApJ, 728, 26, doi: 10.1088/0004-637X/728/1/26

MacLeod, C. L., Ivezić, Ž., Sesar, B., et al. 2012, ApJ, 753, 106, doi: 10.1088/0004-637X/753/2/106

Magorrian, J., Tremaine, S., Richstone, D., et al. 1998, AJ, 115, 2285, doi: 10.1086/300353

Man, Z.-y., Peng, Y.-j., Kong, X., et al. 2019, MNRAS, 488, 89, doi: 10.1093/mnras/stz1706

Marchesi, S., Lanzuisi, G., Civano, F., et al. 2016, ApJ, 830, 100, doi: 10.3847/0004-637X/830/2/100

Marconi, A., Risaliti, G., Gilli, R., et al. 2004, MNRAS, 351, 169, doi: 10.1111/j.1365-2966.2004.07765.x

Markowitz, A., Edelson, R., & Vaughan, S. 2003, ApJ, 598, 935, doi: 10.1086/379103

Markwardt, C. B. 2009, in Astronomical Society of the Pacific Conference Series, Vol. 411, Astronomical Data Analysis Software and Systems XVIII, ed. D. A. Bohlender, D. Durand, & P. Dowler, 251. https://arxiv.org/abs/0902.2850

Martini, P., Miller, E. D., Brodwin, M., et al. 2013, ApJ, 768, 1, doi: 10.1088/0004-637X/768/1/1

Masci, F. J., Laher, R. R., Rusholme, B., et al. 2019, PASP, 131, 018003, doi: 10.1088/1538-3873/aae8ac

Mateos, S., Alonso-Herrero, A., Carrera, F. J., et al. 2012, MNRAS, 426, 3271, doi: 10.1111/j.1365-2966.2012.21843.x

Matthews, T. A., & Sandage, A. R. 1963, ApJ, 138, 30, doi: 10.1086/147615

McConnell, N. J., Ma, C.-P., Gebhardt, K., et al. 2011, Nature, 480, 215, doi: 10.1038/nature10636

McHardy, I. M., Koerding, E., Knigge, C., Uttley, P., & Fender, R. P. 2006, Nature, 444, 730, doi: 10.1038/nature05389

McHardy, I. M., Papadakis, I. E., Uttley, P., Page, M. J., & Mason, K. O. 2004, MNRAS, 348, 783, doi: 10.1111/j.1365-2966.2004.07376.x

McHardy, I. M., Connolly, S. D., Horne, K., et al. 2018, MNRAS, 480, 2881, doi: 10.1093/mnras/sty1983

Merloni, A., Lamer, G., Liu, T., et al. 2024, A&A, 682, A34, doi: 10.1051/0004-6361/202347165

Messick, A., Baldassare, V., Geha, M., & Greene, J. 2023, ApJ, 953, 18, doi: 10.3847/1538-4357/acdc90

Mezcua, M., Civano, F., Marchesi, S., et al. 2018, MNRAS, 478, 2576, doi: 10.1093/mnras/sty1163

Mićić, M., Irwin, J. A., & Lin, D. 2022, ApJ, 928, 117, doi: 10.3847/1538-4357/ac56df

Middei, R., Vagnetti, F., Bianchi, S., et al. 2017, A&A, 599, A82, doi: 10.1051/0004-6361/201629940

Miller, C. J., Nichol, R. C., Gómez, P. L., Hopkins, A. M., & Bernardi, M. 2003, ApJ, 597, 142, doi: 10.1086/378383

Mishra, H. D., & Dai, X. 2020, AJ, 159, 69, doi: 10.3847/1538-3881/ab6225

Mishra, H. D., Dai, X., & Guerras, E. 2021, ApJL, 922, L17, doi: 10.3847/2041-8213/ac36d9

Morabito, L. K., & Dai, X. 2012, ApJ, 757, 172, doi: 10.1088/0004-637X/757/2/172

Morgan, C. W., Kochanek, C. S., Dai, X., Morgan, N. D., & Falco, E. E. 2008, ApJ, 689, 755, doi: 10.1086/592767

Mosby, G., Rauscher, B. J., Bennett, C., et al. 2020, Journal of Astronomical Telescopes, Instruments, and Systems, 6, 046001, doi: 10.1117/1.JATIS.6.4.046001

Mundell, C. G., Ferruit, P., Nagar, N., & Wilson, A. S. 2009, ApJ, 703, 802, doi: 10.1088/0004-637X/703/1/802

Mushotzky, R. 2004, in Astrophysics and Space Science Library, Vol. 308, Supermassive Black Holes in the Distant Universe, ed. A. J. Barger, 53, doi: 10.1007/978-1-4020-2471-9_2

Mushotzky, R. F., Done, C., & Pounds, K. A. 1993, ARA&A, 31, 717, doi: 10.1146/annurev.aa.31.090193.003441

Mushotzky, R. F., Edelson, R., Baumgartner, W., & Gandhi, P. 2011, ApJL, 743, L12, doi: 10.1088/2041-8205/743/1/L12

Nandra, K., George, I. M., Mushotzky, R. F., Turner, T. J., & Yaqoob, T. 1997, ApJ, 476, 70, doi: 10.1086/303600

NASA/IPAC Extragalactic Database (NED). 2019, NASA/IPAC Extragalactic Database (NED), IPAC, doi: 10.26132/NED1

Neugebauer, G., Soifer, B. T., Matthews, K., & Elias, J. H. 1989, AJ, 97, 957, doi: 10.1086/115040

Nicastro, F. 2000, ApJL, 530, L65, doi: 10.1086/312491

Panagiotou, C., & Walter, R. 2020, A&A, 640, A31, doi: 10.1051/0004-6361/201937390

Pancoast, A., Brewer, B. J., Treu, T., et al. 2014, MNRAS, 445, 3073, doi: 10.1093/mnras/stu1419

Pearson, S., Besla, G., Putman, M. E., et al. 2016, MNRAS, 459, 1827, doi: 10.1093/mnras/stw757

Pellegrini, S., Siemiginowska, A., Fabbiano, G., et al. 2007, ApJ, 667, 749, doi: 10.1086/520711

Peterson, B. M., Bentz, M. C., Desroches, L.-B., et al. 2005, ApJ, 632, 799, doi: 10.1086/444494

Petrecca, V., Papadakis, I. E., Paolillo, M., De Cicco, D., & Bauer, F. E. 2024, A&A, 686, A286, doi: 10.1051/0004-6361/202449161

Pimbblet, K. A., Shabala, S. S., Haines, C. P., Fraser-McKelvie, A., & Floyd, D. J. E. 2013, MNRAS, 429, 1827, doi: 10.1093/mnras/sts470

Ptak, A., Yaqoob, T., Mushotzky, R., Serlemitsos, P., & Griffiths, R. 1998, ApJL, 501, L37, doi: 10.1086/311444

Rees, M. J. 1984, ARA&A, 22, 471, doi: 10.1146/annurev.aa.22.090184.002351

Reynolds, C., Ueda, Y., Awaki, H., et al. 2014, arXiv e-prints, arXiv:1412.1177, doi: 10.48550/arXiv.1412.1177

Reynolds, C. S., & Miller, M. C. 2009, ApJ, 692, 869, doi: 10.1088/0004-637X/692/1/869

Richards, G. T., Fan, X., Newberg, H. J., et al. 2002, AJ, 123, 2945, doi: 10.1086/340187

Ricker, G. R., Winn, J. N., Vanderspek, R., et al. 2015, JATIS , 1, 014003, doi: 10.1117/1.JATIS.1.1.014003

Rothschild, R. E., Boldt, E. A., Holt, S. S., & Serlemitsos, P. J. 1974, ApJL, 189, L13, doi: 10.1086/181452

Ruan, J. J., Anderson, S. F., MacLeod, C. L., et al. 2012, ApJ, 760, 51, doi: 10.1088/0004-637X/760/1/51

Saez, C., Chartas, G., Brandt, W. N., et al. 2008, AJ, 135, 1505, doi: 10.1088/0004-6256/135/4/1505

Sánchez, P., Lira, P., Cartier, R., et al. 2017, ApJ, 849, 110, doi: 10.3847/1538-4357/aa9188

Sánchez-Sáez, P., Lira, P., Cartier, R., et al. 2019, ApJS, 242, 10, doi: 10.3847/1538-4365/ab174f

Scargle, J. D. 1982, ApJ, 263, 835, doi: 10.1086/160554

Schlafly, E. F., & Finkbeiner, D. P. 2011, ApJ, 737, 103, doi: 10.1088/0004-637X/737/2/103

Schmidt, K. B., Marshall, P. J., Rix, H.-W., et al. 2010, ApJ, 714, 1194, doi: 10.1088/0004-637X/714/2/1194

Schmidt, M. 1963, Nature, 197, 1040, doi: 10.1038/1971040a0

Schmidt, M., & Green, R. F. 1983, ApJ, 269, 352, doi: 10.1086/161048

Sesar, B., Ivezić, Ž., Lupton, R. H., et al. 2007, AJ, 134, 2236, doi: 10.1086/521819

Seyfert, C. K. 1943, ApJ, 97, 28, doi: 10.1086/144488

Shakura, N. I., & Sunyaev, R. A. 1976, MNRAS, 175, 613, doi: 10.1093/mnras/175.3.613

Shankar, F., Weinberg, D. H., & Miralda-Escudé, J. 2009, ApJ, 690, 20, doi: 10.1088/0004-637X/690/1/20

Shappee, B., Prieto, J., Stanek, K. Z., et al. 2014a, in American Astronomical Society Meeting Abstracts, Vol. 223, American Astronomical Society Meeting Abstracts #223, 236.03

Shappee, B. J., Prieto, J. L., Grupe, D., et al. 2014b, ApJ, 788, 48, doi: 10.1088/0004-637X/788/1/48

She, R., Ho, L. C., Feng, H., & Cui, C. 2018, ApJ, 859, 152, doi: 10.3847/1538-4357/aabfe7

Silverman, J. D., Kovač, K., Knobel, C., et al. 2009, ApJ, 695, 171, doi: 10.1088/0004-637X/695/1/171

Simm, T., Salvato, M., Saglia, R., et al. 2016, A&A, 585, A129, doi: 10.1051/0004-6361/201527353

Slavcheva-Mihova, L., & Mihov, B. 2011, A&A, 526, A43, doi: 10.1051/0004-6361/200913243

Smith, K. L., Mushotzky, R. F., Boyd, P. T., et al. 2018, ApJ, 857, 141, doi: 10.3847/1538-4357/aab88d

Son, S., Kim, M., & Ho, L. C. 2022, ApJ, 927, 107, doi: 10.3847/1538-4357/ac4dfc

Stern, D., Eisenhardt, P., Gorjian, V., et al. 2005, ApJ, 631, 163, doi: 10.1086/432523

Stern, D., Assef, R. J., Benford, D. J., et al. 2012, ApJ, 753, 30, doi: 10.1088/0004-637X/753/1/30

Strauss, M. A., Weinberg, D. H., Lupton, R. H., et al. 2002, AJ, 124, 1810, doi: 10.1086/342343

Tadhunter, C. 2016, A&A Rv, 24, 10, doi: 10.1007/s00159-016-0094-x

Tamura, N., Ohta, K., & Ueda, Y. 2006, MNRAS, 365, 134, doi: 10.1111/j.1365-2966.2005.09677.x

Terlevich, R., Tenorio-Tagle, G., Franco, J., & Melnick, J. 1992, MNRAS, 255, 713, doi: 10.1093/mnras/255.4.713

Timmer, J., & Koenig, M. 1995, A&A, 300, 707

Treiber, H. P., Hinkle, J. T., Fausnaugh, M. M., et al. 2022, arXiv e-prints, arXiv:2209.15019, doi: 10.48550/arXiv.2209.15019

—. 2023, MNRAS, 525, 5795, doi: 10.1093/mnras/stad2530

Trevese, D., Kron, R. G., Majewski, S. R., Bershady, M. A., & Koo, D. C. 1994, ApJ, 433, 494, doi: 10.1086/174661

Trèvese, D., & Vagnetti, F. 2002, ApJ, 564, 624, doi: 10.1086/324541

Troyer, J., Starkey, D., Cackett, E. M., et al. 2016, MNRAS, 456, 4040, doi: 10.1093/mnras/stv2862

Trumpler, R. J., & Weaver, H. F. 1953, Statistical Astronomy (Berkeley, University of California Press)

Tubín-Arenas, D., Krumpe, M., Lamer, G., et al. 2024, A&A, 682, A35, doi: 10.1051/0004-6361/202346773

Urry, C. M., & Padovani, P. 1995, PASP, 107, 803, doi: 10.1086/133630

Uttley, P., McHardy, I. M., & Papadakis, I. E. 2002, MNRAS, 332, 231, doi: 10.1046/j.1365-8711.2002.05298.x

Vallely, P. J., Kochanek, C. S., Stanek, K. Z., Fausnaugh, M., & Shappee, B. J. 2021, MNRAS, 500, 5639, doi: 10.1093/mnras/staa3675

Vanden Berk, D. E., Wilhite, B. C., Kron, R. G., et al. 2004, ApJ, 601, 692, doi: 10.1086/380563

Vanderspek, R., Doty, J. P., Fausnaugh, M., et al. 2018, TESS Instrument Handbook, Tech. rep., Kavli Institute for Astrophysics and Space Science, Massachusetts Institute of Technology

Vaughan, S., Edelson, R., Warwick, R. S., & Uttley, P. 2003, MNRAS, 345, 1271, doi: 10.1046/j.1365-2966.2003.07042.x

Wandel, A., Peterson, B. M., & Malkan, M. A. 1999, ApJ, 526, 579, doi: 10.1086/308017

Wasleske, E. J., & Baldassare, V. F. 2023, AJ, 166, 64, doi: 10.3847/1538-3881/ace16b

Wasleske, E. J., Baldassare, V. F., & Carroll, C. M. 2022, ApJ, 933, 37, doi: 10.3847/1538-4357/ac715b

Webb, N. A., Coriat, M., Traulsen, I., et al. 2020, A&A, 641, A136, doi: 10.1051/0004-6361/201937353

Wen, Z. L., & Han, J. L. 2024, ApJS, 272, 39, doi: 10.3847/1538-4365/ad409d

Willmer, C. N. A. 2018, ApJS, 236, 47, doi: 10.3847/1538-4365/aabfdf

Wright, E. L., Eisenhardt, P. R. M., Mainzer, A. K., et al. 2010, AJ, 140, 1868, doi: 10.1088/0004-6256/140/6/1868

Wrobel, J. M., Terashima, Y., & Ho, L. C. 2008, ApJ, 675, 1041, doi: 10.1086/527542

Yang, G., Brandt, W. N., Vito, F., et al. 2018, MNRAS, 475, 1887, doi: 10.1093/mnras/stx2805

York, D. G., Adelman, J., Anderson, Jr., J. E., et al. 2000, AJ, 120, 1579, doi: 10.1086/301513

Yu, Q., & Tremaine, S. 2002, MNRAS, 335, 965, doi: 10.1046/j.1365-8711.2002.05532.x

Yuan, F., Yoon, D., Li, Y.-P., et al. 2018, ApJ, 857, 121, doi: 10.3847/1538-4357/aab8f8

Yuk, H., & Dai, X. 2025, A&A, 698, A105, doi: 10.1051/0004-6361/202452469

Yuk, H., Dai, X., Jayasinghe, T., et al. 2022, ApJ, 930, 110, doi: 10.3847/1538-4357/ac6423

Yuk, H., Dai, X., & Mićić, M. 2025, arXiv e-prints, arXiv:2501.17844, doi: 10.48550/arXiv.2501.17844

Zang, W., Mao, S., Ge, J., Gould, A., & Yee, J. 2024, in American Astronomical Society Meeting Abstracts, Vol. 243, American Astronomical Society Meeting Abstracts, 231.01

Zu, Y., Kochanek, C. S., Kozłowski, S., & Udalski, A. 2013, ApJ, 765, 106, doi: 10.1088/0004-637X/765/2/106

Zubovas, K., & King, A. 2012, ApJL, 745, L34, doi: 10.1088/2041-8205/745/2/L34